การพัฒนาเพอรอฟสไกต์ $Sr_2FeMoO_{6-delta}$ สำหรับเซลล์เชื้อเพลิงออกไซด์ของแข็ง

นางสาวยุพดี อึ๊งอาภรณ์

วิทยานิพนธ์นี้เป็นส่วนหนึ่งของการศึกษาตามหลักสูตรปริญญาวิทยาศาสตรมหาบัณฑิต
สาขาวิชาเคมี ภาควิชาเคมี
คณะวิทยาศาสตร์ จุฬาลงกรณ์มหาวิทยาลัย
ปีการศึกษา 2558

DEVELOPMENT OF $Sr_2FeMoO_{6-delta}$ PEROVSKITE FOR SOLID OXIDE FUEL CELL

Miss Yupadee Ung-arphorn

A Thesis Submitted in Partial Fulfillment of the Requirements

for the Degree of Master of Science Program in Chemistry

Department of Chemistry

Faculty of Science

Chulalongkorn University

Academic Year 2015

Thesis Title	DEVELOPMENT OF $Sr_2FeMoO_{6-delta}$ PEROVSKITE FOR SOLID OXIDE FUEL CELL
By	Miss Yupadee Ung-arphorn
Field of Study	Chemistry
Thesis Advisor	Assistant Professor Soamwadee Chaianansutcharit, Ph.D.

Accepted by the Faculty of Science, Chulalongkorn University in Partial Fulfillment of the Requirements for the Master's Degree

.....Dean of the Faculty of Science
(Associate Professor Polkit Sangvanich, Ph.D.)

THESIS COMMITTEE

.....Chairman
(Associate Professor Vudhichai Parasuk, Ph.D.)

.....Thesis Advisor
(Assistant Professor Soamwadee Chaianansutcharit, Ph.D.)

.....Examiner
(Professor Thawatchai Tuntulani, Ph.D.)

.....External Examiner
(Tanawat Kanjanaboonmalert, Ph.D.)

ยุพดี อึ๊งอาภรณ์ : การพัฒนาเพอรอฟสไกต์ $Sr_2FeMoO_{6-delta}$ สำหรับเซลล์เชื้อเพลิงออกไซด์ของแข็ง (DEVELOPMENT OF $Sr_2FeMoO_{6-delta}$ PEROVSKITE FOR SOLID OXIDE FUEL CELL) อ.ที่ปรึกษาวิทยานิพนธ์หลัก: ผศ. ดร.โสมวดี ไชยอนันต์สุจริต, 82 หน้า.

ศึกษาสมบัติของดับเบิ้ลเพอรอฟสไกต์ Sr_2FeMoO_6 (SFMO), $Sr_2FeMo_{1-x}Co_xO_6$, $Sr_2FeMo_{1-x}Ni_xO_6$, $Sr_2Fe_{1-x}Co_xMoO_6$, $Sr_2Fe_{1-x}Ni_xMoO_6$, $Sr_{2-x}La_xFeMo_{0.5}Co_{0.5}O_6$, $Sr_{2-x}Pr_xFeMo_{0.5}Co_{0.5}O_6$, $Sr_{2-x}La_xFeMo_{0.5}Ni_{0.5}O_6$ และ $Sr_{2-x}Pr_xFeMo_{0.5}Ni_{0.5}O_6$ สำหรับใช้เป็นแอโนดในเซลล์เชื้อเพลิงออกไซด์ของแข็งที่อุณหภูมิปานกลาง (600-800 องศาเซลเซียส) วัสดุดังกล่าวสามารถสังเคราะห์ได้จากปฏิกิริยาที่ภาวะของแข็ง โดยการเผาและซินเตอร์ที่อุณหภูมิ 1000 และ 1300 องศาเซลเซียสเป็นเวลา 12 ชั่วโมงตามลำดับ ผลการศึกษาโครงสร้างพบว่าวัสดุที่เตรียมได้มีโครงสร้างหลักเป็นดับเบิ้ลเพอรอฟสไกต์และมีโครงสร้าง $SrMoO_4$ เป็นสารเจือปน เมื่อแทนที่ตำแหน่ง Mo ด้วย Co และ Ni พบว่า $SFMCo_x$ และ $SFMNi_x$ จะมีค่าการนำไฟฟ้าดีกว่า SFMO โดย $SFMCo_{0.5}$ and $SFMNi_{0.5}$ แสดงค่าการนำไฟฟ้าสูงที่สุดประมาณ 32.93 และ 50.11 ซีเมนต์ต่อเซนติเมตรที่อุณหภูมิ 800 และ 600 องศาเซลเซียสตามลำดับ นอกจากนี้การแทนที่ที่ตำแหน่ง Fe ด้วย Co และ Ni ในโครงสร้าง $SFCo_xM$ และ $SFNi_xM$ จะทำให้วัสดุมีการนำไฟฟ้าเพิ่มขึ้นที่สัดส่วน x = 0.1 และลดลงที่สัดส่วน x = 0.2 เมื่อศึกษาประสิทธิภาพของวัสดุในการใช้เป็นแอโนดในเซลล์เชื้อเพลิงออกไซด์ของแข็งเดี่ยว โดยใช้อิเล็กโตรไลต์ LSGM และแคโทด $Sr_{0.5}Sm_{0.5}CoO_3$ พบว่าแอโนด $SFMCo_{0.2}$, $SFMNi_{0.1}$, $SFCo_{0.1}M$ and $SFNi_{0.1}M$ ให้กำลังไฟฟ้าสูงที่สุด คือ 802, 723, 823 และ 834 มิลลิวัตต์ต่อตารางเซนติเมตรที่อุณหภูมิ 800 องศาเซลเซียสตามลำดับ ในทางตรงกันข้าม พบว่าไม่สามารถพัฒนาสมบัติการนำไฟฟ้าของ $SFMCo_{0.5}$ และ $SFMNi_{0.5}$ โดยการแทนที่ La และ Pr ที่ตำแหน่ง Sr ได้

ภาควิชา เคมี ลายมือชื่อนิสิต .....

สาขาวิชา เคมี ลายมือชื่อ อ.ที่ปรึกษาหลัก .....

ปีการศึกษา 2558

5572084423 : MAJOR CHEMISTRY

KEYWORDS: SOLID OXIDE FUEL CELL / ANODE MATERIAL / DOUBLE PEROVSKITE / ELECTRICAL CONDUCTIVITY

YUPADEE UNG-ARPHORN: DEVELOPMENT OF $Sr_2FeMoO_{6-delta}$ PEROVSKITE FOR SOLID OXIDE FUEL CELL. ADVISOR: ASST. PROF. SOAMWADEE CHAIANANSUTCHARIT, Ph.D., 82 pp.

Double perovskites, Sr_2FeMoO_6 (SFMO), $Sr_2FeMo_{1-x}Co_xO_6$, $Sr_2FeMo_{1-x}Ni_xO_6$, $Sr_2Fe_{1-x}Co_xMoO_6$, $Sr_2Fe_{1-x}Ni_xMoO_6$, $Sr_{2-x}La_xFeMo_{0.5}Co_{0.5}O_6$, $Sr_{2-x}Pr_xFeMo_{0.5}Co_{0.5}O_6$, $Sr_{2-x}La_xFeMo_{0.5}Ni_{0.5}O_6$ and $Sr_{2-x}Pr_xFeMo_{0.5}Ni_{0.5}O_6$, have been investigated as anode materials for intermediate-temperature solid oxide fuel cell (IT-SOFC, 600-800ºC). All materials synthesized in air by a conventional solid-state reaction with calcination and sintering temperatures of 1000ºC and 1300ºC for 12 hours, respectively, showed the double-perovskite structure as a major phase and $SrMoO_4$ as a minor phase impurity. The incorporation of Co and Ni into the Mo-site of SFMO structure resulted in the increasing of electrical conductivity of $SFMCo_x$ and $SFMNi_x$. Among the various oxides examined, $SFMCo_{0.5}$ and $SFMNi_{0.5}$ showed the highest electrical conductivity of 32.93 and 50.11 $S{\cdot}cm^{-1}$ at 800ºC and 600ºC, respectively. Moreover, a trace amount of Co and Ni inserted in the Fe-site led to the increase in the electrical conductivity of $SFCo_xM$ and $SFNi_xM$ as x = 0.1 and became decreasing when x = 0.2. The configuration of single fuel cells of Co-, Ni-doped SFMO/ $La_{0.9}Sr_{0.1}Ga_{0.8}Mg_{0.2}O_3$/ $Sr_{0.5}Sm_{0.5}CoO_3$ was fabricated and the highest power density of 802, 723, 823 and 834 $mW{\cdot}cm^{-2}$ at 800ºC was achieved from the cells using $SFMCo_{0.2}$, $SFMNi_{0.1}$, $SFCo_{0.1}M$ and $SFNi_{0.1}M$ as anodes, respectively. On the contrary, the conducting properties of $SFMCo_{0.5}$ and $SFMNi_{0.5}$ were not achieved by the introduction of La and Pr at Sr-site.

Department: Chemistry Student's Signature .....

Field of Study: Chemistry Advisor's Signature .....

Academic Year: 2015

ACKNOWLEDGEMENTS

I would like to express my deepest appreciation to my thesis advisor Assistant Professor Dr. Soamwadee Chaianansucharit for her kindness, valuable advice, encouragement and inspiration, not only in my research but also in my daily life. This gave me a lot of strength and motivated me going through some of the difficult days of my life. Without all the support that I have always received from her, this thesis would not have been completed.

In addition, I would like to thank Associate Professor Dr. Vudhichai Parasuk as the chairman, Professor Dr. Thawatchai Tuntulani, and Dr. Tanawat Kanjanaboonmalert for serving as this thesis committee.

Finally, I would like to add a special thanks to my family, all lab's members and friends for their love, entirely care and support.

CONTENTS

Page

Page

Page

LIST OF FIGURES

LIST OF TABLES

LIST OF ABBREVIATIONS

SOFCs	Solid oxide fuel cells
AFC	Alkaline fuel cell
PMEFC	Polymer electrolyte membrane fuel cell
PAFC	Phosphoric acid fuel cell
MCFC	Molten carbonate fuel cell
XRD	X-ray diffractrometry
SEM	Scanning electron microscopy
T	temperature
°C	degree Celsius
K	Kelvin
g	gram
mm	millimeter
cm	centimeter
μm	micrometer
Å	angstrom
σ	specific conductivity
E_a	activation energy
%	percent
t	tolerance factor
r	ionic radius
L	length
I	current
T	thickness
V	voltage
W	width
P	power density
R	resistance
Z	impedance

CHAPTER I
INTRODUCTION

Natural resource consumption has been growing rapidly for the last century due to global industrialization. The limitation of natural resources such as oil, gas and fossil fuel to produce electricity becomes international concerns including environment problems. Thus, the breakthrough of environmental-friendly technology such as solar cell, fuel cells, biofuel and wind energy is of interest as an alternative energy source for future generation.

1.1 Fuel Cell [1-5]

Fuel cells are of great-interest electrochemical device that produces electricity and heat with minimal environmental impact. They are categorized by the kind of electrolyte into five major types: phosphoric acid fuel cell (PAFC), polymer electrolyte membrane fuel cell (PEMFC), alkaline fuel cell (AFC), molten carbonate fuel cell (MCFC) and solid-oxide fuel cell (SOFC), as shown in Table 1.1. The first three types are operated at low temperature (60-220°C) leading to relatively low electrical efficiency of 40-50%. In contrast, the high operating temperature (600-1000°C) of the next two types promotes high power efficiency up to 50-60%. Among these fuel cells, PEMFCs and SOFCs have received much attention because of their high efficiency, intriguing applications, and fuel flexibility. PEMFCs are attractive for motor vehicles whereas SOFCs are attractive for stationary applications.

1.2 Solid Oxide Fuel Cells (SOFCs) [6-8]

Regarding to all solid-state construction and high temperature operation, SOFC has a number of unique characteristics and advantages over other fuel cells such as high electronic-conversion efficiency, environmentally-friendly performance, cogeneration—composed of power and heat, fuel adaptability, and size flexibility. SOFCs have, then, become important as a clean-energy generator that provides a broad range of power from watts to megawatts.

Table 1.1 Description of major fuel cell types [9]

	PEMFC	PAFC	AFC	MCFC	SOFC
Electrolyte	Polymer membrane	Liquid H_3PO_4 (immobilized)	Liquid KOH (immobilized)	Molten carbonate	Ceramic
Charge carrier	H^+	H^+	OH^-	CO_3^{2-}	O^{2-}
Operating temperature	80°C	200°C	60-220°C	650°C	600-1000°C
Catalyst	Platinum	Platinum	Platinum	Nickel	Perovskite (ceramic)
Cell components	Carbon based	Carbon based	Carbon based	Stainless based	Ceramic based
Fuel compatibility	H_2, methanol	H_2	H_2	H_2, CH_4	H_2, CH_4, CO
Efficiency	40-50%	40-50%	30%	50-60%	50-60%

1.2.1 Operation of SOFCs [10]

A SOFC single cell consists of two electrodes (anode and cathode) sandwiched around a hard ceramic electrolyte—an oxide ion conducting ceramic material. The operating principle of a SOFC involves the reduction of molecular O_2 at the cathode and the diffusion of the produced O^{2-} through an electrolyte into the anode, where it reacts with hydrogen fuel to produce water. At the same time, the electrons flow from the anode to the cathode through an external circuit to achieve the desired power. The schematic diagram for the conversion of chemical energy into electrical energy is illustrated in Figure 1.1.

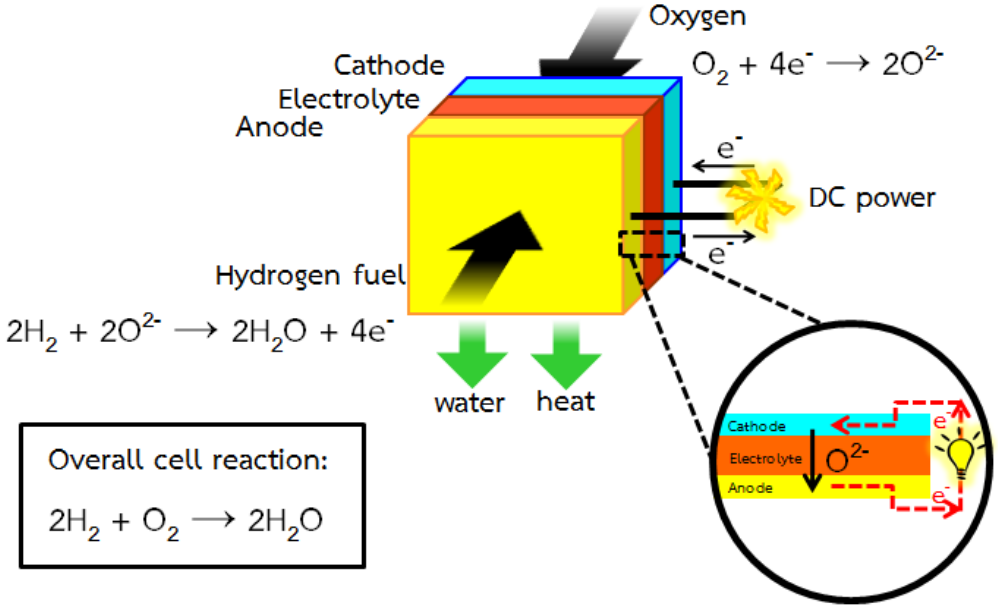

Figure 1.1 Schematic diagram of SOFC operation

1.2.2 Materials for SOFC components

As mentioned earlier, one of the unique advantages of SOFC over other types of fuel cell is its tolerance to the impurities of inlet fuels; that is why the various types of fuel can be applied with SOFC. However, at high operating temperature there are some limitations to SOFC especially the durability of material used. Thus, the materials for each component have been carefully selected based on the operating temperature and basic principle of SOFCs.

1.2.2.1 Electrolyte [11-16]

Electrolyte, one of the core components of the SOFC, is usually made of a dense solid metal-oxide. Based on the concept of oxygen-ion conducting, electrolyte is used to prevent the two electrodes from the electron contacting. It allows only the migration of oxygen ion from the cathode to the anode to maintain the overall charge balance. For satisfactory performance, the electrolyte should accomplish the requirement that limits the choice of the material including high oxygen-ion conductivity, insignificant electronic conductivity, high density to boost gas impermeability, stability over a wide range of temperature and oxygen partial pressure, good chemical interaction with electrode materials to avoid the formation of blocking interface phase, and compatibility to the adjacent electrode informed by thermal expansion coefficient (TEC).

Three kinds of electrolyte have been widely used for SOFCs, yttria-stabilized zirconia (YSZ), gadolinium- or samarium-doped ceria (GDC or SDC), and strontium, magnesium-doped lanthanum gallate (LSGM). There are advantages and disadvantages of these electrolyte materials. YSZ, the conventional electrolyte, is widely employed at high temperature because of its sufficient ionic conductivity; moreover, it is easy to produce and its components are abundant and inexpensive. The other ceria-based electrolytes (GDC or SDC) have received much attention as an alternative electrolyte because of their high conductivity to oxygen ion at lower temperature compared to YSZ, as shown in Figure 1.2. However, in a reducing condition, Ce^{4+} is reduced to Ce^{3+} causing an increase in electronic conductivity and the decrease of cell efficiency. For LSGM, the perovskite-based electrolyte, the ionic conductivity is higher than YSZ and SDC at intermediate temperature and it is more compatible with the lanthanum transition-metal oxide cathode. Nevertheless, its components as starting materials including La_2O_3, $SrCO_3$ and Ga_2O_3 are expensive.

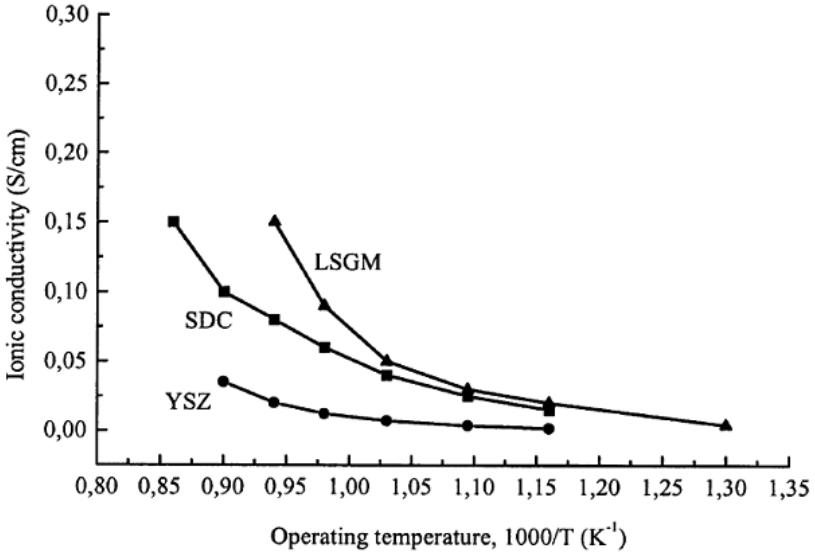

Figure 1.2 Ionic conductivity of some electrolyte materials (YSZ, SDC and LSGM) [3]

In addition to the high oxide-ion transport in electrolyte materials, thermal expansion coefficient (TEC) is also another factor. To avoid the cell cracking during the operation, the TEC values of electrolyte and electrodes should be relatively closed. The TEC values of some electrolytes are summarized in Table 1.2.

Table 1.2 Thermal expansion coefficients of some electrolytes

electrolyte	thermal expansion coefficient (K^{-1})	[ref]
YSZ	10.8×10^{-6}	[13]
SDC	13.5×10^{-6}	[17]
LSGM	11.7×10^{-6}	[18]

1.2.2.2 Cathode [19]

The cathode is the SOFC electrode where the electrochemical reduction of oxygen occurs. At the cathode the reaction mechanism occurs in many steps as explained below:

I) Adsorption of molecular oxygen along the cathode surface

II) Dissociation and reduction of adsorbed oxygen along the cathode surface to produce oxygen ion

III) Diffusion of oxygen ion in the bulk cathode

IV) Transfer of oxygen ion from the bulk cathode into the electrolyte

Based on the oxygen reduction reaction, the kinetics of electrode is an important aspect resulting in the large interfacial polarization resistance. To minimize the resistance, the materials requirement for cathode must be fulfilled as follows:

- high electronic and ionic conductivity
- chemically compatible with the other contacting components under operating atmosphere
- thermal compatibility in TEC with other components
- acceptable porosity to permit oxygen diffusion
- chemical and microstructural stability under an oxidizing atmosphere during fabrication and operation

To meet these expectations, three types of oxide structure: simple perovskite oxide, double-ordered perovskite, and Ruddlesden-Popper phases, have been studied as cathode materials because of their high ionic and electronic conductivity and also thermal stability. Among the number of cathode materials, lanthanum strontium manganites ($La_{1-x}Sr_xMnO_3$, LSM) [20-23], the state-of-the-art material, are extensively used due to their excellent conducting properties and good thermal compatibility with the YSZ electrolyte to operate at high temperature (800-1000°C).

In addition to the cathode requirement previously mentioned, the oxygen reduction reaction taking place at the active area called triple phase boundary (TPB) is also important. TPBs are the sites where the oxygen ion conductor, electronic conductor, and gas phase are in contact. Because of this, to provide materials with more regions of electrochemically active sites, mixed ionic and electronic conductors (MIECs) are required. If the cathode is a MIEC material, the kinetic of oxygen reduction is enhanced because the material has more active sites for the reduction at the surface and also a pathway for oxygen ions to diffuse through the bulk as displayed in Figure 1.3.

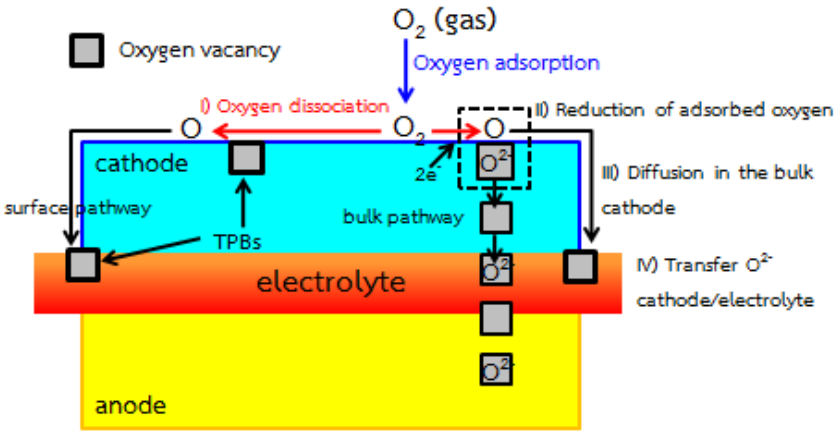

Figure 1.3 Active area of oxygen reduction reaction

1.2.2.3 Anode [24, 25]

Because the oxidation reaction of hydrogen takes place at the anode side, anode materials should be stable in the reducing atmosphere of the fuels such as hydrogen and hydrocarbon, predominantly active for electrochemical or catalytic the oxidation of the selected fuel gas, high electrical conductivity, good chemical and thermal compatibility with those of the adjoining components, good tolerance to carbon built-up and sulfur containing in case of using hydrocarbon fuel, and sufficiently porous to allow the fuel supply and the reaction product removal. Moreover, like the cathode materials, the anode should favorably be made of MIEC materials.

In terms of researches on the anode materials, Ni-based material is the most common anode material in the SOFC which utilizes hydrogen as a fuel [26]. Nickel is an excellent catalyst for both hydrogen oxidation and steam reforming. Unfortunately, it poses some problems such as sulfur poisoning caused by adsorption of H_2S and the formation of coke when using hydrocarbon as a fuel [27]. Consequently, to limit carbon formation on anode materials, several approaches have been taken. One approach is to replace or make alloys of Ni component with other metals such as Co, Cu and Fe [28, 29]. The anode containing mixtures of metallic alloy is more tolerant to carbon deposition but the power density of the cell is lower than that with the Ni-based anode material. Accordingly, many researchers have concentrated on the development of the anodes including the oxide compound having adequate conductivity at the reducing atmosphere. Sr_2FeMoO_6 (SFMO), a double perovskite oxide, is one of the most promising anodes because it produces high power densities when using methane as a fuel [18, 30]; in

addition, it provides mixed valence redox couples Mo^{5+}/ Mo^{6+} and Fe^{3+}/ Fe^{2+} that can accept electrons from hydrogen or hydrocarbon fuel, to induce dissociation on the oxide surface.

1.3 Perovskite oxide [31]

The compound of ABX_3, where A is the alkaline or alkaline earth metal, B is the transition metal and X is the anion that bond to both metal ions, is widely investigated. The adopted structure of oxides is known as perovskite, ABO_3. In the idealized structure, cubic perovskite oxide has the A cation occupying in the middle of the cube resulting in the twelve-fold coordination site with O atoms whereas the B cation forms a three-dimensional network of corner sharing BO_6 octahedra as shown in Figure 1.4.

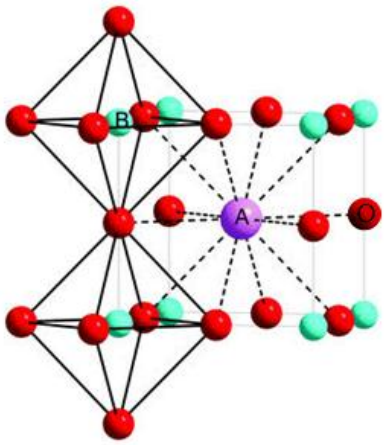

Figure 1.4 Perovskite structure, ABO_3 [31]

A subclass of perovskite oxides is represented by the general formula $A_2B'B''O_6$, known as “double perovskite”. It is named because the unit cell is twice as that of perovskite. It has the same framework of twelve-coordinated A sites and six-coordinated B sites, but the two cations are well-ordered on the B site. Sr_2FeMoO_6, for example, has the Fe and Mo atoms alternatively arranged as shown in Figure 1.5.

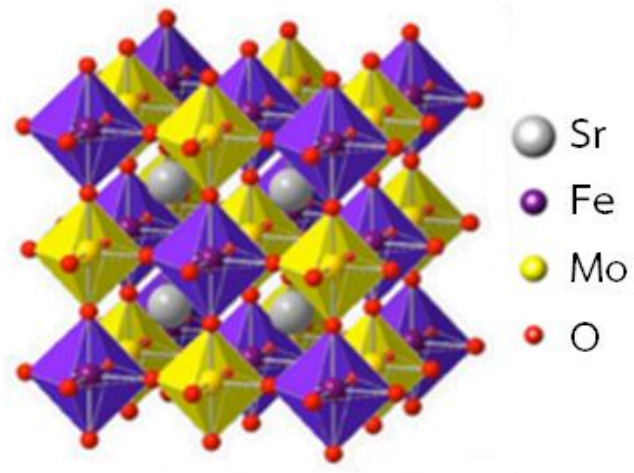

Figure 1.5 Double perovskite as Sr_2FeMoO_6 structure [32]

Double perovskites have received much attention recently due to the catalytic properties related to electronic conductivity and oxygen vacancy. Because of this, these oxides seem to be perfect candidates to exhibit interesting catalytic properties in anode SOFCs.

Apart from the idealized cubic structure, a large number of perovskite or related structure can be found by partial substitution of A and B cations with other cations (same or different in size and charge). Many perovskites are distorted from the ideal cubic structure in which Goldschmidt proposed an index named tolerance factor (*t*) for evaluating the stability of perovskites based on ionic radii and the *t* value is defined by the equation 1.1 [31].

$$t = \frac{(r_A + r_O)}{\sqrt{2} \times (r_B + r_O)} \qquad (1.1)$$

where r_A, r_B and r_O are relative ionic radii of the A and B cations and the oxygen ion, respectively.

The ideal cubic perovskite structure is found in a few case for *t*-values very close to 1.00 at high temperature. However, the cubic perovskite structure can be maintained with $0.95 \leq t \leq 1.04$ and the low symmetry (orthorhombic and tetragonal) structure can be found for $0.75 \leq t \leq 0.90$.

1.4 Electrical conductivity

In perovskite structure, the B cations surrounded with oxide anions are related to the mobile charge carrier—excess electron and electron hole—along the B-O-B chains. Because of the overlapping of the orbitals of oxide ion and the adjoining B-site cation, as illustrated in Figure 1.6, the electrons and holes reversibly exchange creating the electronic conductivity. The higher the concentration of the mobile charge carriers, the greater the conductivity is observed. Moreover, the introduction of the different oxidation state cation, aliovalent doping, can also generate mobile charge carriers. For example, increasing in valence of the B cation produces electronic compensation or the formation of oxygen vacancies known as ionic compensation. Since the two types of compensation are related to other factors including the type and concentration of dopant, the microstructure, the temperature, the oxygen partial pressure, etc., the appearance of both is undesirable.

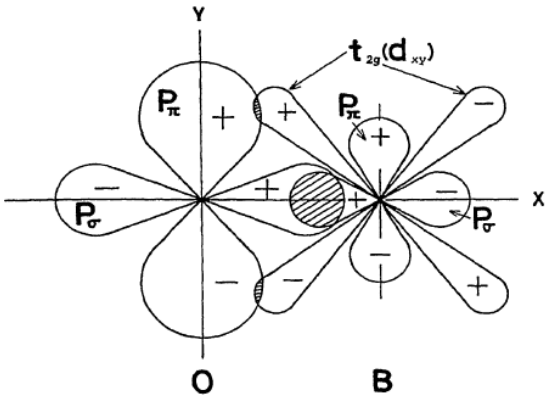

Figure 1.6 Covalent bonds between anionic *p* orbital and t_{2g} orbital of B cations [33]

For ionic conductivity, the pathway of oxygen migration is constituted by two A-site cations and one B-site cation called “Saddle point” as displayed in Figure 1.7. The oxygen ion passes from one site to the adjacent site along the octahedral edge. The maximum ionic radius of mobile ions past through the saddle point is represented by critical radius (r_{cr}). This factor can be calculated from equation 1.2: where r_A and r_B are the ionic radius of the A ion and B ion, respectively, and a_0 relates to the cubic lattice parameter.

$$r_{cr} = \frac{a_0(\frac{3}{4}a_0 - \sqrt{2}r_B) + r_B^2 - r_A^2}{2(r_A - r_B) + \sqrt{2}a_0} \qquad (1.2)$$

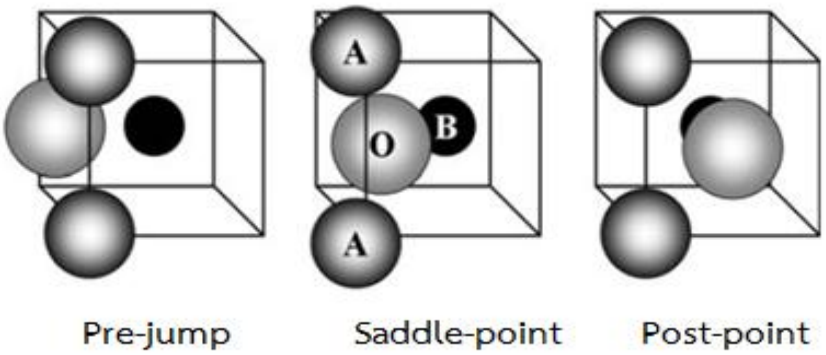

Figure 1.7 The migration of the oxygen ion passes through the saddle point [33]

Another factor determining the SOFC electrode performance is the electrical conductivity (**σ**), calculating from the equation 1.3:

$$\sigma = nq\mu \qquad (1.3)$$

Where n is the concentration of the carried charge (cm^{-3}), q is the charge (coulombs) and μ is the value of the mobility of the charge carrier ($cm^2 s^{-1} V^{-1}$) and the unit of **σ** is $S{\cdot}cm^{-1}$.

In summary, the electrical conductivity is comprised of two mechanisms, electronic and ionic conduction; differentiated from the carrier like electron/hole or oxygen vacancies. The electronic conduction is much higher than the ionic conduction; hence, the summation of both conduction values is determined in terms of the electrical conductivity.

1.5 Oxygen transport process [34]

Because perovskite oxides have good mixed ionic and electronic property, they can be used as membranes for oxygen separation. Based on the difference in the partial pressure of oxygen between the feed side and the permeate side, oxygen migrates from the feed side through a dense conducting material to the permeate side. The mechanism of oxygen transport processes occurs in many steps as displayed in Figure 1.8.

I) gas phase mass transfer (diffusion from the high oxygen partial pressure side)

II) surface exchange (adsorption, ionization and incorporation)

III) bulk diffusion

IV) surface exchange (association and desorption)

V) gas phase mass transfer (diffusion to the low oxygen partial pressure side)

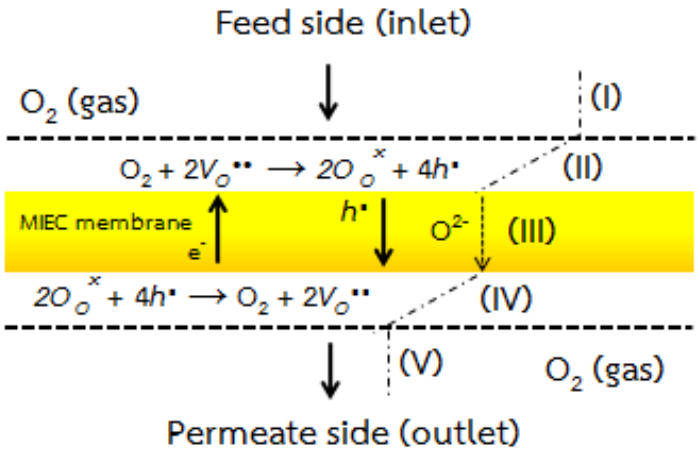

Figure 1.8 Mechanism of oxygen permeation through MIEC membrane [34]

Where O_O^x = oxide ion on the oxide ion lattice site with neutral charge

$V_O^{\bullet\bullet}$ = oxygen vacancies with double positive charge

$h^\bullet$ = electronic holes

To enhance the oxygen transport mechanism, increasing surface area is concerned by polishing the membrane surface and coating the porous layer on the top of the dense membrane. This option can promote oxygen permeation flux by promoting the adsorption and dissociation of oxygen. In addition to the surface active area, a decrease of membrane thickness can also increase the oxygen permeation flux.

1.6 Fuel cell characterization

In this section, the most popular and effective SOFC characterization techniques e.g. current-voltage measurement and electrochemical impedance spectroscopy, are briefly introduced.

1.6.1 Current-voltage (*i*-V) characterization [35]

Generally, an *i*-V measurement provides overall quantitative evaluation of SOFC performance and SOFC power density. The performance of the SOFC device can be summarized in Figure 1.9. This graph, called a current-voltage (*i*-V) curve, shows the voltage output of the fuel cell accompanied with the applied current normalized by the area of the electrode to give a current density (*i*). In y-axis, open circuit voltage, OCV, is normally less than the ideal voltage due to polarization losses. The higher the loaded current is applied, the lower the output voltage of the cell is collected, that means the greater of energy losses. These losses arise from three polarization mechanisms, which contributes to the characteristic shape of *i*-V curve, as follows:

1. Activation losses (losses due to electrochemical reaction)
2. Ohmic losses (losses due to ionic and electronic conduction)
3. Concentration losses (losses due to mass transport)

$$P = iV \tag{1.4}$$

Apart from *i*-V curve, a power density curve as a function of current density can be constructed from the information of *i*-V curve by multiplying the voltage at each point on the *i*-V curve as shown in equation 1.4. The combination of fuel cell *i*-V and power density curves is displayed in Figure 1.10. In this figure, fuel cell voltage is given on the left-hand of y-axis while power density is given on the right-hand of y-axis.

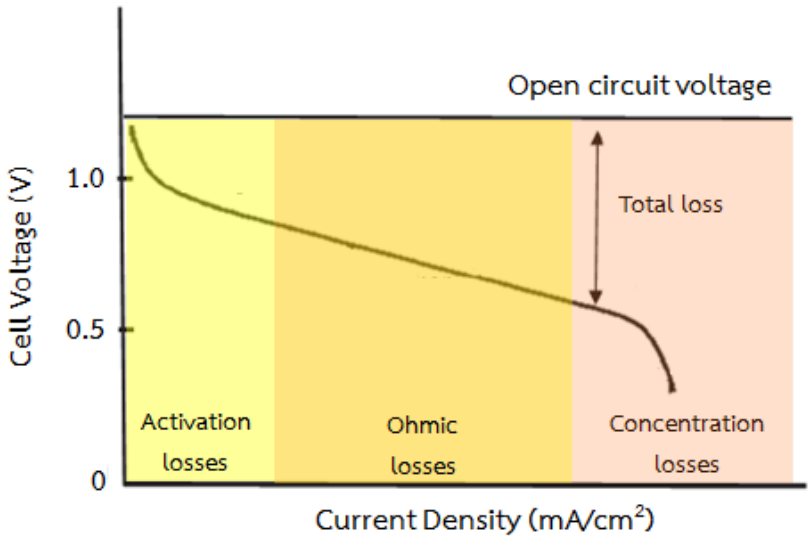

Figure 1.9 Schematic diagram of fuel cell *i*-V curve

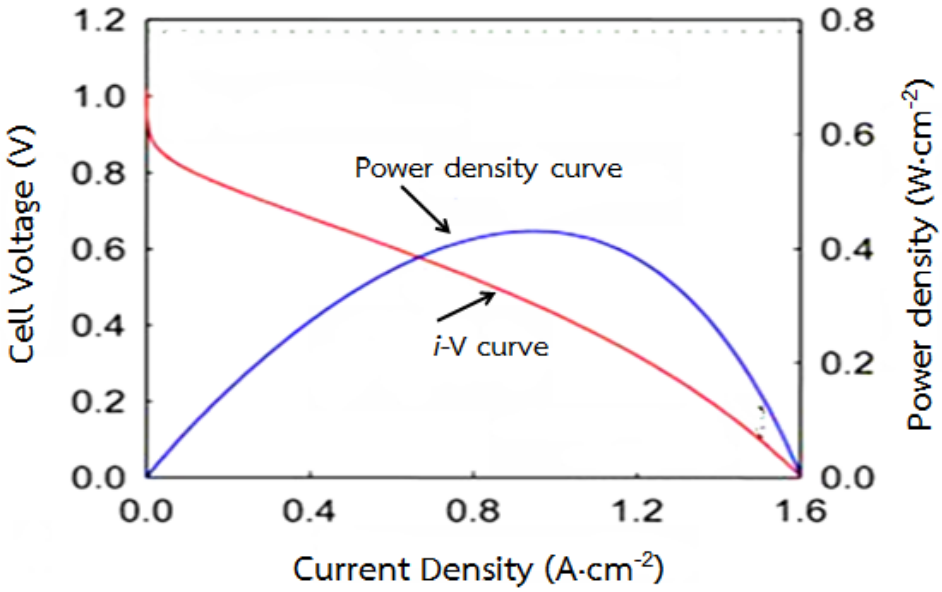

Figure 1.10 The combination of fuel cell *i*-V and power density curve

1.6.2 Electrochemical Impedance Spectroscopy (EIS) characterization or AC impedance

While the *i*-V curve performs quantification of fuel cell performance, electrochemical impedance spectroscopy, a powerful technique to exactly define polarization losses (easier known as resistance), can provide the information on individual losses; however, the interpretation of the result is relatively time-consuming.

AC impedance measurements are often made by applying a small voltage over a wide range of frequency and the current output is responded. Unlike resistance, impedance can deal with time- or frequency-dependent system. The impedance (Z) can hence be expressed by the ratio of the applied sinusoidal voltage and the phase-shifted current response as related to Ohm's Law defined below:

$$Z = \frac{V_{(t)}}{i_{(t)}} = \frac{V\cos(\omega t)}{i\cos(\omega t - \varphi)} = Z_0(\cos\varphi + j\sin\varphi)$$

Where j in this expression represents the imaginary number ($j = \sqrt{-1}$). Therefore, impedance data are plotted in terms of the real and imaginary components, as expressed by $Z_{real} = Z_0\cos\varphi$ and $Z_{imag} = Z_0\sin\varphi j$, respectively, ($Z_{real}$ on the x axis and $-Z_{imag}$ on the y axis). The representation of impedance data are known as Nyquist plot as shown in Figure 1.11 which can describe the physiochemical processes occurring in the fuel cell associated with a network of resistors (R), capacitors (C) and inductors (L).

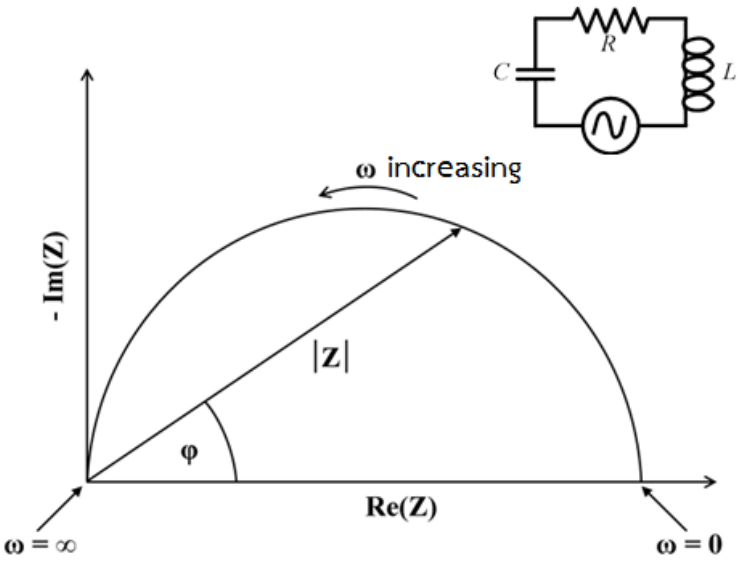

Figure 1.11 Nyquist plot of impedance

1.7 Literature reviews

Because the conventional Ni-based anode materials encounter several problems such as instability upon redox cycling, nickel coarsening at high temperature, sulfur contamination and carbon deposition, finding an appropriate anode is a crucial task for SOFC researches.

The double perovskite oxide, Sr_2FeMoO_6, containing alternate layers of FeO_6 and MoO_6 octahedra with the voluminous Sr cations that occupy the voids between the octahedral, has been extensively studied as a promising anode material for SOFCs because this MIEC material combines good catalytic activity with ionic and electrical conductivity. Some of those researches are summarized as follows.

Huang [36] et al. reported that the B-site of ordered-perovskite Sr_2MgMoO_6 can tolerate to the carbon built-up and sulfur poisoning presenting in natural gas.

Zhang [37] et al. studied on A_2FeMoO_6 (A = Ca, Sr, Ba) double-perovskite and found the coexistence of Fe^{3+}- Mo^{5+} and Fe^{2+}- Mo^{6+} in these compounds. In the nitrogen environment, the phase stability of Sr_2FeMoO_6 and Ba_2FeMoO_6 were stable up to 1200°C whereas Ca_2FeMoO_6 differed from the others. However, the oxygen vacancy concentration of Sr_2FeMoO_6 was higher than that of Ba_2FeMoO_6, which resulted in the maximum power density of Sr_2FeMoO_6. Moreover, Sr_2FeMoO_6 displayed exceptional thermal compatibility with LSGM (9182) electrolyte.

Suthirakun [38] et al. investigated the electrochemical oxidation of H_2 fuel on the surface of $Sr_2Fe_{1.5}Mo_{0.5}O_6$ (SFMO) by using ab initio thermodynamic analysis. They

found that Mo plays a crucial role in catalytic activity of SFMO under fuel cell operating condition. To improve the overall electrochemical performance of SOFC, increasing the Mo content or a small amount of an active transition metal like Ni to the structure must be achieved.

Feng [39] et al. studied the substitution of Fe in $Sr_2Fe_{1.5}Mo_{0.5}O_6$ with Ni. They found that $Sr_2Fe_{1.4}Ni_{0.1}Mo_{0.5}O_6$ showed the highest electrical conductivity of 20.6 $S{\cdot}cm^{-1}$ and the maximum power density of 530 $mW{\cdot}cm^{-2}$ was achieved at 800°C in H_2. This result can be explained by the presence of the ion pairs of Fe^{3+}/Mo^{5+}, which is beneficial to the electron transfer between themselves and to improve the redox reaction rate.

Pan [40] et al. replaced Fe with Co in the $Sr_2Fe_{1.5}Mo_{0.5}O_6$ structure to improve the SOFC performance. When Co was introduced, the conductivity and the chemical diffusion coefficient increased because Co-doping increased the oxygen vacancy concentration. In addition, the interfacial polarization resistance of Co-substituted electrode on LSGM electrolyte was inversely proportional to the Co content.

Kharton [41] et al. examined the doping of Fe and Ni on $LaCo_{1-x-y}Fe_xNi_yO_3$ perovskite family. Ni substitution was the cause of the decreased TEC value and the increased electrical conductivity and oxygen nonstoichiometry. Moreover, a marked rise in the oxygen permeation flux is resulted from the substitution of Co with Ni.

Savaniu [42] et al. evaluated the potential of La in $SrTiO_3$ ($La_{0.2}Sr_{0.7}TiO_3$) as an anode material. At the operating temperature of 650°C, the acceptable conductivity and the enhancement in fuel oxidation were observed. The fuel cell test of 0.54 $W{\cdot}cm^{-2}$ was achieved at 750°C using humidified H_2 as fuel.

Wang [43] et al. investigated the electrochemical properties of $Sr_{1-x}Pr_xCo_{0.95}Sn_{0.05}O_3$ as a SOFC cathode material. When the x value was increased up to 0.2, their conductive property changed from semiconductor to metal behavior. Moreover, the electrical conductivity increased with the Pr content and reached the maximum value of 1350 $S{\cdot}cm^{-2}$ at 700°C using the $Sr_{1-x}Pr_{0.3}Co_{0.95}Sn_{0.05}O_3$ cathode. However, the delamination of the cathode was noticed from $Sr_{1-x}Pr_{0.2}Co_{0.95}Sn_{0.05}O_3$ because of the TEC mismatch with SDC electrolyte while the $Sr_{1-x}Pr_{0.2}Co_{0.95}Sn_{0.05}O_3$-SDC composite maintained a good electrolyte matching with SDC.

Jin [44] et al. investigated double perovskites $LnBaCoFeO_5$ (LnBCF, Ln= Pr and Nb). At the temperature below 1000°C, they found that these materials were chemically compatible with LSGM9182 electrolyte. The two oxidation states, +3 and +4, were contributed to Fe and Co ions in $LnBaCoFeO_5$ and Pr^{3+} was mostly found in PBCF. Moreover, the TEC values of PBCF and NBCF, 21.0 x 10^{-6} and 19.5 x 10^{-6} K^{-1},

respectively, at 30-1000°C, were lower than the TECs of $LnBaCoFeO_5$ based-structure. The highest electrical conductivities of 321 and 172 $S{\cdot}cm^{-1}$ were obtained from PBCF and NBCF, respectively, at 350°C.

Vitoriano [45] et al. synthesized $La_{0.6}Ca_{0.4}Fe_{1-x}Ni_xO_3$ (x = 0.1, 0.2 and 0.3, LCFN). The highest electrochemical performance was achieved from $La_{0.6}Ca_{0.4}Fe_{1-x}Ni_{0.1}O_3$ using SDC as electrolyte and the highest electrical conductivity over 350 $S{\cdot}cm^{-1}$ at 500°C was also observed.

From these literatures, the replacement of Co, Ni, Pr and La ions could enhance the conducting properties of perovskite oxide. As a result, the aim of this work is to improve properties of Sr_2FeMoO_6 including electrical conductivity and oxygen permeation by introduction of Co, Ni, Pr and La ions as potential anode material in SOFCs.

1.8 Objective

1.8.1 To synthesize Sr_2FeMoO_6 perovskite oxide materials as below:

- Substitution Mo and Fe site of Sr_2FeMoO_6 structure with Co and Ni
  - $Sr_2FeMo_{1-y}M'_yO_6$ (M' = Co, Ni; y = 0.0-0.5)
  - $Sr_2Fe_{1-y}M'_yMoO_6$ (M' = Co, Ni; y = 0.0-0.5)
- Substitution Sr site of the selected-oxide above, which performs good electrical conductivity, with La and Pr
  - $Sr_{2-x}M_xFeMo_{1-y}Co_yO_6$ (M = La, Pr; x = 0.0-0.3)
  - $Sr_{2-x}M_xFeMo_{1-y}Ni_yO_6$ (M = La, Pr; x = 0.0-0.3)

1.8.2 To characterize the synthesized oxides for phase identification and morphology.

1.8.3 To measure electrical conductivity and oxygen permeation of oxide disks.

1.8.4 To evaluate the electrochemical performance of the prepared oxides.

CHAPTER II
EXPERIMENTAL

The chemical, apparatus and experimental procedures including processing of preparation and characterization of materials, are described as below:

2.1 Chemicals

The chemicals and reagents listed in Table 2.1 were used without further purification.

Table 2.1 Chemicals and reagents used in this research

Chemicals and reagent	Formula weight	Purity (%)	Company
$SrCO_3$	147.63	≥99.9	Aldrich
Fe_2O_3	159.69	81	Labchem
MoO_3	143.94	99.5	Univar
Co_3O_4	240.80	99.5	Aldrich
NiO	74.69	99	Aldrich
Pr_6O_{11}	1021.44	99.9	Aldrich
La_2O_3	325.81	99.99	Wako
Ga_2O_3	187.44	≥99.99	Aldrich
MgO	40.3	≥98.0	Fluka
$Sr(NO_3)_2$	211.63	99	Sigma-Aldrich
$Sm(NO_3)_3{\cdot}6H_2O$	444.47	99.9	Aldrich
$Co(NO_3)_3{\cdot}6H_2O$	291.03	98-102.0	Univar
$C_6H_8O_7{\cdot}H_2O$	210.14	99.5-100.5	Merck
NH_4NO_3	80.04	101.0	J.T. Baker
$C_{10}H_{16}N_2O_8$	292.25	99.4-100.6	Univar
NH_3 solution	35.5	25	Merck

2.2 Material preparation

2.2.1 Anode preparation

All anodes were synthesized by a conventional solid-state reaction. The abbreviation and the anode-composition are summarized in Table 2.2

Table 2.2 The component of all samples

Substituted site	Dopant	Composition	Abbreviation
-	-	Sr_2FeMoO_6	SFMO
Mo	Co	$Sr_2FeMo_{0.9}Co_{0.1}O_6$	$SFMCo_{0.1}$
		$Sr_2FeMo_{0.8}Co_{0.2}O_6$	$SFMCo_{0.2}$
		$Sr_2FeMo_{0.7}Co_{0.3}O_6$	$SFMCo_{0.3}$
		$Sr_2FeMo_{0.5}Co_{0.5}O_6$	$SFMCo_{0.5}$
	Ni	$Sr_2FeMo_{0.9}Ni_{0.1}O_6$	$SFMNi_{0.1}$
		$Sr_2FeMo_{0.7}Ni_{0.3}O_6$	$SFMNi_{0.3}$
		$Sr_2FeMo_{0.5}Ni_{0.5}O_6$	$SFMNi_{0.5}$
Fe	Co	$Sr_2Fe_{0.9}Co_{0.1}MoO_6$	$SFCo_{0.1}M$
		$Sr_2Fe_{0.8}Co_{0.2}MoO_6$	$SFCo_{0.2}M$
		$Sr_2Fe_{0.7}Co_{0.3}MoO_6$	$SFCo_{0.3}M$
	Ni	$Sr_2Fe_{0.9}Ni_{0.1}MoO_6$	$SFNi_{0.1}M$
		$Sr_2Fe_{0.8}Ni_{0.2}MoO_6$	$SFNi_{0.2}M$
		$Sr_2Fe_{0.7}Ni_{0.3}MoO_6$	$SFNi_{0.3}M$
Sr in $SFMCo_{0.5}$	La	$Sr_{1.9}La_{0.1}FeMo_{0.5}Co_{0.5}O_6$	$La_{0.1}$-$SFMCo_{0.5}$
		$Sr_{1.7}La_{0.3}FeMo_{0.5}Co_{0.5}O_6$	$La_{0.3}$-$SFMCo_{0.5}$
	Pr	$Sr_{1.9}Pr_{0.1}FeMo_{0.5}Co_{0.5}O_6$	$Pr_{0.1}$-$SFMCo_{0.5}$
		$Sr_{1.7}Pr_{0.3}FeMo_{0.5}Co_{0.5}O_6$	$Pr_{0.3}$-$SFMCo_{0.5}$
Sr in $SFMNi_{0.5}$	La	$Sr_{1.9}La_{0.1}FeMo_{0.5}Ni_{0.5}O_6$	$La_{0.1}$-$SFMNi_{0.5}$
		$Sr_{1.7}La_{0.3}FeMo_{0.5}Ni_{0.5}O_6$	$La_{0.3}$-$SFMNi_{0.5}$
	Pr	$Sr_{1.9}Pr_{0.1}FeMo_{0.5}Ni_{0.5}O_6$	$Pr_{0.1}$-$SFMNi_{0.5}$
		$Sr_{1.7}Pr_{0.3}FeMo_{0.5}Ni_{0.5}O_6$	$Pr_{0.3}$-$SFMNi_{0.5}$

Fe_2O_3 and MoO_3 were used as the starting materials to synthesize the $Fe_2Mo_3O_{12}$ intermediate to prevent the volatilization of MoO_3. Firstly, the stoichiometric amounts of Fe_2O_3 and MoO_3 were thoroughly mixed and heated at 12°C·min^{-1} up to 750°C for 12 hours [46]. Next, the starting mixtures of $SrCO_3$, Fe_2O_3,

$Fe_2Mo_3O_{12}$, Co_3O_4, Pr_6O_{11}, La_2O_3 and NiO were ground and calcined in air at 1000°C for 12 hours. After that, the calcined powder was re-ground and 2 g of the resulting powder was subsequently loaded into a die with the cavity of 2 cm in diameter. The die was constantly and isostatically pressed up to 98 MPa for 5 minutes by the hydraulic pump to obtain a disk. Finally, the disk was sintered at 1300°C in air with the heating rate of 3.4°C·min^{-1} for 12 hours to obtain the dense ceramic disk.

2.2.2 Cathode preparation [47]

In this research, $Sr_{0.5}Sm_{0.5}CoO_6$ (SSC) was employed as the cathode and prepared by the combination of the citrate and ethylenediamine tetraacetic acid (EDTA) complexing method. Firstly, EDTA, the complexing agent, was dissolved in distilled water and the pH of solution was adjusted to 7 by the addition of 25 wt% ammonia water to form EDTA-NH_3-H_2O under vigorously stirring. Secondly, in a separate solution, $Sr(NO_3)_2$, $Sm(NO_3)_3{\cdot}6H_2O$ and $Co(NO_3)_3{\cdot}6H_2O$ were dissolved in distilled water to give a dark reddish solution and then the solution was poured into the EDTA-NH_3-H_2O solution. After 30 minutes, the solution of citric acid was introduced and the molar ratio of the total *metal ions*: *EDTA*: *citric acid* was controlled to be around 1 : 1.1 : 3. Finally, the pH value of the final solution was adjusted to 7 again and the solution was stirred overnight at room temperature prior to the addition of NH_4NO_3 solution. The resulting solution was evaporated on a hot plate and the black product was achieved. The black product was then decomposed at 400°C for 2 hours. After that, the obtained powder was ground and sintered at 1000°C for 5 hours.

2.2.3 Electrolyte preparation [48]

Due to the higher ionic conductivity than those of the commonly used electrolytes, the perovskite with the composition of $La_{0.9}Sr_{0.1}Ga_{0.8}Mg_{0.2}O_3$ (LSGM) was used as an electrolyte and prepared by a solid-state reaction using La_2O_3, $SrCO_3$, Ga_2O_3, and MgO. The starting materials were mixed and homogenized in a mortar and subsequently calcined at 1000°C in air for 6 hours. The calcined powders were then re-ground and pressed isostatically at 325 MPa for 30 minutes in order to form a cylindrical disk (2 cm in diameter). The disks were sintered at 1500°C in air for 5 hours and then rubbed off to the thickness of 0.3 mm by a diamond grinding machine.

2.3 Material characterization

2.3.1 X-ray diffractrometry (XRD)

The phase structure of the prepared oxide was carried out using Rigaku, DMAX 2002 Ultima Plus X-Ray powder diffractometer equipped with a monochromator and a Cu-target X-ray tube (40 kV, 30 mA). The angles of two-theta ranged from 20 to 70 degree (scan speed of 5 degree·min^{-1}) were recorded, at Department of Chemistry, Faculty of Science, Chulalongkorn University.

2.3.2 Scanning Electron Microscopy (SEM)

The morphology of the sintered oxide was studied using a JEOL JSM- 5800LV scanning electron microscopy, Oxford Instrument (model Link ISIS series 300) at Faculty of Science, Chulalongkorn University.

2.3.3 X-ray photoelectron spectroscopy (XPS)

To assess the surface chemical properties, a rectangular (12 mm x 5 mm x 2 mm) of sintered oxide was characterized by a Kratos Axis Ultra X-ray photoelectron spectrometer using a monochromatic Al Kα (1486.6 eV) as an X-ray source and a pass energy of 40 eV at The Petroleum and Petrochemical College, Chulalongkorn University. The analysis chamber was pressurized and controlled around 10^{-7}-10^{-9} Torr during the measurement. The binding energies of elements were recorded and calibrated relative to the C1s reference peak at 284.6 eV.

2.3.4 Dilatometry

A dilatometer, LINSEIS L75 Platinum Series, (at Ministry of Science and Technology, Thailand) was used to determine the thermal expansion coefficient (TEC) of the specimen with approximate dimensions of the same as that used for XPS specimens. In this measurement, the heating rate was kept at 3ºC·min^{-1} and the temperature measurement ranged from room temperature to 1000ºC in air.

2.3.5 Electrical conductivity measurement [49]

The electrical conductivity of materials was investigated by the DC four-point probes method. A disk of sintered-oxide was cut into a rectangular shape with approximate dimensions of 12 mm x 5 mm x 1.5 mm. Pt wires were employed as an electrode: the two-wire outer of the specimen was corresponded to the current-Pt probes and the two wires between the outer probes were related to the voltage probes as shown in Figure 2.1. These wires were attached to the specimen using Pt

past as a binder and heated at 950°C for 10 minutes with a heating rate of 5°C·min^{-1} to gain a good electronic contact specimen. After applying a DC current (I) through the current probes over the temperature range of 300°C to 800°C in air, the difference in voltage, V were measured by an Autolab PGSTAT302N potentiostat/galvanostat. The data was calculated using the equation 2.1:

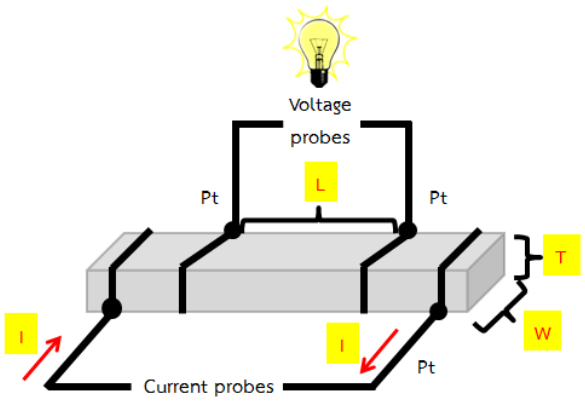

Figure 2.1 DC four-probes measurement

$$\sigma = \frac{I}{V} \times \frac{L}{W \times T} \qquad (2.1)$$

Where σ is electrical conductivity (S·cm^{-1})
I is applied DC current (A)
L is length between two inner probes (cm)
V is different voltage between two outer probes (V)
W is width of rectangular specimen (cm)
T is thickness of rectangular specimen (cm)

2.3.7 Oxygen permeation measurement

Oxygen permeation measurement is used to evaluate the ability of sintered membranes to permit oxygen gas from one side through the other side driven by the oxygen partial pressure gradient across the membrane as previously stated in Chapter I.

According to membrane preparation, the thickness of the disks used as membrane was polished to 0.3 mm by a diamond grinding machine. The polished membranes were then placed on the vertical alumina tubes using an o-ring glass as a sealant to prevent leakage as shown in Figure 2.2. In the beginning step of the

measurement, the assembly was fired at a rate of 5°C·min^{-1} up to 1000°C and held for 10 minutes to seal the alumina tubes. Then, the measurement was employed in temperature range of 650-1000°C by adjusting the heating rate of 5°C·min^{-1}. Air zero was purged into one side of the membrane-disk to achieve the oxygen-rich side at a flow rate of 100 mL·min^{-1} whereas the other side was exposed to helium gas (99.999%) which was not only as a sweep gas to produce an oxygen partial pressure gradient but also as the carrier gas for transportation of the permeated oxygen. The permeated oxygen was consequently injected into a gas chromatograph (Agilent, 6820A) equipped with a 5Å capillary column joining to the end of the sweep side and examined by thermal conductivity detector. The oxygen permeation flux was carried out using the measured outlet flow rate and calculated using the equation 2.2:

$$J_{O_2}(\text{mol}\cdot\text{cm}^{-1}\cdot\text{s}^{-1}) = \left[C_{O_2} - C_{N_2} \times \frac{0.21}{0.79} \times \left(\frac{28}{32}\right)^{1/2}\right] \times \frac{F}{S} \qquad (2.2)$$

Where C_O and C_N were the concentration of oxygen and nitrogen gas, respectively, measuring on the sweep side (mol·mL^{-1}), F is the gas flow rate exiting on the sweep side (mL·s^{-1}), and S is the effective area of the membrane on the sweep side (cm^2).

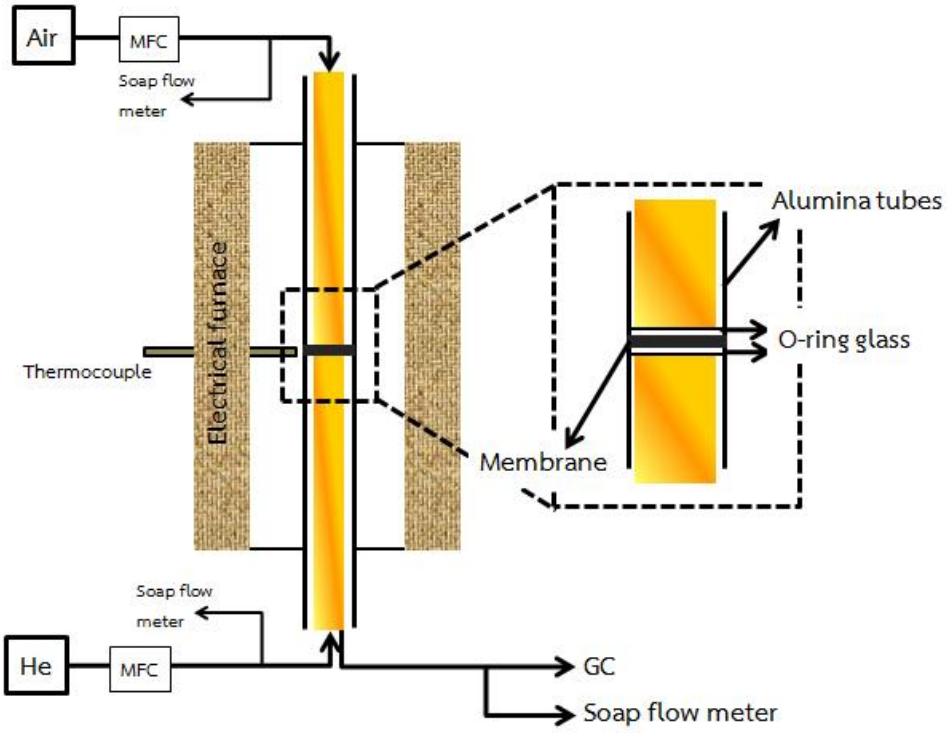

Figure 2.2 Schematic diagram of oxygen permeation measurement

2.3.8 SOFC performance test and AC impedance

Single cells were fabricated using 300-μm thick LSGM as the electrolyte, SSC perovskite as the cathode and the synthesized oxides as the anodes. The anode materials and SSC were both made into slurries using a binder (ethyl cellulose + isobutyrate). Anode slurry was then applied onto one side of the LSGM disk by a screen printing technique and SSC slurry was subsequently applied onto the other side. Both cathode and anode were fired at 1000°C for 30 minutes for a good attachment of electrodes and electrolyte as a single cell. Then, the cell was placed on an alumina tube and sealed with a glass-ring sealant. At the reaction temperature of 600-800°C under ambient pressure, the cathode side was exposed to oxygen gas (99.99%) while the anode side was exposed to hydrogen gas (99.99%) at a flow rate of 100 mL·min^{-1} as schematically shown in Figure 2.3. The current-voltage (*i*-V) of the cells was measured using a HA-151B galvanostat and an U3402A Agilent multimeter whereas the AC impedance was recorded on the potentiostat mode of Autolab PGSTAT302N instrument equipped with a frequency response analyzer under open circuit conditions in the frequency range from 200 kHz to 0.1 Hz.

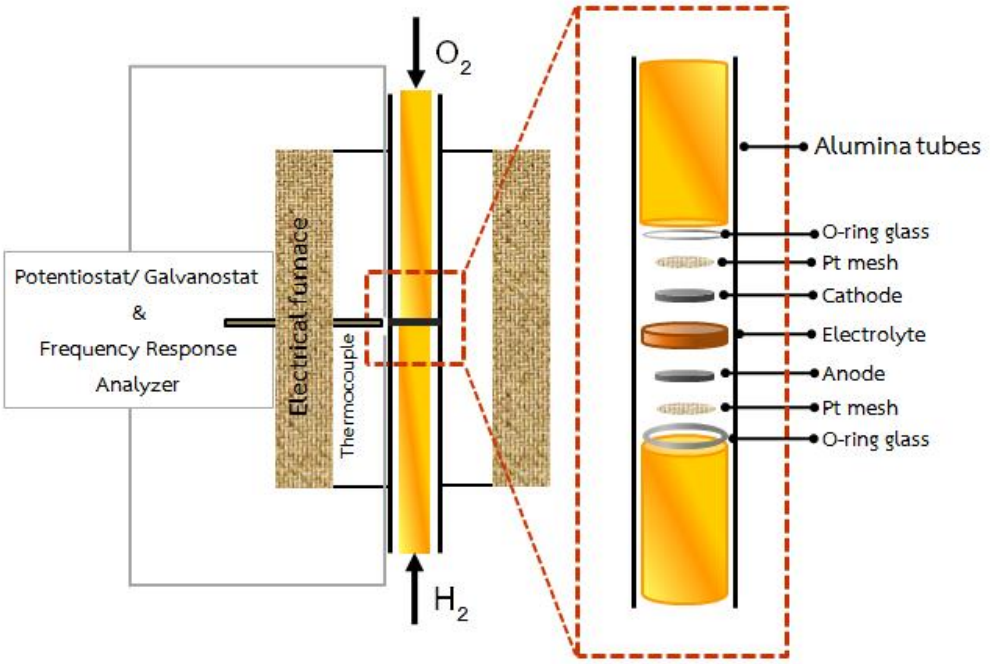

Figure 2.3 Schematic of the setup employing single cell for SOFC performance and AC impedance measurement

CHAPTER III
RESULT AND DISCUSSION

3.1 Characterization of $Sr_2FeMo_{1-x}M_xO_6$ (M = Co, Ni; X = 0.0-0.5)

3.1.1 XRD characterizations

Figure 3.1 depicts the XRD patterns of the SFMO, $SFMCo_x$ and $SFMNi_x$ oxide sintered at 1300°C for 12 hours in air. It is obviously seen that SFMO revealed the existence of the double-perovskite structure and the formation of $SrMoO_4$ impurity (JCPDS 08-0482). The appearance of $SrMoO_4$ phase can be found during the high-temperature preparation of SFMO in air [50]. Since the oxygen stoichiometry of 6 is attained when the Mo solubility limit is 17% ($Sr_2Fe_{1.34}Mo_{0.68}O_6$), the extra oxygen is accommodated in the $SrMoO_4$ phase [51]. When Co and Ni were substituted at the Mo site, the peak intensities of impurity phase became weaker, as observed from the peak at two-theta degree of 27.7. The main diffraction peaks of $SFMCo_x$ and $SFMNi_x$ at two-theta degree of 32.2 shifted to the lower values of two-theta compared to the un-doped one, indicating the lattice expansion caused by the substitution of Co and Ni in the structure. The reason for this is the difference in the ionic radii of the main element and the dopant. When the large ionic radii (Co^{2+} = 0.65 Å, Ni^{2+} = 0.69 Å) was introduced into the Mo site (Mo^{6+} = 0.59 Å, Mo^{5+} = 0.61 Å), the lattice was expanded resulting in an increase in the unit cell parameters; the diffraction peaks consequently shifted to the lower value of two-theta degree related to Bragg's Law. When the doping amount of Co and Ni was at x = 0.5, the $SrMoO_4$ impurity peaks became disappeared and the $SFMCo_{0.5}$ and $SFMNi_{0.5}$ were found to be phase-pure which contributes to the solubility limit of Mo formerly explained. The depletion of impurity phase $SrMoO_4$ as a function of dopant illustrated in Figure 3.2, indicates the introduction of Co and Ni at the Mo site reduces the $SrMoO_4$ phase in the prepared oxides. Furthermore, at the composition of x = 0.5, the main diffraction peak was shifted to higher values of two-theta degree, suggesting the shrinkage of the structure. This could be because the introduction of the low valence ion (Co^{2+} and Ni^{2+}) can induce the oxidation state of B-site cations from Fe^{2+} to Fe^{3+} in order to balance the electrical neutrality. The charge compensation occurs from a combination of Fe^{2+} ($3d^6$)/Mo^{6+} ($4d^0$), or of Fe^{3+} ($3d^5$)/Mo^{5+} ($4d^1$), or a mixture of these two forms. As a consequence, the B-O bond length will decrease and the bond strength increases regarding to the valence bond theory.

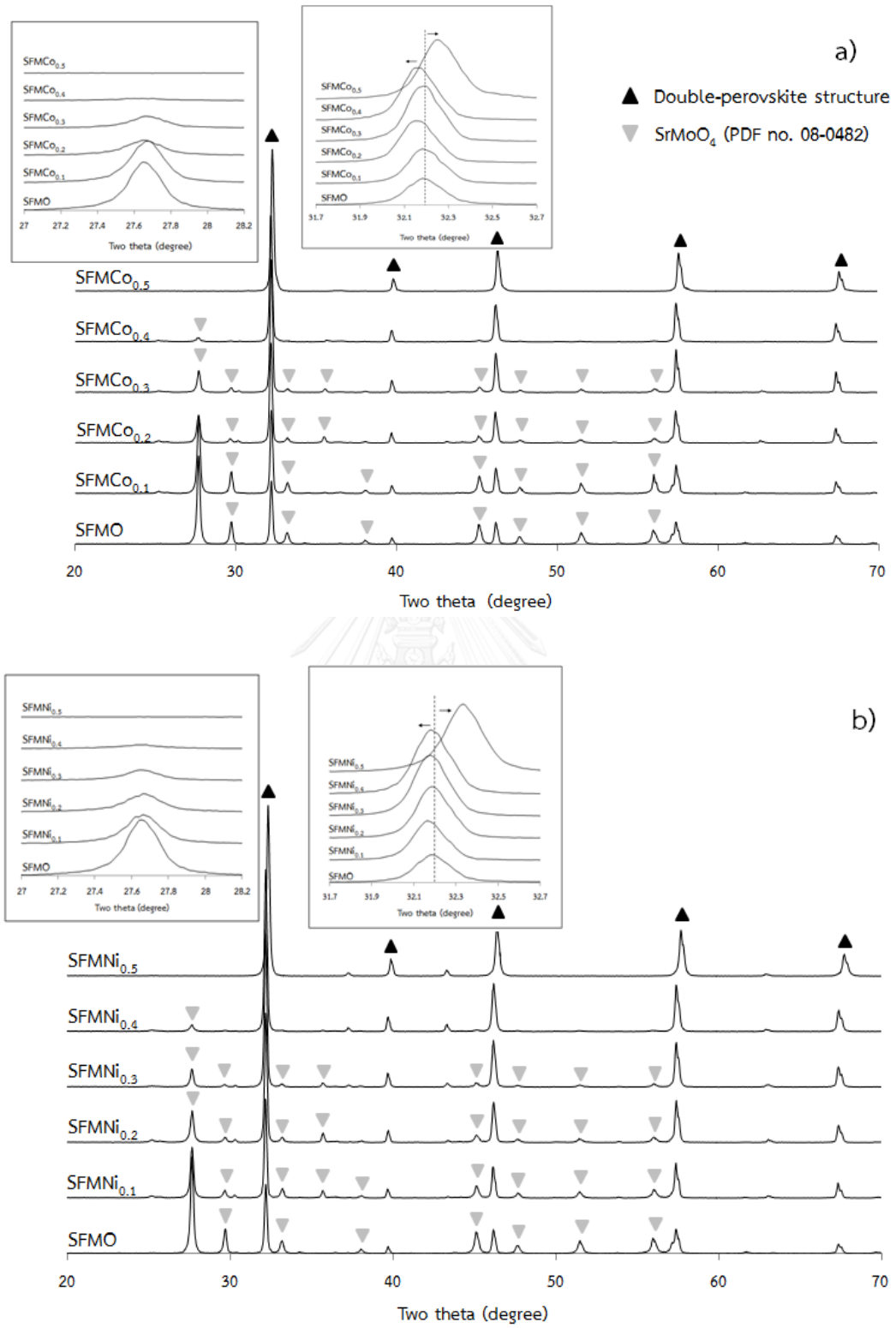

Figure 3.1 XRD patterns of a) $SFMCo_x$ and b) $SFMNi_x$ oxides sintered in air at 1300°C for 12 hours

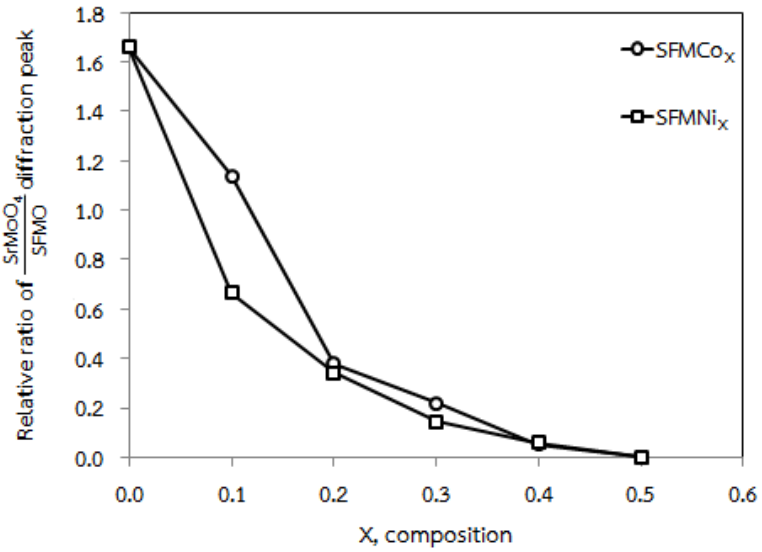

Figure 3.2 Relative ratios between the main diffraction peak of $SrMoO_4$ impurity and the main diffraction peak of double perovskite structure as a function of dopant composition

3.1.2 Electrical conductivity measurement

Figure 3.3 shows the temperature dependence on electrical conductivity of $SFMCo_x$ and $SFMNi_x$ in air from 300°C to 800°C the data are tabulated in Table 3.1-3.2.

It can be seen that both $SFMCo_x$ and $SFMNi_x$ have the similar trend on electrical conductivity. The electrical conductivity of all specimens increased with increasing temperature, exhibiting the typical semiconducting-like conduction behavior. In this work, the appearance of $SrMoO_4$ impurity phase is negligible because it is an insulator [50]. The electrical conductivity also increased with increasing the metal-doped content, which is due to the formation of small band gap between the 3d band of doped-ions and the 2p band of O ions that easily promotes electrons to jump from valence band to conduction band [52]. Moritomo et al. [53] also mentioned that the Mo—O bond length can play an important role in perovskite oxide; the shrinkage of Mo—O bond results in the enhancement of hybridization between the Mo 4d and O 2p orbitals. As a result, electrons easily transfer from O 2p orbital to Mo 4d orbital. In this study, the highest electrical conductivity values of 32.93 $S{\cdot}cm^{-1}$ and 50.11 $S{\cdot}cm^{-1}$ were observed from $SFMCo_{0.5}$ and $SFMNi_{0.5}$, respectively, which may consequently be the results of the 3d:2p band overlapping and the shrinkage of the structure as observed in the XRD patterns. In addition, Liu

[54] reported that the electronic conductivity can be influenced by the main oxidation state of Mo +6 with a small portion of Mo +5 via the equilibrium reaction of $Fe^{3+} + Mo^{5+} = Fe^{2+} + Mo^{6+}$ [55]. Since the XPS analysis of Mo 3d in this study indicated that Mo^{+6} is the main composition, the electronic conductivity in these materials is mainly contributed from Mo^{+6}.

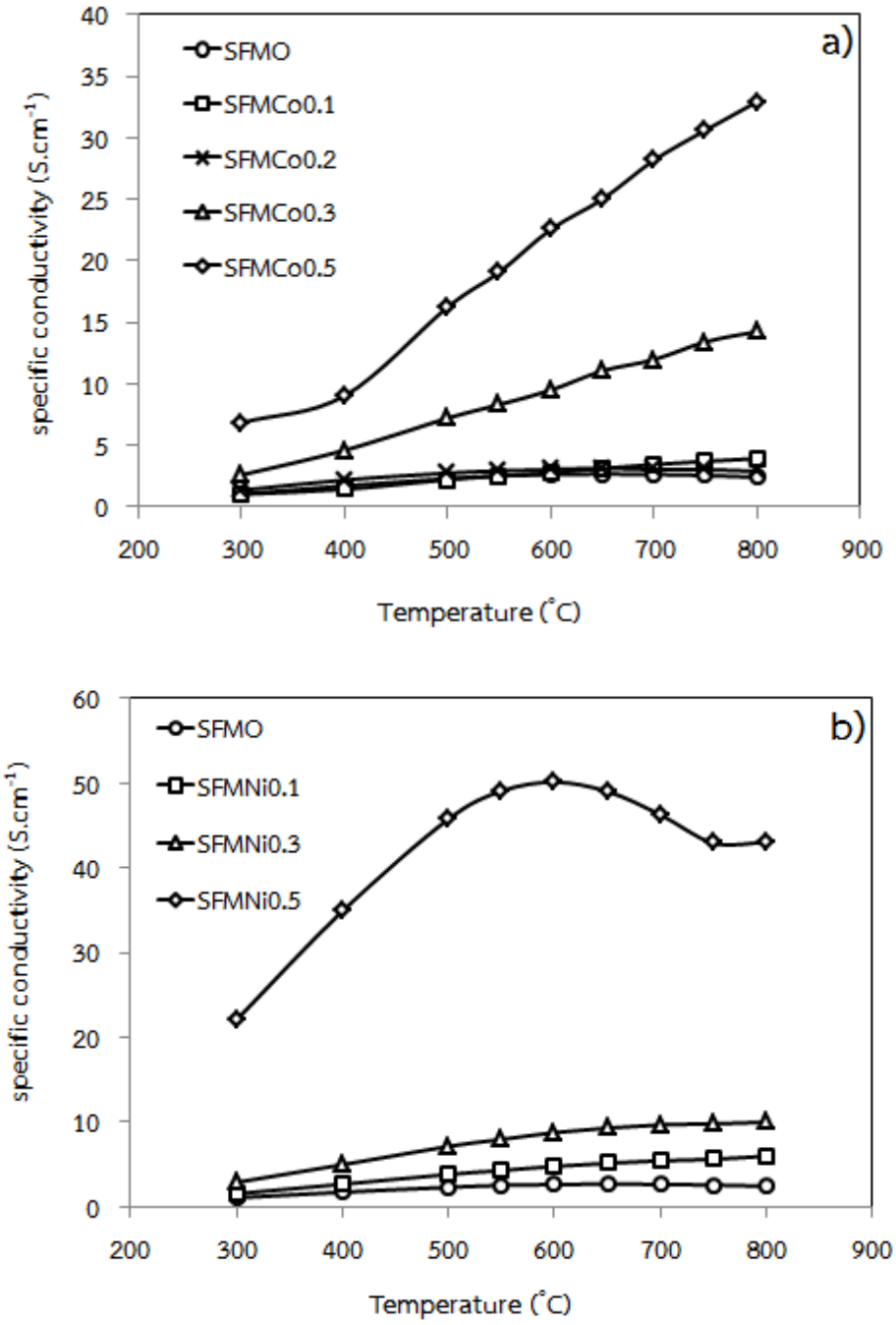

Figure 3.3 Temperature dependence on conductivity of (a) $SFMCo_x$ and (b) $SFMNi_x$ in air

Furthermore, as temperature increases, the lattice oxygen can be lost (O_o^x), contributing to the oxygen vacancies ($V_o^{\cdot\cdot}$) and the partial reduction of Mo^{6+} (Mo_{Mo}^x) to Mo^{5+} ($Mo_{Mo}^{'}$) ions, which can be defined by equation 3.1 [56]:

$$2Mo_{Mo}^x + O_o^x \leftrightarrow 2Mo_{Mo}^{'} + V_o^{\cdot\cdot} + 1/2O_2(g) \quad (3.1)$$

Table 3.1 The specific conductivity of $SFMCo_x$ (x = 0-0.5)

Oxide	Specific conductivity ($S{\cdot}cm^{-1}$)							E_a (eV)
	300°C	400°C	500°C	600°C	700°C	800°C	max	
SFMO	1.05	1.71	2.30	2.63	2.64	2.42	2.68	0.379
$SFMCo_{0.1}$	1.02	1.43	2.22	2.77	3.45	3.94	3.94	0.146
$SFMCo_{0.2}$	1.36	2.19	2.74	3.05	3.04	2.90	3.14	0.214
$SFMCo_{0.3}$	2.60	4.60	7.22	9.50	11.97	14.25	14.25	0.248
$SFMCo_{0.5}$	6.85	9.03	16.25	22.56	28.18	32.93	32.93	0.244

However, the mobility of oxygen vacancies is low compared to the electron delocalization; therefore, the conductivity depends strongly on the concentration of the delocalized electrons.

From the Arrhenius plot of electrical conductivity presented in Figure 3.4, the activation energy (E_a) of electronic conduction as a function of metal-doped content can be derived from the fitted slope using equations 3.2 and 3.3.

$$\boldsymbol{\sigma = \frac{A}{T}\, exp\, \frac{-E_a}{RT}} \quad (3.2)$$

$$\boldsymbol{E_a = kT} \quad (3.3)$$

Where A is a constant, R is the gas constant, k is the Boltzman constant and T is the absolute temperature. The calculated data was summarized in Tables 3.1 and 3.2.

Table 3.2 The specific conductivity of $SFMNi_x$ (x = 0-0.5)

Oxide	Specific conductivity ($S \cdot cm^{-1}$)							E_a (eV)
	300°C	400°C	500°C	600°C	700°C	800°C	max	
SFMO	1.05	1.71	2.30	2.63	2.64	2.42	2.68	0.379
$SFMNi_{0.1}$	1.54	2.67	3.82	4.78	5.44	5.98	5.98	0.208
$SFMNi_{0.3}$	2.89	4.97	7.12	8.76	9.67	9.99	9.99	0.199
$SFMNi_{0.5}$	22.06	34.90	45.77	50.11	46.27	43.02	50.11	0.136

The linear relationship obtained from ln (σT) and 1000/T indicates the conduction mechanism as the small polaron hopping mechanism [57]. The decrease of E_a value when the dopant was introduced suggests that the incorporation of Co and Ni facilitates the electron migration. And, the reduction of E_a with increasing the metal-substituted content also indicates the smooth migration of the electrons, which is a result of the reduction of Mo—O bond length as observed from the XRD's result.

In the Ni-doped SFMO, $SFMNi_{0.5}$ showed the lowest E_a value which directly corresponds to the highest conductivity of the material. However, in case of Co-doped SFMO, the lowest E_a value was obtained from $SFMCo_{0.1}$ whereas the maximum conductivity was observed from $SFMCo_{0.5}$. This controversy may be caused by the difference in oxygen vacancy concentration as confirmed by the oxygen permeation flux's result. According to the experiment conducted by Sun et al. [58], the electrons could be trapped by the oxygen vacancies, which led to the decreased of electronic charge carrier concentration. And, since the electrical conductivity was also associated with the electronic carrier concentration, then the electronic conductivity decreased. In this work, $SFMCo_{0.1}$ showed the higher oxygen permeation flux than that of $SFMCo_{0.5}$, which implies that $SFMCo_{0.1}$ should have more oxygen vacancy than $SFMCo_{0.5}$. Therefore, electrons in $SFMCo_{0.1}$ were supposedly trapped by the oxygen vacancy resulting in the decrease of electronic conductivity.

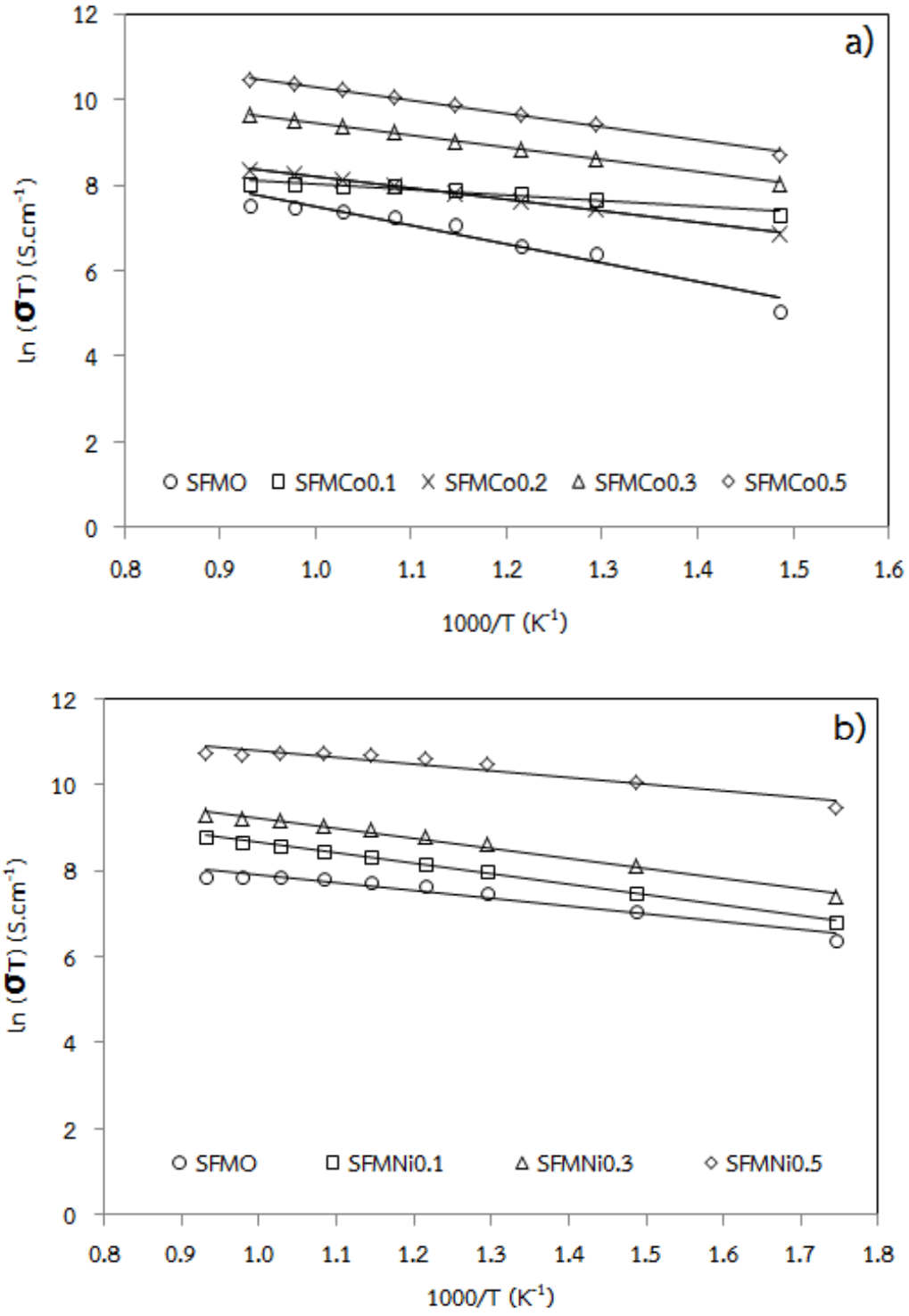

Figure 3.4 Arrhenius plots for the electrical conductivity of (a) $SFMCo_x$ and (b) $SFMNi_x$ at 300-800°C

3.1.3 Single cell performance

The LSGM electrolyte-supported single fuel cells with the configuration of $SFMCo_x$/ LSGM/ SSC and $SFMNi_x$/ LSGM/ SSC were tested using humidified H_2 and O_2 as a fuel and an oxidant, respectively. Figure 3.5 shows the cell voltage and the power density at 800°C. It is clearly seen that the performance of the cell using SFMO anode was enhanced by Co-, and Ni-doped anode. The highest power densities of 802 $mW{\cdot}cm^{-2}$ and 723 $mW{\cdot}cm^{-2}$ were obtained from the cells using $SFMCo_{0.2}$ and $SFMNi_{0.1}$ anode, respectively. This may be because $SFMNi_{0.1}$ and $SFMCo_{0.2}$ have higher oxygen mobility compared to others as seen in oxygen permeation results, which enhances the rapidly transport of oxygen through the materials and extends TPB. Nevertheless, in this work, the highest values of conductivity were obtained from $SFMCo_{0.5}$ and $SFMNi_{0.5}$ but the cell performance was low. Therefore, it can be suggested that the conductivity of the anode is not the main factor affecting the cell performance. Other factors such as conductivity of electrolyte, activity of cathode, thermal compatibility and so on could be accounted for the performance of the cell.

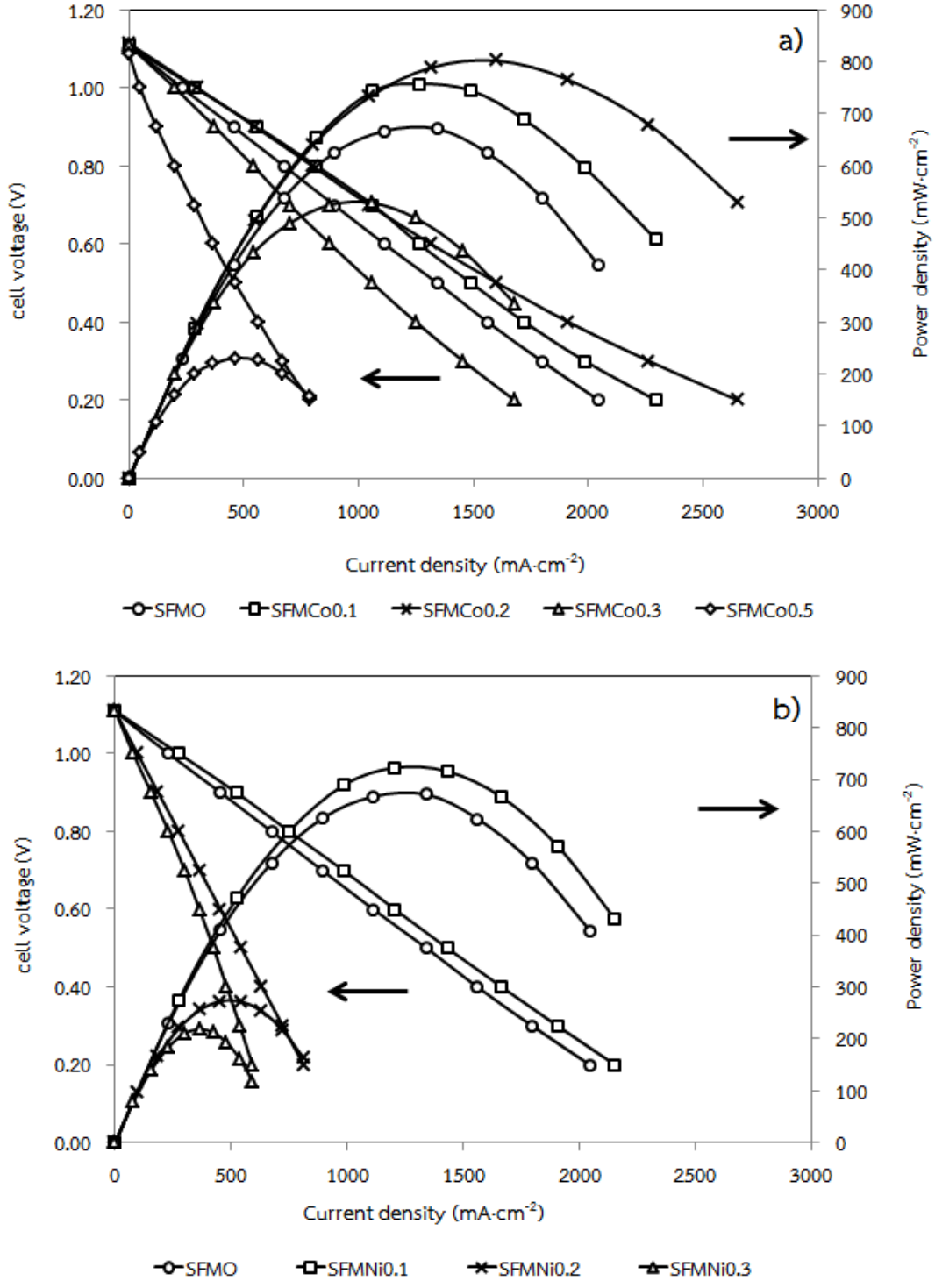

Figure 3.5 The single cell performance of cells a) $SFMCo_x$ /LSGM /SSC and b) $SFMNi_x$ / LSGM/ SSC at 800°C

3.1.4 Electrochemical impedance

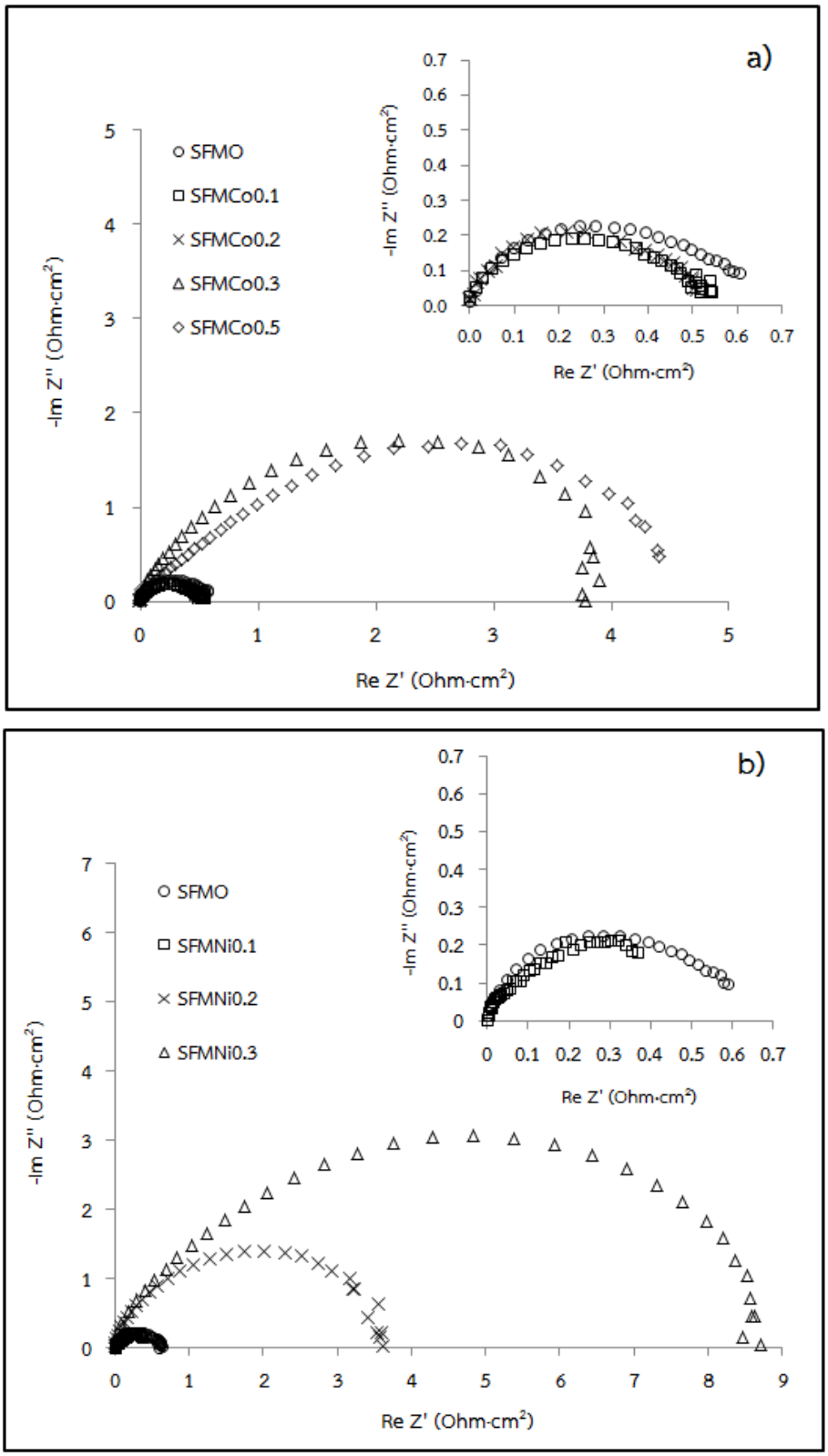

Figure 3.6 Relative impedance spectra of cells at 800°C a) $SFMCo_x$/ LSGM/ SSC and b) $SFMNi_x$/ LSGM/ SSC

From the Nyquist plot of the cell in Figure 3.6, the interception of the semicircle at high and low frequency regions on Re Z' axis are recognized as the ohmic resistance (R_{ohm}) and the total resistance (R_{total}) of the cell, respectively. The width between the high and the low frequency intercept is the polarization resistance (R_p), which mainly correlates to the adsorption, diffusion, and charge transfer process on the electrodes [37]. The R_{ohm} resistance is mainly dominated from the electrolyte, the electrode, and the wire contact [30]. It is observed that the obtained polarization resistance values were in agreement with the cell performance test. The higher the power density of the cell, the lower the polarization resistance obtained which is the requirement of the electrode as shown in Table 3.3.

Table 3.3 The power density and the polarization resistance of LSGM-supported single cell with different anode materials at 800°C

Anodes	R_p ($\Omega \cdot cm^2$)	Power density ($mW \cdot cm^{-2}$)
SFMO	0.59	671
$SFMCo_{0.1}$	0.54	758
$SFMCo_{0.2}$	0.51	802
$SFMCo_{0.3}$	3.65	529
$SFMCo_{0.5}$	4.42	231
$SFMNi_{0.1}$	0.50	723
$SFMNi_{0.2}$	3.60	273
$SFMNi_{0.3}$	8.72	218

Regards to the results on the cell performance and impedance of materials, SFMO, $SFMCo_{0.2}$, $SFMCo_{0.3}$, $SFMNi_{0.1}$ and $SFMNi_{0.3}$ were chosen for further investigation on the thermal expansion property, the oxygen transport property and the chemical state property.

3.1.5 Thermal expansion

The thermal expansion coefficient (TEC) is an important property for electrode materials because the mismatched TEC between electrodes and electrolyte may contribute to the delamination of the multi-layer during the long-term operating processes [59]. In this work, the TEC of all specimens were measured in the temperature range of 30-1000°C in air as shown in Figure 3.7. It is observed that the thermal expansion curves of $SFMCo_x$ and $SFMNi_x$ increased with increasing

temperature and a linear thermal expansion behavior was observed at temperature lower than 700°C while a non-linear thermal expansion behavior was presented at temperature higher than 700°C. At high temperature, the crystal lattice easily expands due to the increasing of bond length and the loss of lattice oxygen. As a result, a non-linear behavior is observed.

Table 3.4 The average TEC values for $SFMCo_x$ in different temperature ranges in air

Samples	TEC (x 10^{-6} K^{-1})		
	30-800°C	600-1000°C	30-1000°C
SFMO [37]	-	-	13.9
SFMO	13.3	14.9	13.7
$SFMCo_{0.1}$	13.9	15.3	14.2
$SFMCo_{0.2}$	14.1	15.8	14.7
$SFMCo_{0.5}$	15.6	18.2	16.0

After addition of Co and Ni in the SFMO structure, the average TEC values of $SFMCo_x$ and $SFMNi_x$ were slightly larger than that of SFMO anode as summarized in Table 3.4-3.5. This could be a result from the structural expansion because Ni^{2+} (0.69 Å) and Co^{2+} (0.65 Å) have the larger ionic radii than Mo (Mo^{6+} = 0.59 Å, Mo^{5+} = 0.61 Å). Thus when the temperature increased, the structure easily expanded. In case of $SFMCo_x$, the concentration of Co added can promote the lattice oxygen loss as reported by Kaus [60], leading to the increase in TEC. Generally, Co-based perovskite oxides exhibited high TEC values, for example, the TEC of $SrCo_{0.8}Fe_{0.2}O_3$ (SCF) is 30 x 10^{-6} K^{-1} at 20-900°C [61-63] but the TEC of $SFMCo_{0.1}$ and $SFMCo_{0.2}$ oxides in this study were not much different from SFMO and closed to that of the LSGM electrolyte (11.7 x 10^{-6} K^{-1}, 30-800°C), a common electrolyte used in SOFC. Thus, a good thermal compatibility can be achieved and no delamination occurs along the interface; as a result, high SOFC performance can be observed. On the other hand, the highest TEC value obtained from $SFMCo_{0.5}$ oxide may cause the incompatibility between materials, resulting in the lowest power density as confirmed by *i*-V-P curve's result.

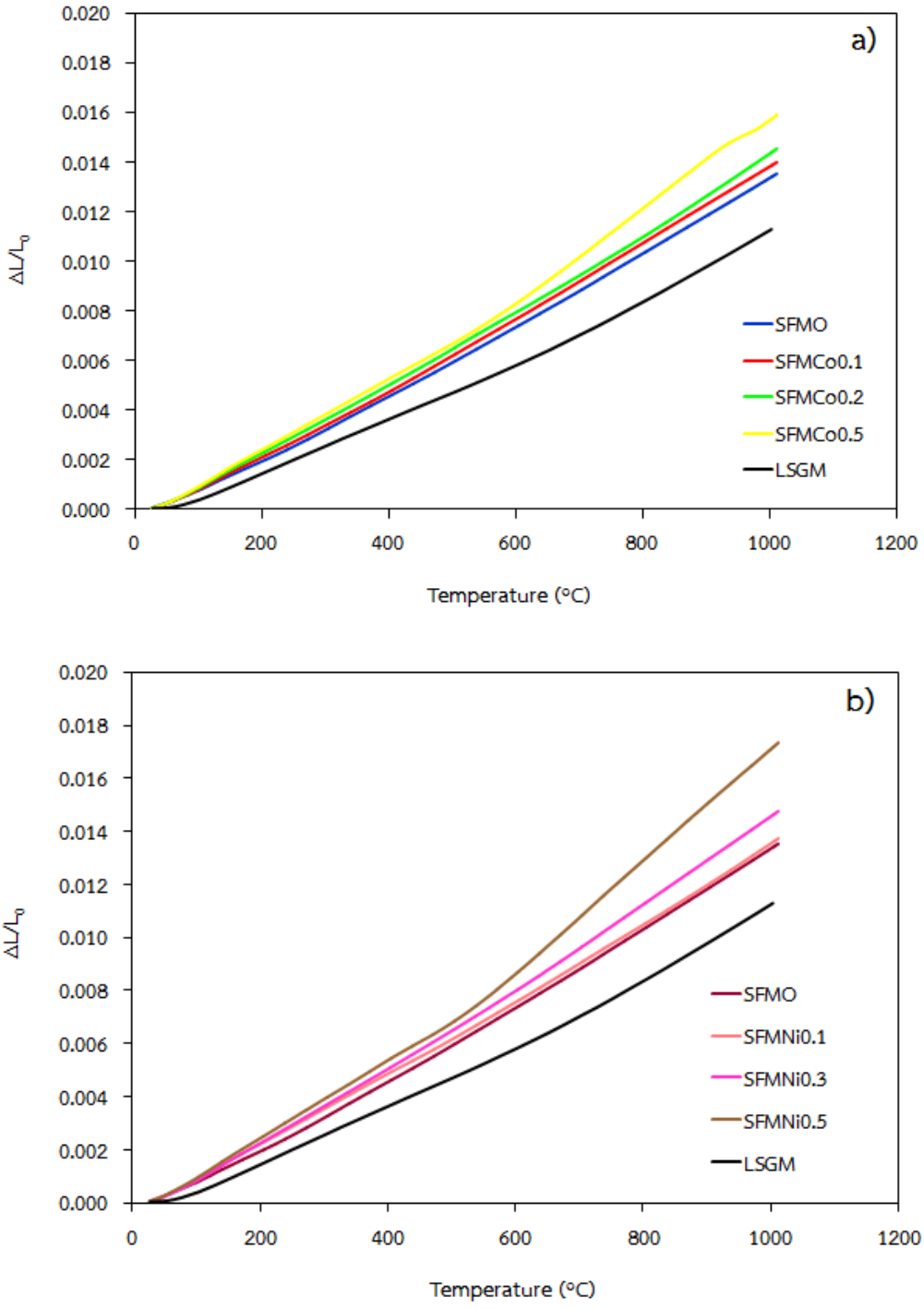

Figure 3.7 Thermal expansion curves of a) $SFMCo_x$ and b) $SFMNi_x$ as a function of temperature ranging from room temperature to 1000°C

Similar to the TEC value of $SFMCo_x$, the TEC values of $SFMNi_x$ anodes increased from 13.3 x 10^{-6} to 16.7 x 10^{-6} K^{-1} when x increased from 0 to 0.5. However, the average TEC of $SFMNi_{0.1}$ and $SFMNi_{0.3}$ are quite closed to those of LSGM electrolyte attributing to the high SOFC performance whereas $SFMNi_{0.5}$ has high TEC value which may cause a low power density of the cell. From the thermal expansion study, the materials with small amount addition of Co and Ni at Mo site can be used as anode materials of SOFC with LSGM electrolyte.

Table 3.5 The average TEC values for $SFMNi_x$ in different temperature ranges in air

Samples	TEC (x 10^{-6} K^{-1})		
	30-800°C	600-1000°C	30-1000°C
SFMO	13.3	14.9	13.7
$SFMNi_{0.1}$	13.5	14.8	13.9
$SFMNi_{0.3}$	14.5	16.3	14.9
$SFMNi_{0.5}$	16.7	21.0	17.5

3.1.6 Cross section analysis

The cross-section SEM images between the anodes and the LSGM electrolyte after cell performance testing are shown Figure 3.8-3.9. For the SFMO, $SFMCo_{0.1}$, $SFMCo_{0.2}$ and $SFMNi_{0.1}$ anodes, it is observed that there are no cracks along the interface between anodes and electrolyte, suggesting a good contact between the two materials. These results are the supportive data for the thermal compatibility result and the excellent electrochemical performance of the materials. However, in case of $SFMCo_{0.5}$ and $SFMNi_{0.3}$, the delamination of the two layers was observed and might be a cause of low SOFC performance as previously discussed.

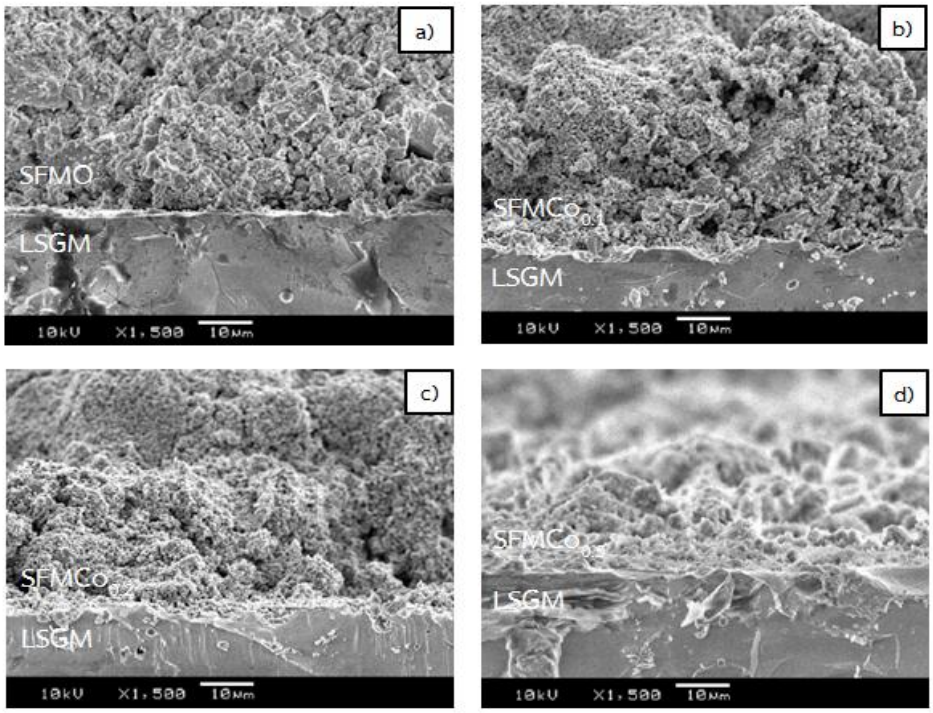

Figure 3.8 Cross-section images of $SFMCo_x$ (x = 0, 0.1, 0.2 and 0.5) anodes on LSGM electrolyte after cell performance testing a) SFMO b) $SFMCo_{0.1}$ c) $SFMCo_{0.2}$ and d) $SFMCo_{0.5}$

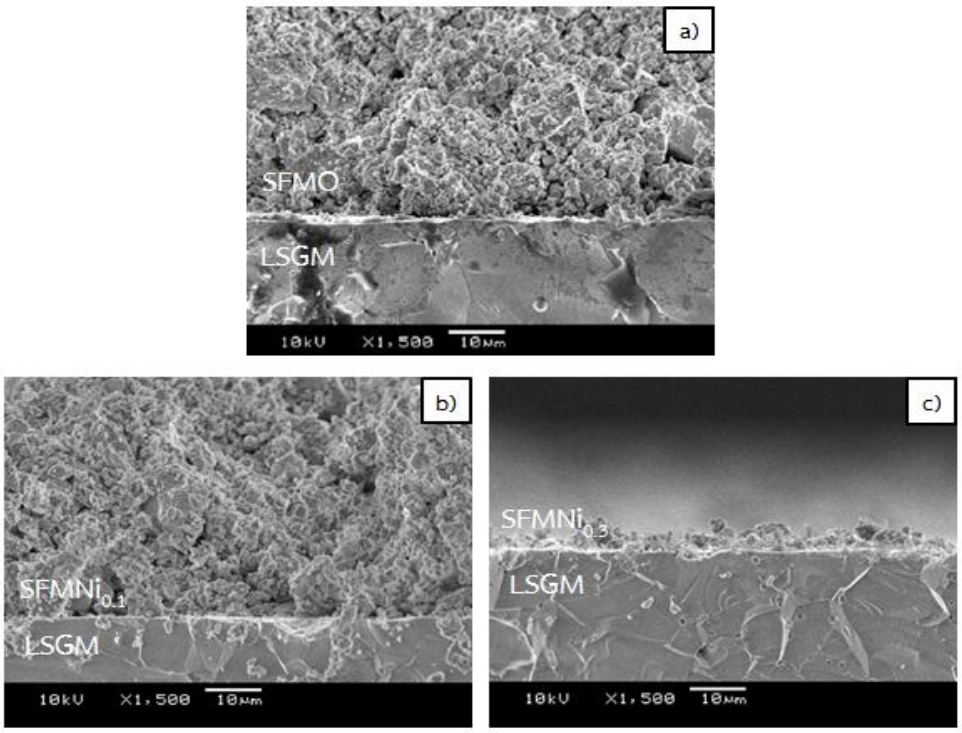

Figure 3.9 Cross-section images of $SFMNi_x$ (x = 0, 0.1, and 0.3) anodes on LSGM electrolyte after cell performance testing a) SFMO b) $SFMNi_{0.1}$ and c) $SFMNi_{0.3}$

3.1.7 Oxygen permeation measurement

The oxygen transport on perovskite membrane is controlled by two main factors: the oxygen surface exchange kinetic and the solid-state bulk diffusion or a combination of both. At high temperature, oxygen permeation is typically controlled by bulk diffusion whereas at lower temperature it is limited by the surface kinetics associated with adsorption/desorption, surface diffusion and charge transfer. This is because the activation energy of the surface is higher than the oxygen bulk diffusion [64].

The oxygen permeation fluxes of 300 μm-thick membranes were examined in the temperature ranging from 700 to 1000°C and the results are illustrated in Figure 3.10. Obviously, the oxygen permeability increased with increasing temperature, indicating oxygen permeation fluxes of all materials are mainly controlled by the bulk diffusion. At high temperature, the loss of lattice oxygen contributes to the increasing of concentration and mobility of oxide ion [41] and the decreasing of activation energy for the ion mobility and surface exchange [65]. Furthermore, it has been found that the oxygen permeability increased when the small amount of Co and Ni was introduced as x = 0.1 and 0.2 and then decreased when the Co and Ni was at x = 0.3. The increasing of oxygen permeation flux can be explained by the increase in concentration of oxygen vacancies which can facilitate oxide ion mobility [66]. In this study, at 800°C $SFMNi_{0.1}$ and $SFMCo_{0.2}$ showed the highest oxygen permeation fluxes of 0.645 $mL \cdot min^{-1} \cdot cm^{-2}$ and 0.263 $mL \cdot min^{-1} \cdot cm^{-2}$, respectively, which corresponds to the high cell performance of these materials in section 3.1.3. However, it is observed that in case of Co-doped materials, at temperature higher than 850°C, the oxygen permeation flux of $SFMCo_{0.1}$ was higher than that of $SFMCo_{0.2}$, suggesting $SFMCo_{0.1}$ may be a good candidate for high temperature anode material.

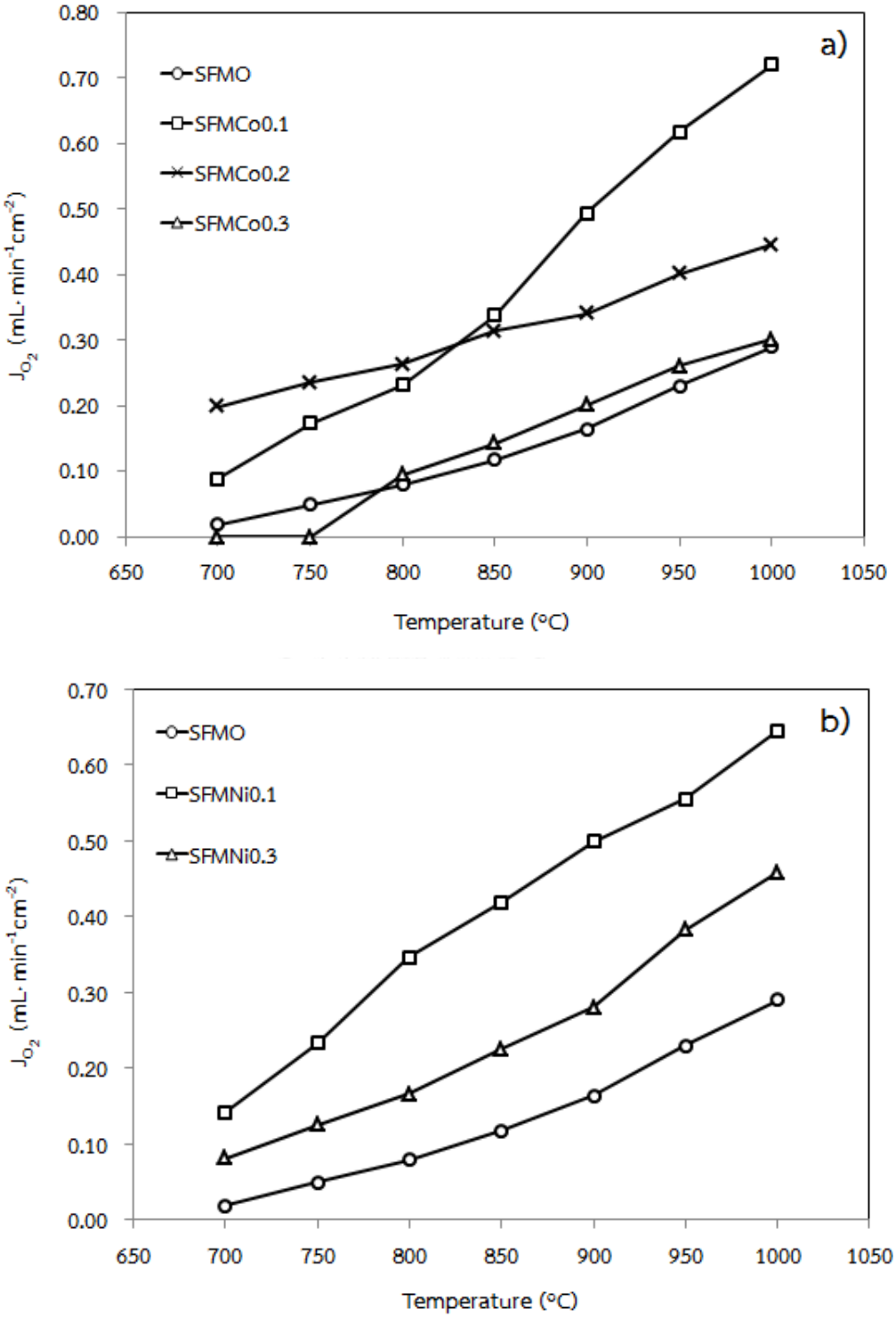

Figure 3.10 Temperature dependence of oxygen permeation for a) $SFMCo_x$ (x = 0-0.3) and b) $SFMNi_x$ (x = 0, 0.1, and 0.3) oxides

In addition, an apparent activation energy is also an important parameter for characterization of the oxygen permeability. It can be calculated from the slope of the oxygen flux logarithm ln (J_{O2}) plot against the reciprocal of absolute temperature as defined by equation 3.4 [66].

$$\ln (J_{O_2}) = \frac{-E_a}{RT} \quad (3.4)$$

Where J_{O2} is the oxygen flux, E_a is the apparent activation energy, R is the gas constant and T is absolute temperature. And, the calculated apparent E_a are summarized in Table 3.8.

As observed in Table 3.6, the activation energy of SFMO decreased by the metal-doping indicating the easier migration of O^{2-} from one site to the neighboring one, and increased with the more content of dopant. Additionally, the activation energy of 27.56 and 49.87 kJ·mol^{-1} were obtained from $SFMCo_{0.2}$ and $SFMNi_{0.1}$, respectively, which are lower than that reported oxide, LSCF4628, as 79.8 kJ·mol^{-1} [67]. Therefore, these materials are potential candidates for anode in SOFC.

Table 3.6 Activation energy (E_a) of $SFMCo_x$ and $SFMNi_x$ (x = 0-0.3) oxides at 700-1000°C

Samples	Activation energy (E_a, kJ·mol^{-1})
SFMO	90.85
$SFMCo_{0.1}$	71.56
$SFMCo_{0.2}$	27.56
$SFMCo_{0.3}$	67.05
$SFMNi_{0.1}$	49.87
$SFMNi_{0.3}$	58.82

3.1.8 X-ray Photoelectron analysis

The XPS analyses of Fe 2p, Mo 3d, and Co 2p on SFMO, $SFMCo_{0.2}$, and $SFMCo_{0.3}$ were performed and the spectra are illustrated in Figure 3.11-3.13. For Co 2p analysis, cobalt was in the mixed oxidation state of Co^0, $Co^{2+}$and Co^{3+} which can be seen in Figure 3.11. When x = 0.3, the peaks at binding energy around 777.8 eV and 794.8 eV demonstrated the Co $2p_{3/2}$ and Co $2p_{1/2}$ of Co^0, 780.4 eV and 794.9 eV represented Co^{2+}, and 786.4 eV and 796.6 eV represented Co^{3+}. When x = 0.2, only one weak broad peak was observed at 784.3 eV due to the relatively low Co doped

content. And, by the curves fitting, the binding energy around 777 eV, 781 eV and 786 eV may correspond to the Co^{0} $2p_{3/2}$, Co^{2+} $2p_{3/2}$ and Co^{3+} $2p_{3/2}$, respectively. Thus, it is concluded that Co has been incorporated into the structure and it exhibits as Co, Co^{2+} and Co^{3+}.

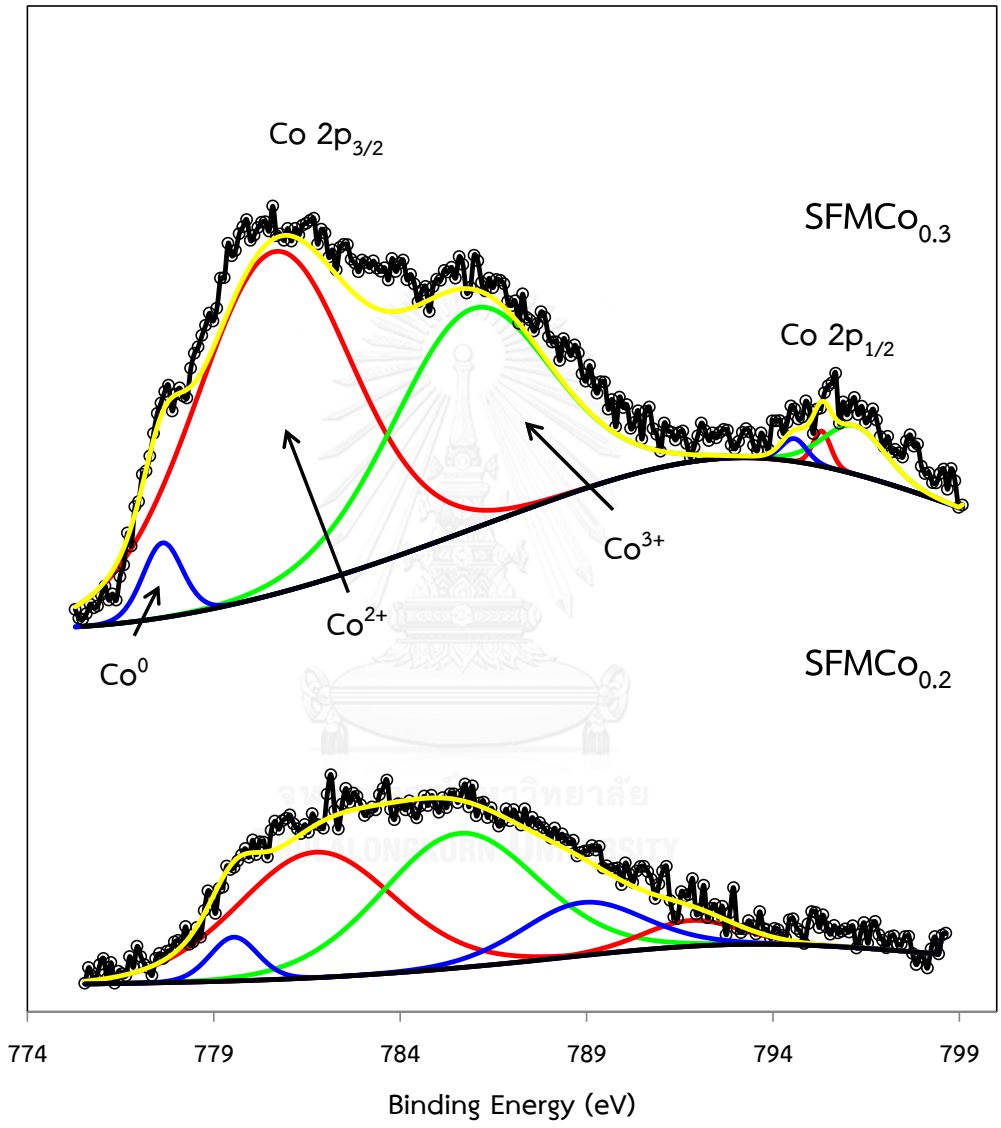

Figure 3.11 The Co 2p core-level spectra of $SFMCo_{0.2}$ and $SFMCo_{0.3}$ double perovskite

The XPS spectra of Fe 2p of SFMO, $SFMCo_{0.2}$ and $SFMCo_{0.3}$ is demonstrated in Figure 3.12. The broad peaks of Fe 2p were observed at binding energy around 709.2 eV (Fe $2p_{3/2}$) and higher energy around 722.6 eV (Fe $2p_{1/2}$). By the curve fitting, the Fe 2p components of SFMO and $SFMCo_{0.3}$ give rise to six peaks that are assigned to Fe^{0}

(705.6 eV and 719.5 eV), Fe^{2+} (710 eV and 723 eV) and Fe^{3+} (713.5 eV and 725 eV). While the Fe 2p of $SFMCo_{0.2}$ consists of two chemical species, Fe^{2+} and Fe^{3+}, at the binding energy of 710.4 and 723.9 eV for Fe^{2+} and at 713.7 eV and 725.8 eV for Fe^{3+}. In addition, the binding energy of Fe $2p_{3/2}$ increased with the Co content and the fitting curve extraction indicated the Fe^{2+}/ Fe^{3+} proportion as 10.558, 24.997 and 21.992 for SFMO, $SFMCo_{0.2}$ and $SFMCo_{0.3}$, respectively, as shown in Table 3.7.

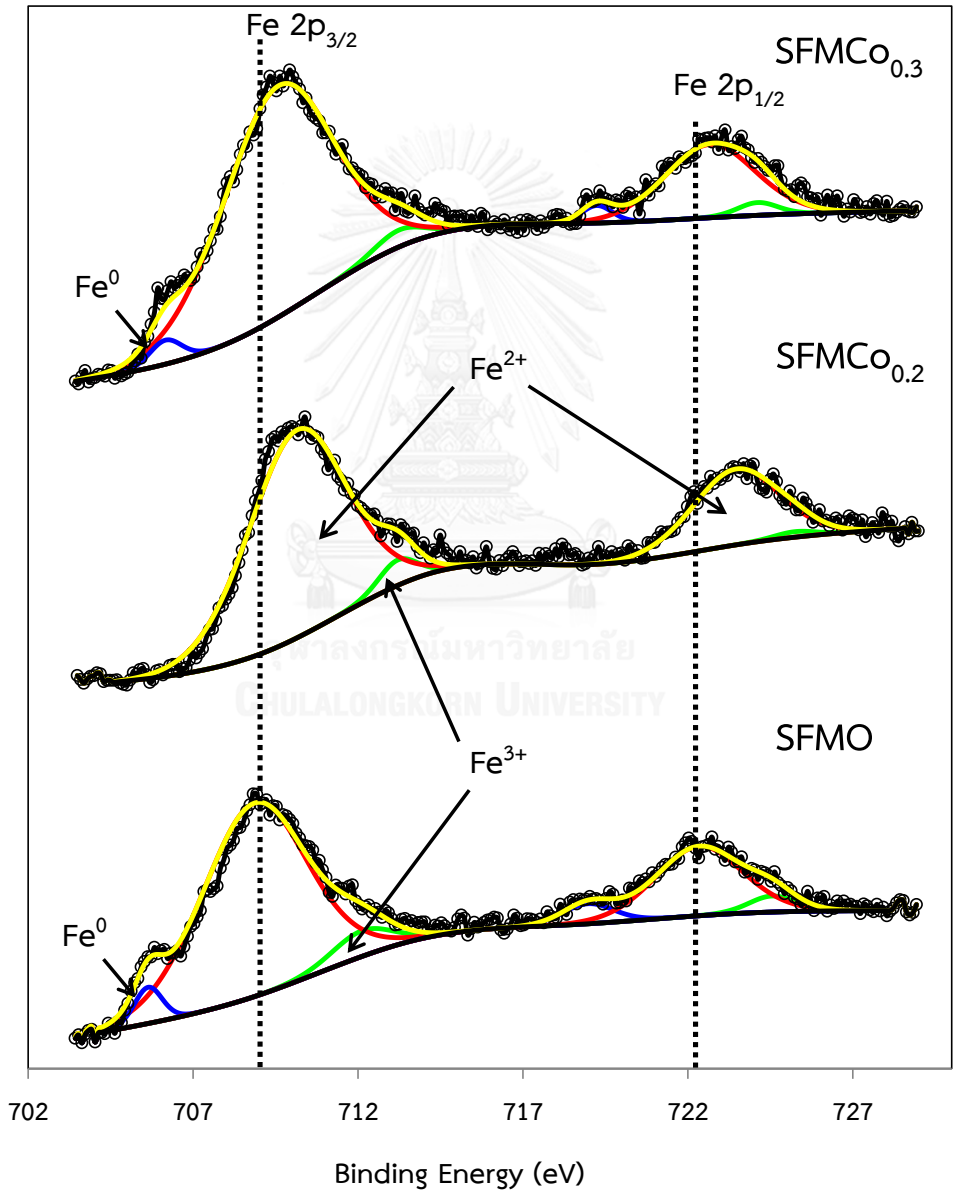

Figure 3.12 The Fe 2p core-level spectra of SFMO, $SFMCo_{0.2}$, $SFMCo_{0.3}$ double perovskite

Table 3.7 Chemical state of Fe 2p in $SFMCo_x$

Samples	Fe $2p_{3/2}$			Fe $2p_{1/2}$			Fe^{2+}/ Fe^{3+}
	Fe^0	Fe^{2+}	Fe^{3+}	Fe^0	Fe^{2+}	Fe^{3+}	ratio
SFMO	547	10977	839	558	3262	406	10.558
$SFMCo_{0.2}$	-	11057	524	-	3525	122	24.997
$SFMCo_{0.3}$	423	13989	448	292	3585	281	21.992

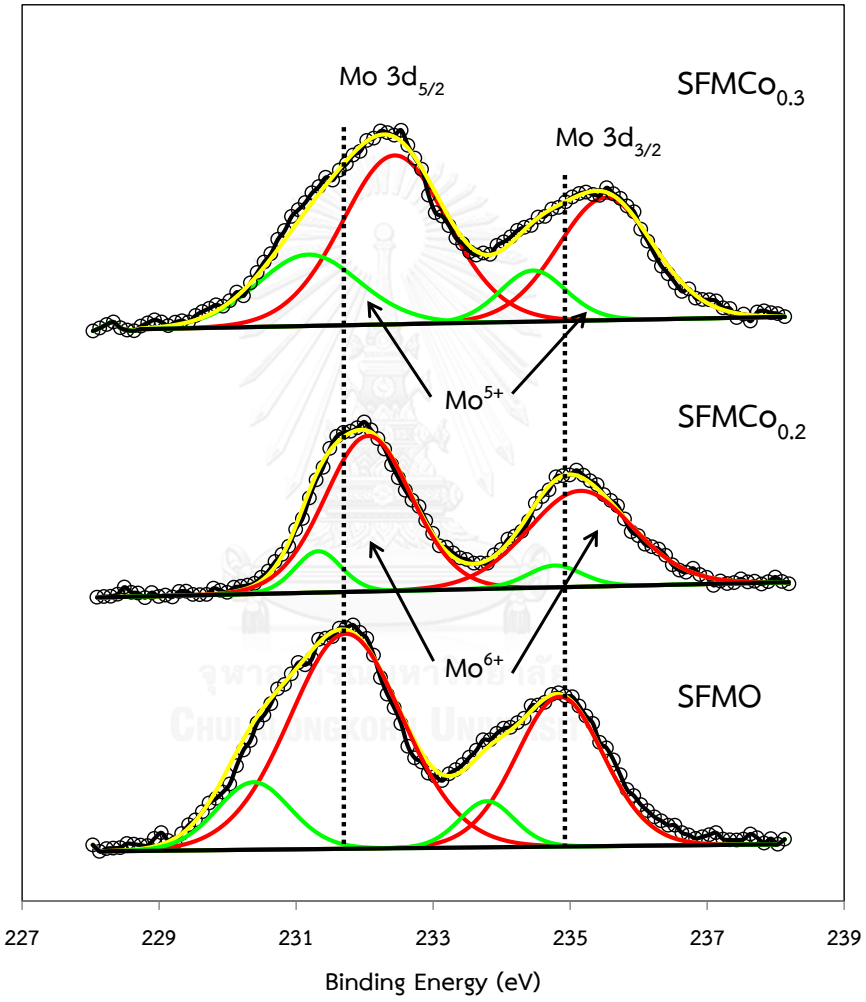

Figure 3.13 The Mo 3d core-level spectra of SFMO, $SFMCo_{0.2}$, $SFMCo_{0.3}$ double perovskite

Figure 3.13 illustrates two broad peaks of the Mo 3d XPS spectra at binding energy around 231.8 eV (Mo $3d_{5/2}$) and 235.0 eV (Mo $3d_{3/2}$). The fitting curves of Mo 3d spectra revealed the mixed chemical states of Mo^{6+} and Mo^{5+}. The fitted peaks of Mo^{6+} $3d_{5/2}$ and Mo^{6+} $3d_{3/2}$ were observed at 232.0 eV and 235.0 eV, respectively, and

the peaks of Mo^{5+} were at 230.4 eV and 233.8 eV. The proportion of Mo^{6+} and Mo^{5+} was calculated and summarized in Table 3.8.

Table 3.8 Chemical state of Mo 3d in $SFMCo_x$

Samples	Mo $3d_{5/2}$		Mo $3d_{3/2}$		Mo^{6+} / Mo^{5+}
	Mo^{6+}	Mo^{5+}	Mo^{6+}	Mo^{5+}	ratio
SFMO	3874	788	2089	402	5.056
$SFMCo_{0.2}$	2149	304	1606	189	7.783
$SFMCo_{0.3}$	2835	1161	1872	536	2.967

In this study, the $SFMCo_{0.2}$ anode showed the highest SOFC performance. This may be explained by the highest proportion of Fe^{2+}/ Fe^{3+} and Mo^{6+}/ Mo^{5+} ratio that influences on the reaction equilibrium of Fe^{3+} + Mo^{5+} = Fe^{2+} + Mo^{6+} as mention by Dai [55]. Moreover, the amount of Fe^{0} and Mo^{4+} species were not detected in this composition. In conclusion, the incorporation of Co can improve the electrochemical properties of SFMO.

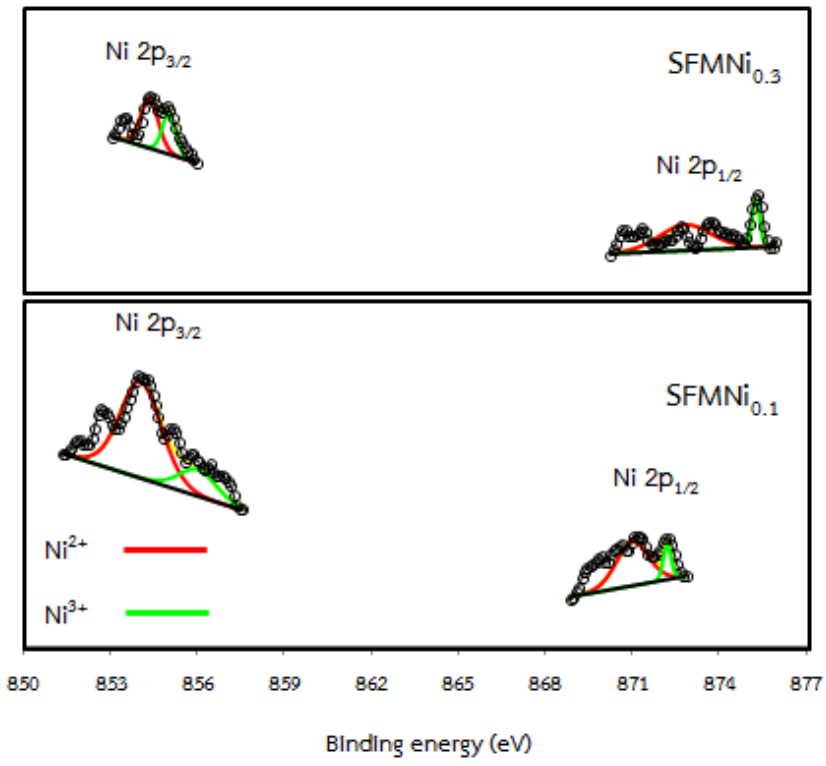

Figure 3.14 The Ni 2p core-level spectra of $SFMNi_{0.1}$ and $SFMNi_{0.3}$ double perovskite

For SFMO, $SFMNi_{0.1}$ and $SFMNi_{0.3}$, the XPS spectra of Ni 2p, Fe 2p, and Mo 3d are displayed in Figure 3.14-3.16. For Ni 2p study, all Ni-doped oxides showed the Ni^{2+} and Ni^{3+} species and the peaks appeared at binding energy of 854.4 eV and 856.5 eV corresponded to Ni^{2+} $2p_{3/2}$ and Ni^{3+} $2p_{3/2}$ whereas the binding energy of 871.4 eV and 872.4 eV are assigned to Ni^{2+} $2p_{1/2}$ and Ni^{3+} $2p_{1/2}$, respectively as shown in Figure 3.14.

Figure 3.15 shows the co-existence peaks of Fe $2p_{3/2}$ and Fe $2p_{1/2}$ at binding energy around 709.2 eV and 722.6 eV, respectively. Similar to the Fe-2p XPS spectra of $SFMCo_x$, there are three components observed at 705.3 eV (Fe^0 $3d_{5/2}$), 707.3 eV (Fe^{2+} $3d_{5/2}$) and 712.7 eV (Fe^{3+} $3d_{5/2}$) in SFMO, $SFMNi_{0.3}$ but in the case of the $SFMNi_{0.1}$, only the Fe^{2+} and Fe^{3+} valence states were found.

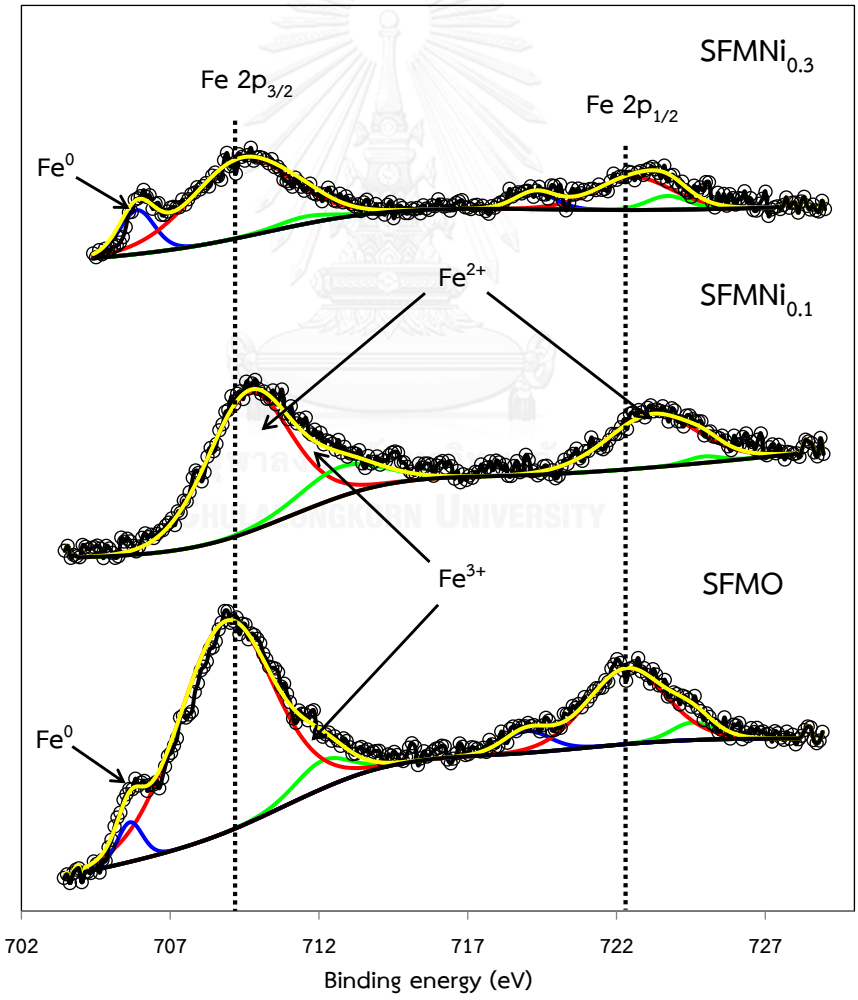

Figure 3.15 The Fe 2p core-level spectra of SFMO, $SFMNi_{0.1}$, $SFMNi_{0.3}$ double perovskite

Table 3.9 Chemical state of Fe 2p in $SFMNi_x$

Samples	Fe $2p_{3/2}$			Fe $2p_{1/2}$			Fe^{2+}/ Fe^{3+}
	Fe^0	Fe^{2+}	Fe^{3+}	Fe^0	Fe^{2+}	Fe^{3+}	ratio
SFMO	547	10977	839	558	3262	406	10.558
$SFMNi_{0.1}$	-	6356	1339	-	2636	119	13.451
$SFMNi_{0.3}$	835	4356	216	377	1396	310	12.335

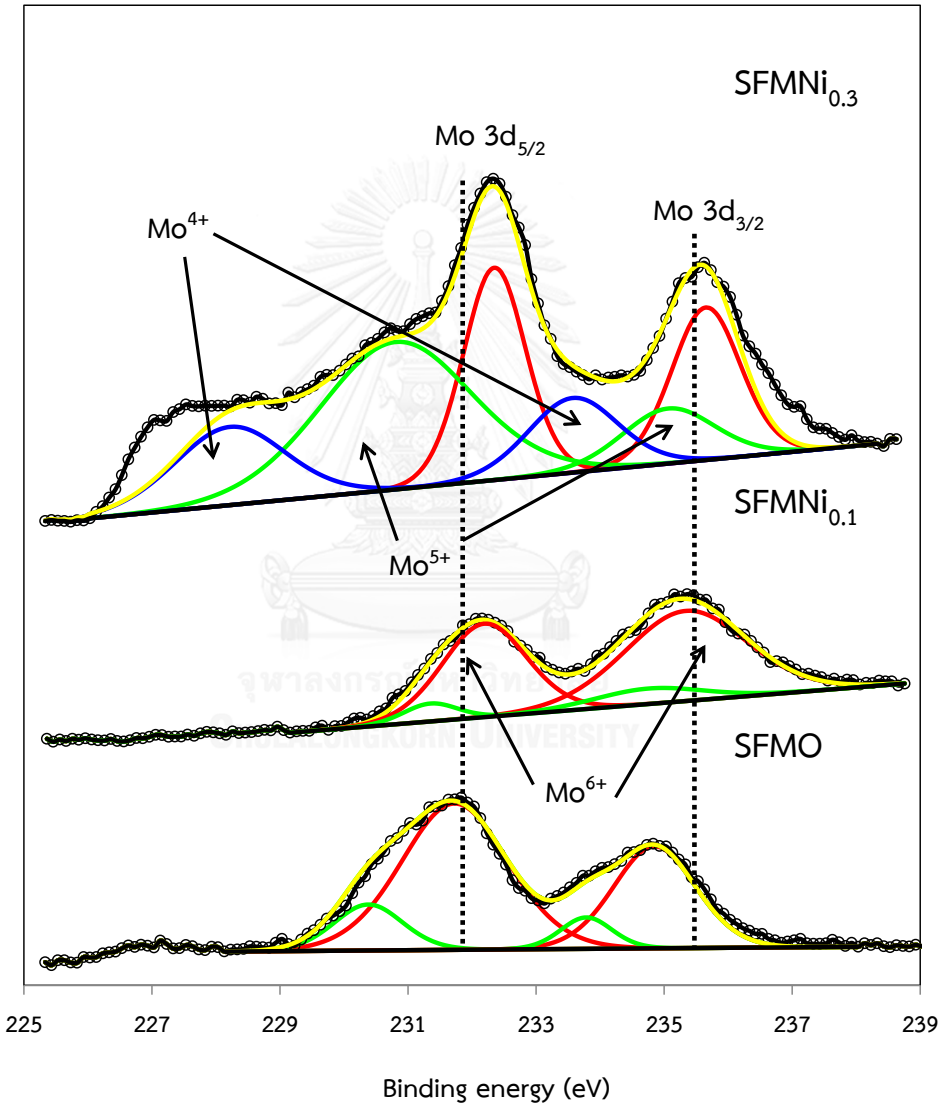

Figure 3.16 The Mo 3d core-level spectra of SFMO, $SFMNi_{0.1}$, $SFMNi_{0.3}$ double perovskite

Figure 3.16 demonstrates the Mo 3d XPS spectra of $SFMNi_x$. The two broad peaks around 231.9 eV and 235.0 eV are assigned to $3d_{5/2}$ and $3d_{1/2}$ on the binding energy scale. From the fitting curve extraction, the curves of Mo 3d are associated with Mo^{5+} (230.5 eV and 234.0 eV) and Mo^{6+} (232.2 eV and 235.5 eV) as observed in SFMO and $SFMNi_{0.1}$ oxides. However, in $SFMNi_{0.3}$, the binding energy of Mo $3d_{5/2}$ spectra at 228.1 eV, 230.8 and 232.5 eV are attributed to Mo^{4+} [37], Mo^{5+} and Mo^{6+}. The ratio of Mo^{6+}/ Mo^{5+} was calculated and the data are displayed in the same trend as the Fe^{2+}/ Fe^{3+} ions pair, as summarized in Table 3.9-3.10.

Table 3.10 Chemical state of Mo 3d in $SFMNi_x$

Samples	Mo $3d_{5/2}$			Mo $3d_{1/2}$			Mo^{6+}/ Mo^{5+}
	Mo^{4+}	Mo^{5+}	Mo^{6+}	Mo^{4+}	Mo^{5+}	Mo^{6+}	ratio
SFMO	-	788	3874	-	402	2089	5.056
$SFMNi_{0.1}$	-	242	1973	-	420	2755	7.356
$SFMNi_{0.3}$	7966	20499	12181	6150	4682	9654	1.328

From the XPS analysis of $SFMNi_x$, it is concluded that $SFMNi_x$ definitely established the appearance of Fe^{2+}/ Fe^{3+} and Mo^{6+}/ Mo^{5+} couples. The trace amount of Mo^{4+} occurred when high Ni content was added, e.g. at x = 0.3. In addition, the concentration of Ni can influence the proportion of mixed valence state couples. The ratio of Fe^{2+}/ Fe^{3+} and Mo^{6+}/ Mo^{5+} gives rising with the increase in the Ni content until it reached the highest proportion in $SFMNi_{0.1}$ anode. Thus, the high power density observed in the SOFC performance of this composition may be a result of reaction equilibrium of Fe^{3+} + Mo^{5+} = Fe^{2+} + Mo^{6+} that is a directly impact on the electrochemical properties of SFMO structure.

3.2 Characterization of $Sr_2Fe_{1-x}M_xMoO_6$ (M = Co, Ni; X = 0.0-0.2)

3.2.1 XRD characterizations

Figure 3.17 shows the XRD patterns of the SFMO, $SFCo_xM$ and $SFNi_xM$ oxide sintered at 1300°C for 12 hours in air. It is obviously seen that all materials consisted of two phases: the double-perovskite structure and the impurity phase, $SrMoO_4$, (JCPDS 08-0482). The main diffraction peak of metal-doped oxides at the two-theta of 32.2 slightly shifted to the lower value of two-theta compared to the SFMO structure, suggesting the expansion of crystal lattice caused by the substitution of Co and Ni in the structure. Because Co (0.65 Å) and Ni (0.69 Å) have larger ionic size than Fe (Fe^{2+} = 0.61 Å, Fe^{3+} = 0.55 Å), the lattice parameter should theoretically increase

with the introduction of Co and Ni. In case of $SrMoO_4$ impurity phase, a high intensity of the spectrum was still observed in the structure when increasing the dopant content. Thus, the remains of impurity phase in the structure when doping Co and Ni at Fe site is due to the Mo solubility limit as earlier explained.

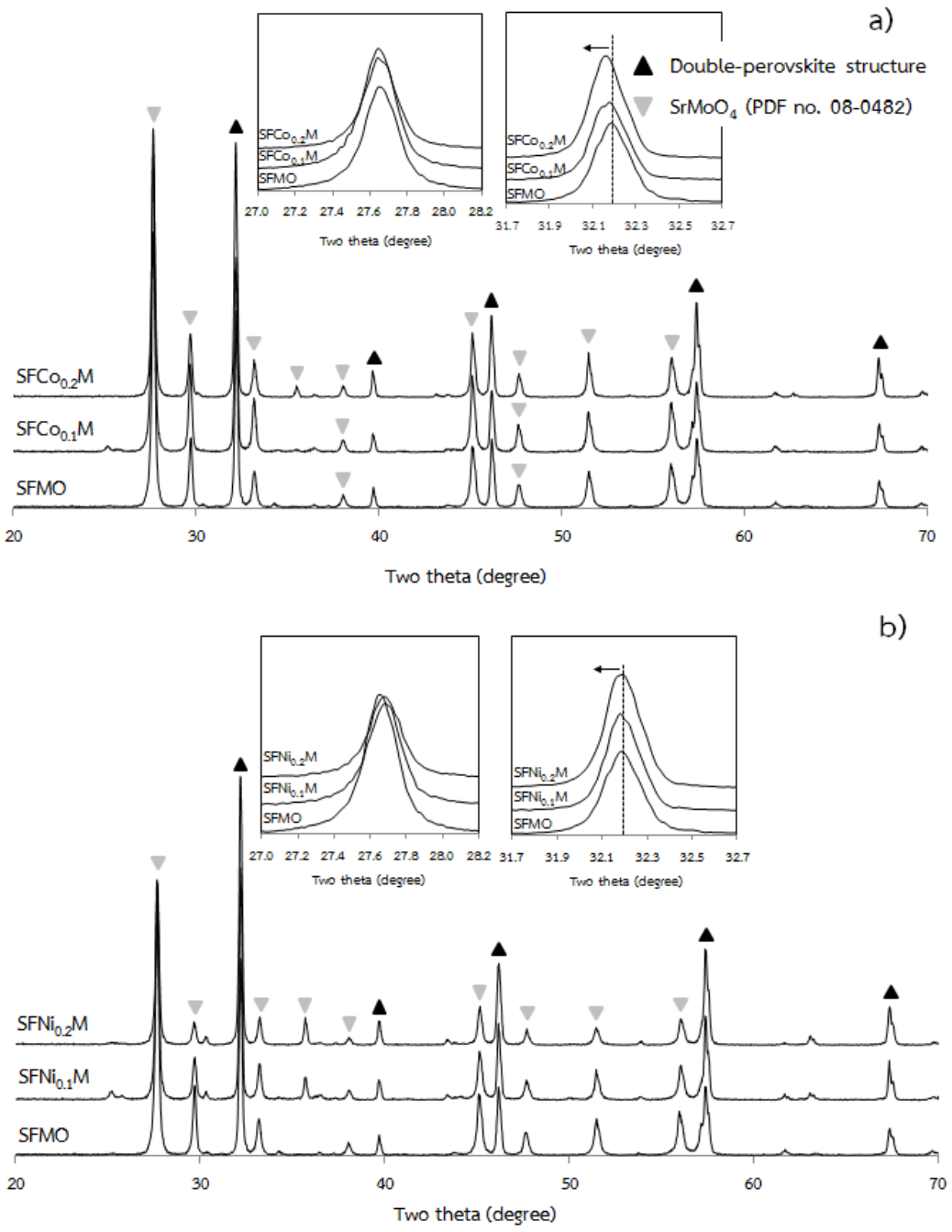

Figure 3.17 XRD patterns of a) $SFCo_xM$ and b) $SFNi_xM$ oxides sintered in air at 1300°C for 12 hours

3.2.2 Electrical conductivity measurement

Figure 3.18 shows the temperature dependence on electrical conductivity as a function of Co and Ni-doping concentrations in air from 300°C to 800°C and the data are summarized in Table 3.11-3.12.

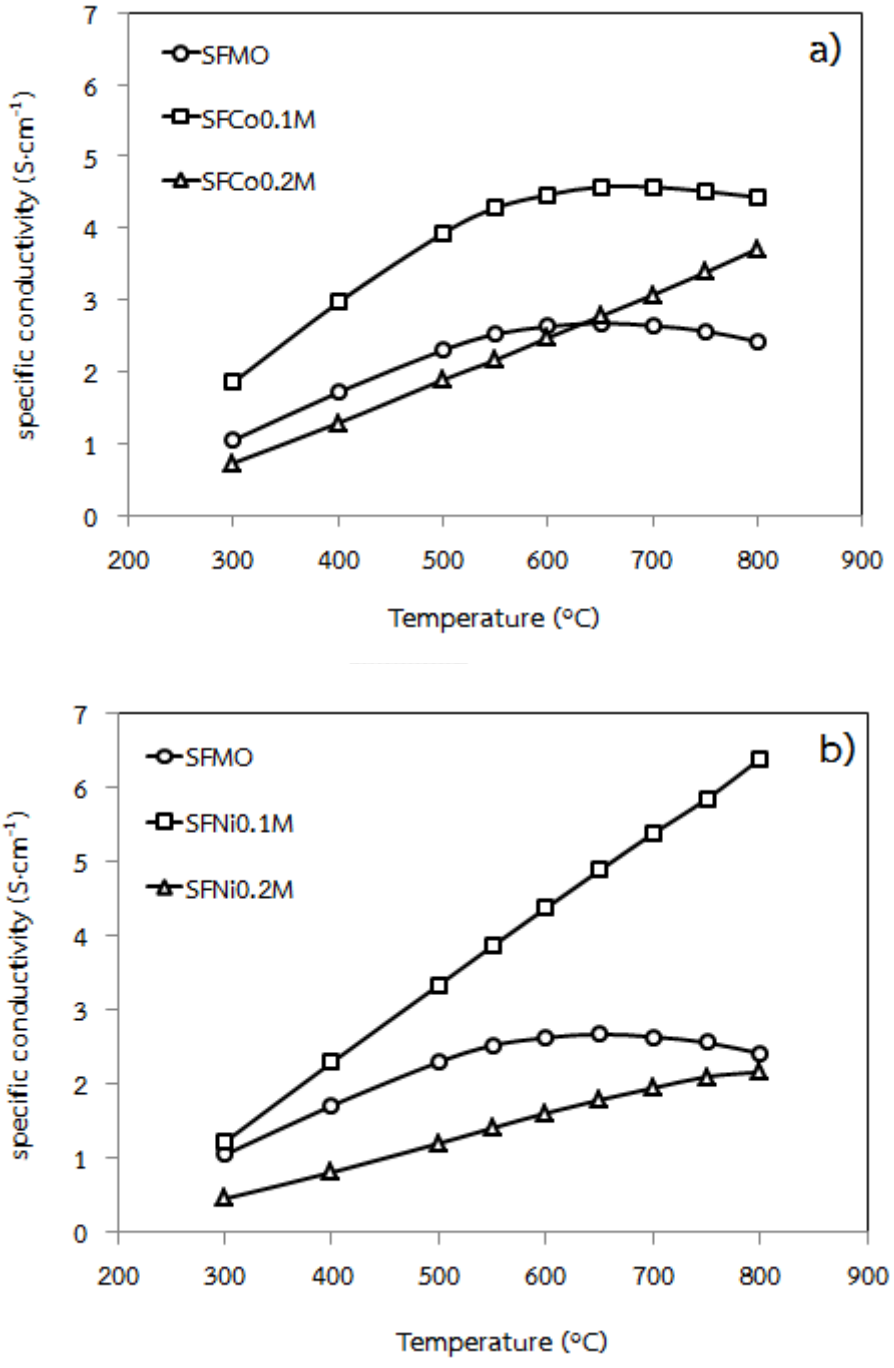

Figure 3.18 Temperature dependence on conductivity of (a) $SFCo_xM$ and (b) $SFNi_xM$ in air

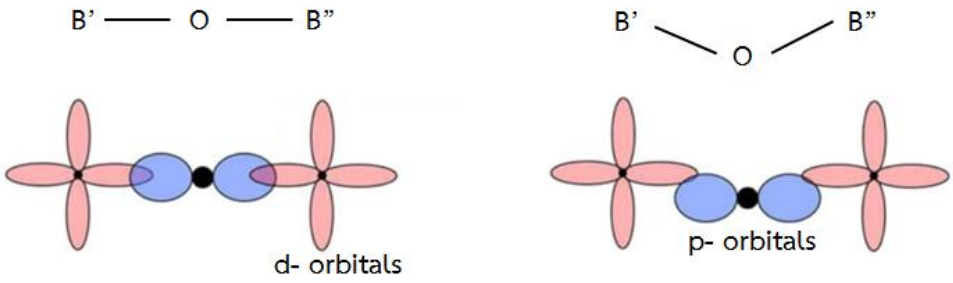

Figure 3.19 The orbitals overlapping of B'—O— B" [68]

The electrical conductivities of all examined oxides increased with increasing temperature, indicating the semiconducting behavior. In case of SFMO and $SFCo_{0.1}M$, the electrical conductivity increased to the temperature of 650°C and remained constant afterwards. The electrical conductivity did not continue increasing at high temperature, which could be a result from the loss of lattice oxygen contributing to the formation of oxygen vacancies and the reduction of electronic charge carrier concentration [52] as expressed in equation 3.5.

$$O_o^{\times} \longrightarrow \tfrac{1}{2}\, O_{2\,(g)} + V_o^{\bullet\bullet} + 2e^{-} \qquad (3.5)$$

Where $O_o^{\times}$ is the oxide ion on the oxide ion lattice site with neutral charge and $V_o^{\bullet\bullet}$ is the oxygen vacancies with double positive charge, based on Kröger–Vink notation.

Table 3.11 The specific conductivity of $SFCo_xM$ (x = 0-0.2)

Oxide	Specific conductivity ($S{\cdot}cm^{-1}$)							E_a (eV)
	300°C	400°C	500°C	600°C	700°C	800°C	max	
SFMO	1.05	1.71	2.30	2.63	2.64	2.42	2.68	0.379
$SFCo_{0.1}M$	1.85	2.97	3.93	4.46	4.57	4.43	4.57	0.133
$SFCo_{0.2}M$	0.73	1.29	1.89	2.48	3.07	3.71	3.71	0.230

With increasing concentration of dopant, the conductivity of $SFCo_xM$ increased and reached the maximum value when x = 0.1 around 4.58 $S{\cdot}cm^{-1}$ at 650°C, and became decreasing with more cobalt content (x = 0.2). Similar to the aspect of $SFCo_xM$ conduction, the conductivity of $SFNi_xM$ achieved 6.40 $S{\cdot}cm^{-1}$ at 800°C, followed by a decrease of electrical conductivity with more Ni-doping (x = 0.2). According to the density of state (DOS) calculation carried out by Xie [52], when

a trace amount of Co and Ni is added, the increasing of conductivity may be explained by two reasons: (i) the increasing of electrons at the Fermi level implies the increasing number of charge carrier concentration and (ii) the formation of smaller band gap can be approached from the valence band and conduction band. On the other hand, the decreasing of conductivity when x = 0.2 may be due to the bending strain caused by the larger ion doping into the lattice. The bending of the O—(Co, Fe)—O bonds reduces the bond angle below 180° as illustrated in Figure 3.19 [68].

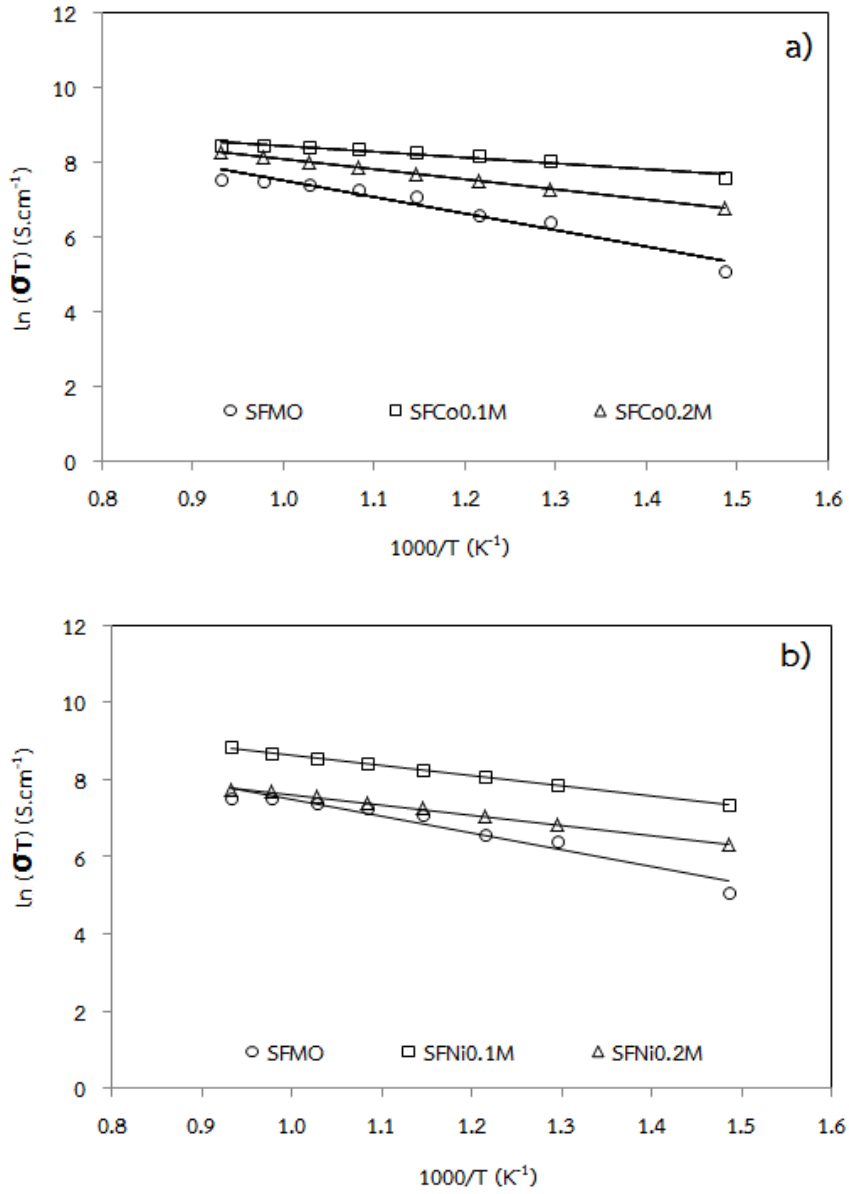

Figure 3.20 Arrhenius plots for the electrical conductivity of (a) $SFCo_xM$ and (b) $SFNi_xM$ at 300-800°C

Table 3.12 The specific conductivity of $SFNi_xM$ (x = 0-0.2)

Oxide	Specific conductivity ($S \cdot cm^{-1}$)							E_a (eV)
	300°C	400°C	500°C	600°C	700°C	800°C	max	
SFMO	1.05	1.71	2.30	2.63	2.64	2.42	2.68	0.379
$SFNi_{0.1}M$	1.22	2.30	3.34	4.38	5.38	6.40	6.40	0.228
$SFNi_{0.2}M$	0.46	0.82	1.20	1.61	1.95	2.16	2.16	0.230

The activation energy of all materials calculated from the slope of Arrhenius plot in Figure 3.20 is summarized in Table 3.11-3.12. The linear relationship between ln (σT) and 1000/T indicates the small polaron hopping mechanism of these materials [57]. With increasing the metal-doped content, E_a value decreases which can be explained by an easy jump of electron as a result of the two reasons mentioned by Xie [52] earlier. When x = 0.2, the E_a value increases but it is still lower than the un-doped one. In this study, the lowest E_a values of 0.133 eV and 0.228 eV were obtained from $SFCo_{0.1}M$ and $SFNi_{0.1}M$, respectively, which corresponds to the highest conductivity of the Co, Ni-doped oxides.

Comparing the conductivity between Co- and Ni-doped SFMO oxides, $SFM(Co, Ni)_x$ oxides, $SF(Co, Ni)_xM$ anodes have the lower conductivity than that of $SFM(Co, Ni)_x$ family. This is because the substitution at the different site may promote the different carrier as the key of electrochemical properties. And, for this reason the $SF(Co, Ni)_xM$ anodes were not further investigated on other compositions.

3.2.3 Single cell performance

Figure 3.19 shows the power density and cell voltage as a function of current density at 800°C for a single cell with the prepared-oxide anodes. The power density of $SFCo_xM$ and $SFNi_xM$ increased with the dopant content as x = 0.1 and decreased when x = 0.2. The highest power density collected from the cell with $SFCo_{0.1}M$ and $SFNi_{0.1}M$ anode were 823 and 834 $mW \cdot cm^{-2}$, which are actually higher than the cell using SFMO anode.

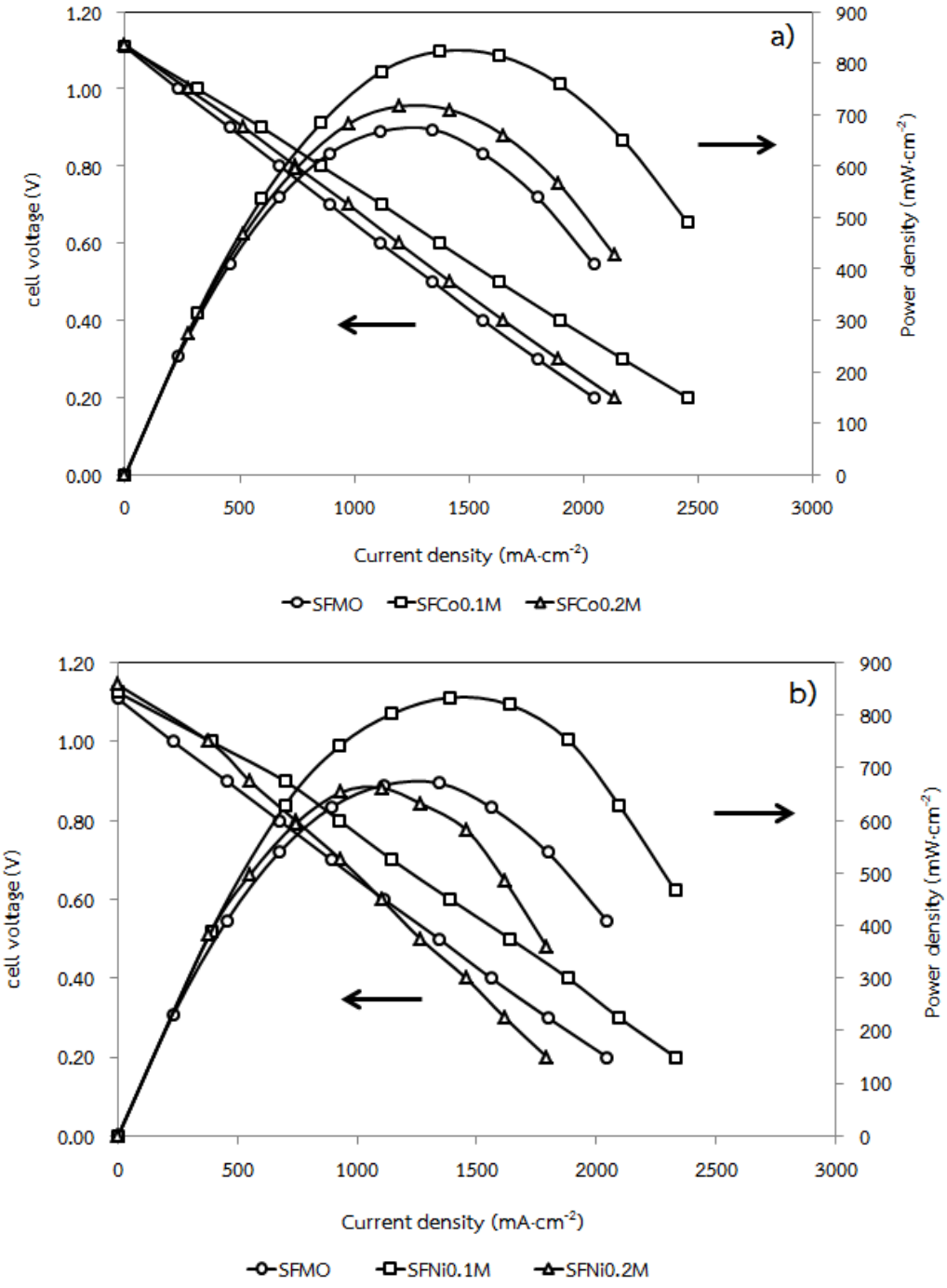

Figure 3.21 The single cell performance of cells a) $SFCo_xM$ / LSGM / SSC and b) $SFNi_xM$ / LSGM/ SSC at 800°C

Table 3.13 The power density and the polarization resistance of LSGM-supported single cell with different anode materials at 800ºC

Anodes	R_p ($\Omega \cdot cm^2$)	Power density ($mW \cdot cm^{-2}$)
SFMO	0.59	671
$SFCo_{0.1}M$	0.46	823
$SFCo_{0.2}M$	0.56	716
$SFNi_{0.1}M$	0.45	834
$SFNi_{0.2}M$	0.80	661

Therefore, it has been concluded that by doping small amount of Co and Ni at Fe site of SFMO, the cell performance of SFMO was improved. In addition, the increasing trend of power density is similar to the increase in the conductivity of materials suggesting electronic conduction play an important role in conductivity and cell performance.

3.2.4 Electrochemical impedance

In addition, the corresponding impedance data are shown in Figure 3.20 and Table 3.11. It can be seen that the R_p value continuously decreased with increasing metal doping from x = 0 to x = 0.1 and then increased with the dopant addition. These results are in agreement with the power density of the cell. The higher the power density, the lower the polarization resistance obtained. The minimum R_p of $SFCo_xO$ and $SFNi_xO$ oxides are 0.46 and 0.45 $\Omega \cdot cm^2$, obtained from $SFCo_{0.1}M$ and $SFNi_{0.1}M$, respectively.

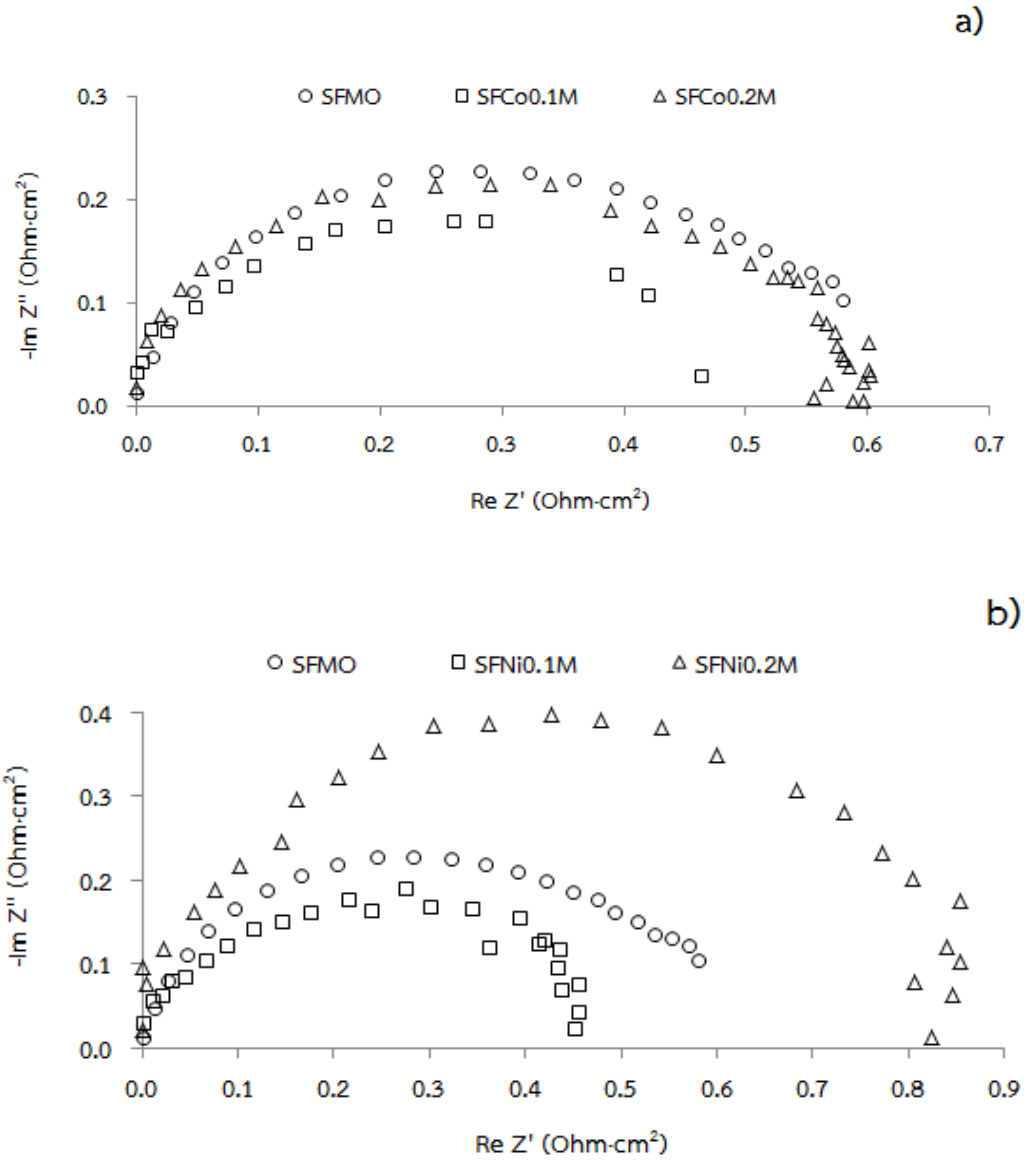

Figure 3.22 Relative impedance spectra of cells at 800°C a) $SFCo_xM$/ LSGM/ SSC and b) $SFNi_xM$/ LSGM/ SSC

3.2.5 Cross section analysis

Figure 3.23 shows the cross-section SEM images of $SFCo_{0.1}M$ and $SFNi_{0.1}M$ as anodes after cell testing. A good binding and continuous contact between anodes and LSGM electrolytes were observed which is indicative of the good thermal-expansion compatibility along anode and electrolyte; as a result, the high SOFC performance was obtained.

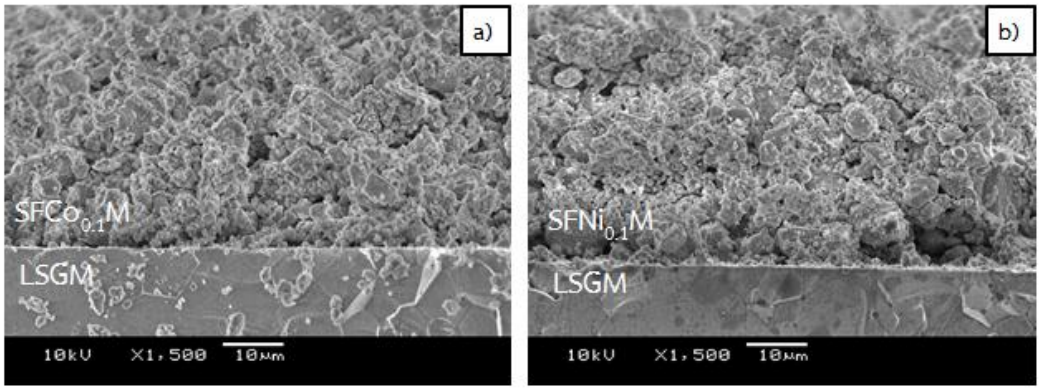

Figure 3.23 Cross-section images of anode on LSGM electrolyte after cell performance testing a) $SFCo_{0.1}M$ and b) $SFNi_{0.1}M$

3.3 Characterization of $Sr_{2-x}A_xFeMo_{0.5}Co_{0.5}O_6$ (A = La, Pr; X = 0.0-0.3)

$SFMCo_x$ and $SFMNi_x$ with the highest electrical conductivity were chosen for the substitution of La and Pr in Sr-site to improve the electrical conductivity in this experiment.

3.3.1 XRD characterizations

The XRD patterns of La_x-$SFMCo_{0.5}$ and Pr_x-$SFMCo_{0.5}$ are shown in Figure 3.24. The phase of $SFMCo_{0.5}$ was determined as double perovskite structure. When lanthanum was introduced into the Sr-site of $SFMCo_{0.5}$, the double perovskite structure was obtained as a major phase and the main diffraction peaks of La_x-$SFMCo_{0.5}$ at two-theta degree of 32.3 slightly shifted to the higher values, suggesting the contraction of lattice parameter. The substitution of small cation La^{3+} to the Sr site (La^{3+} = 1.36 Å, Sr^{2+} = 1.45 Å) causes the shrinkage of crystal lattice. However, the secondary phase, CoO (JCPDS 78-0431) was observed as a trace impurity in the composition, indicating the limitation of lanthanum introduced into the structure. Moreover, the $SrMoO_4$ phase impurity was also obtained from $La_{0.3}$-$SFMCo_{0.5}$ composition as a common impurity in SFMO structure [50]. In case of the replacement of Sr by praseodymium, the XRD patterns of Pr_x-$SFMCo_{0.5}$ provided a similar result with La_x-$SFMCo_{0.5}$. The double perovskite structure was still obtained as the major phase whereas the formation of CoO impurity in sample with x = 0.1 and the existence of $SrMoO_4$ in sample with x = 0.3 were noticed. As reported by Taskin [69], in the double perovskite structure, the difference in size between the host ion and the substituted ion at the A-site is very sensitive to the atomic arrangement in the AO plane which can be resulted in the reduction of the strength of oxygen

binding. Thus, when Pr (Pr^{3+} = 1.13 Å) was added at Sr (Sr^{2+} = 1.45 Å), the intensity of the main diffraction peak of double-perovskite structure decline, indicating a low crystallinity in the structure due to structural distortion. With more addition of La and Pr, the instability of the structure caused by the weaker of oxygen bonding in the SrO planes may result in the removal of Sr from the lattice to form $SrMoO_4$ phase as seen from the addition as x = 0.3. In addition, Pr has smaller ionic radii than La, the distortion of structure would be high and the crystallinity of Pr-substituted materials is reduced, which is clearly observed by the XRD results.

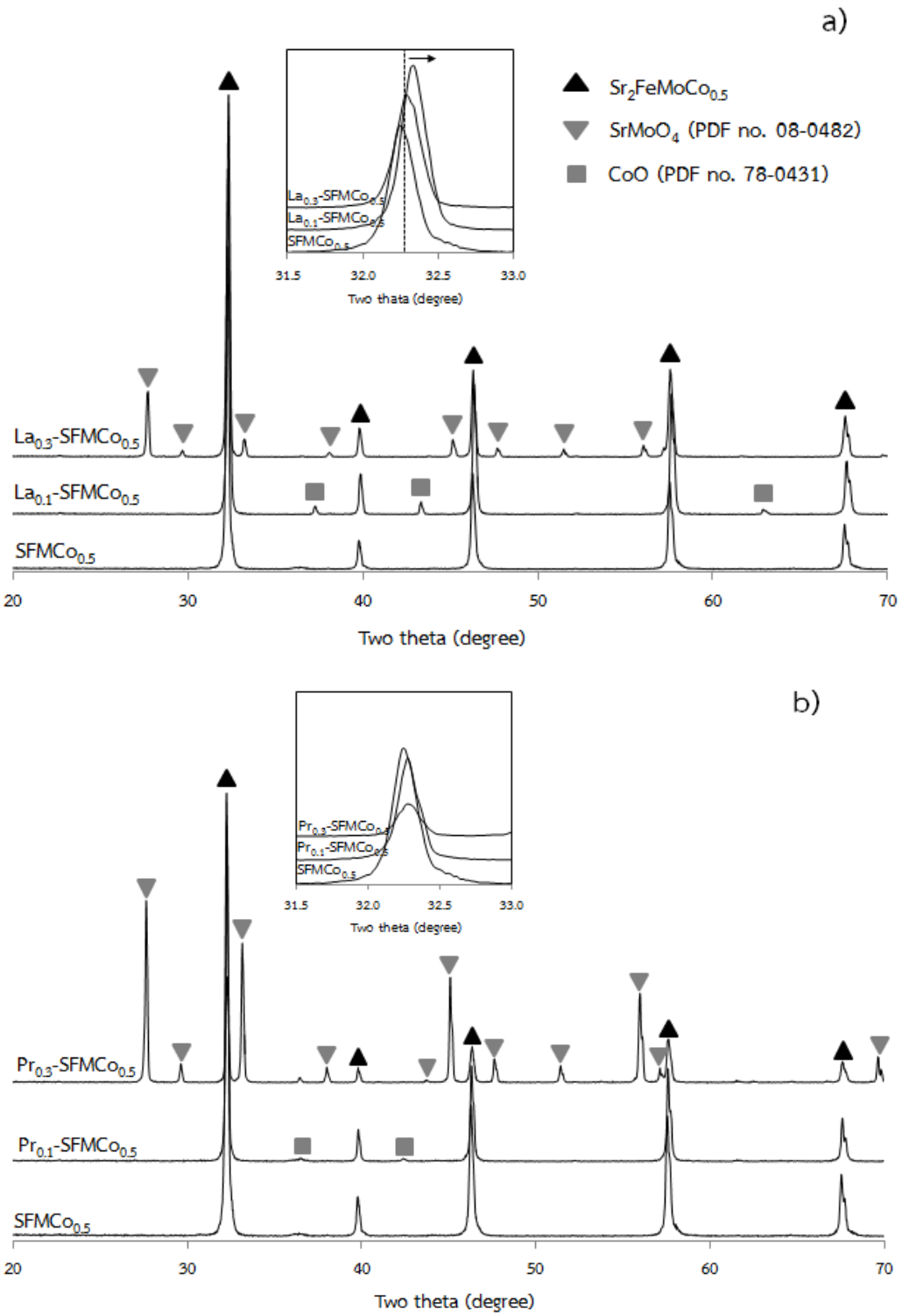

Figure 3.24 XRD patterns of a) La_x-$SFMCo_{0.5}$ and b) Pr_x-$SFMCo_{0.5}$ oxides sintered in air at 1300°C for 12 hours in air

3.3.2 Electrical conductivity measurement

Figure 3.25 shows the temperature dependence on electrical conductivity as a function of La and Pr-doping concentrations in air from 300°C to 800°C and the data are summarized in Table 3.14.

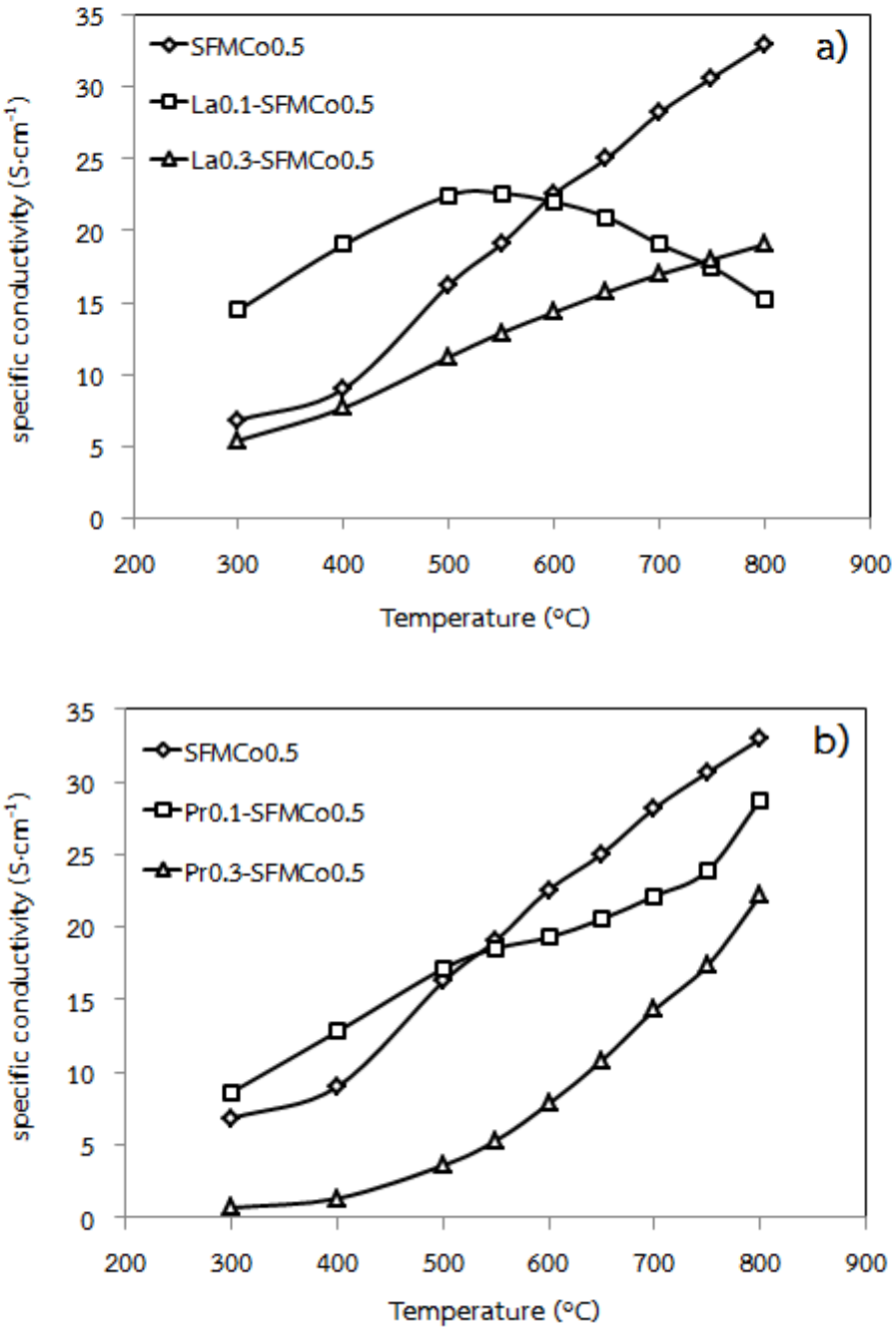

Figure 3.25 Temperature dependence on conductivity of (a) La_x-$SFMCo_{0.5}$ and (b) Pr_x-$SFMCo_{0.5}$ in air

Table 3.14 The specific conductivity of La_x-$SFMCo_{0.5}$ and Pr_x-$SFMCo_{0.5}$ (x = 0-0.3)

Oxide	Specific conductivity ($S \cdot cm^{-1}$)							E_a (eV)
	300°C	400°C	500°C	600°C	700°C	800°C	max	
$SFMCo_{0.5}$	6.85	9.03	16.25	22.56	28.18	32.93	32.93	0.244
$La_{0.1}$-$SFMCo_{0.5}$	14.50	19.03	22.46	22.03	19.08	15.21	22.46	0.077
$La_{0.3}$-$SFMCo_{0.5}$	5.44	7.70	11.24	14.35	16.96	19.04	19.04	0.204
$Pr_{0.1}$-$SFMCo_{0.5}$	8.64	12.82	17.13	19.28	22.15	28.76	28.76	0.182
$Pr_{0.3}$-$SFMCo_{0.5}$	0.69	1.33	3.61	7.85	14.32	22.19	22.19	0.451

As observed in Figure 3.25, the electrical conductivity of $SFMCo_{0.5}$ was indicative of semiconducting behavior throughout the range of temperature measurement. When La was introduced into the Sr site, the electrical conductivity of $La_{0.1}$-$SFMCo_{0.5}$ showed metallic-like conduction behavior after 500°C. The variation of conduction behavior of this material may be explained by the formation of CoO phase observed from XRD because it is a conducting material. In case of $La_{0.3}$-$SFMCo_{0.5}$, semiconducting-like conduction behavior was observed and the $SrMoO_4$ impurity phase was not considered because it is an insulating material and no evidence of CoO was formed. For Pr_x-$SFMCo_{0.5}$ oxides, the electrical conductivity of all samples exhibited the conduction behavior as semiconductor similar to the base material. However, the decreased in electrical conductivity by the addition of La and Pr may be described by a weaker bond of oxygen and the distortion of structure, which retards the migration of electrons. Thus, it can be concluded that the addition of Pr and La at A-site does not improve the properties of $SFMCo_{0.5}$ material.

The activation energy of La_x-$SFMCo_{0.5}$ and Pr_x-$SFMCo_{0.5}$ calculated from the slope of Arrhenius plot (Figure 3.26) is summarized in Table 3.14. It can be seen that the E_a values decreased with the dopant. This may be explained by many plausible reasons: (i) the different type of conduction behavior, (ii) some electrons are blocked by oxygen vacancy, and (iii) CoO impurity enhances the movement of electrons. However, when the dopant was increased, the E_a values increased, indicating a poor migration of electron which may cause by the structural distortion.

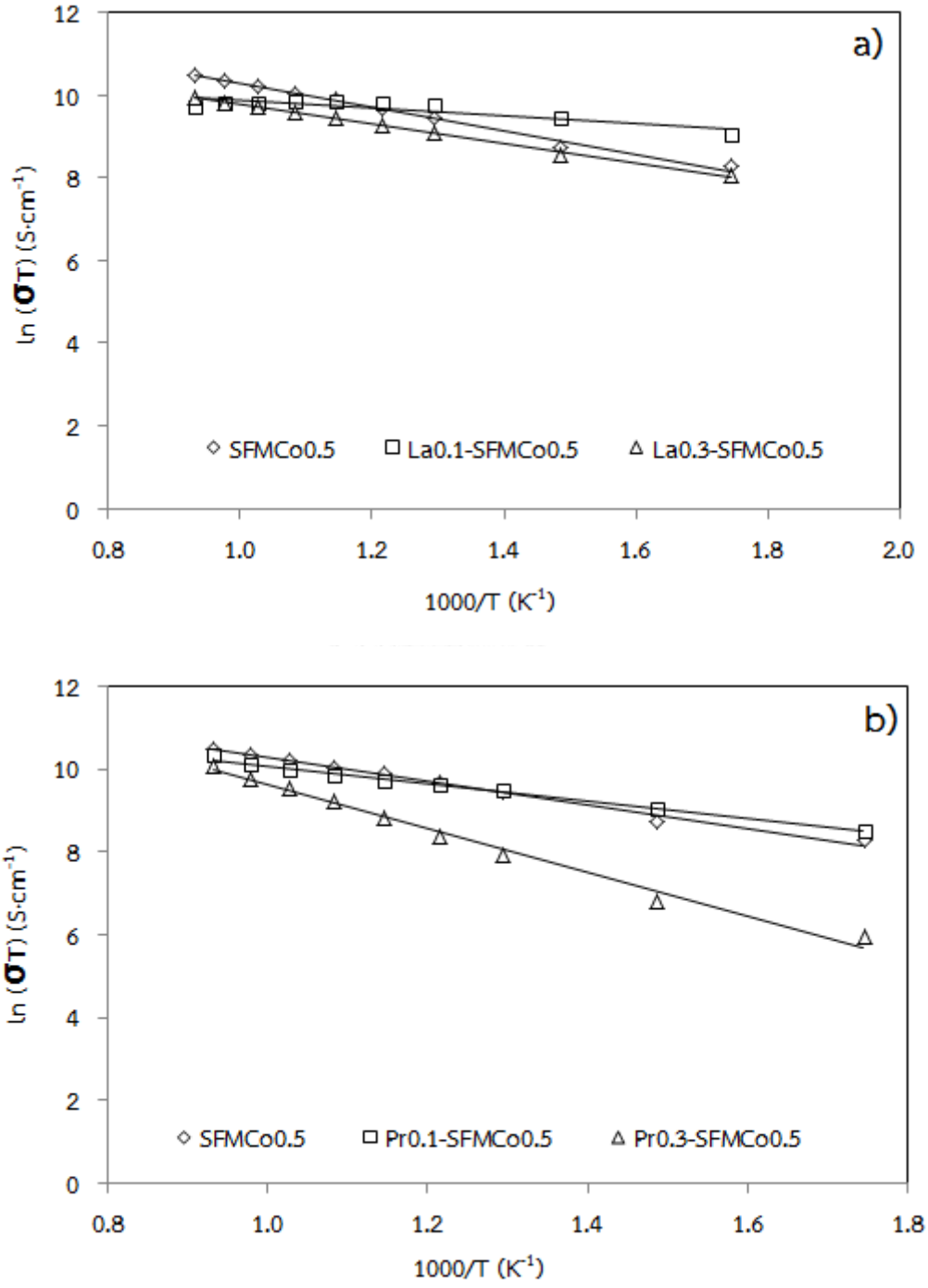

Figure 3.26 Arrhenius plots for the electrical conductivity of (a) La_x-$SFMCo_{0.5}$ and (b) Pr_x-$SFMCo_{0.5}$ at 300-800°C

3.4 Characterization of $Sr_{2-x}A_xFeMo_{0.5}Ni_{0.5}O_6$ (A = La, Pr; X = 0.0-0.3)

3.4.1 XRD characterizations

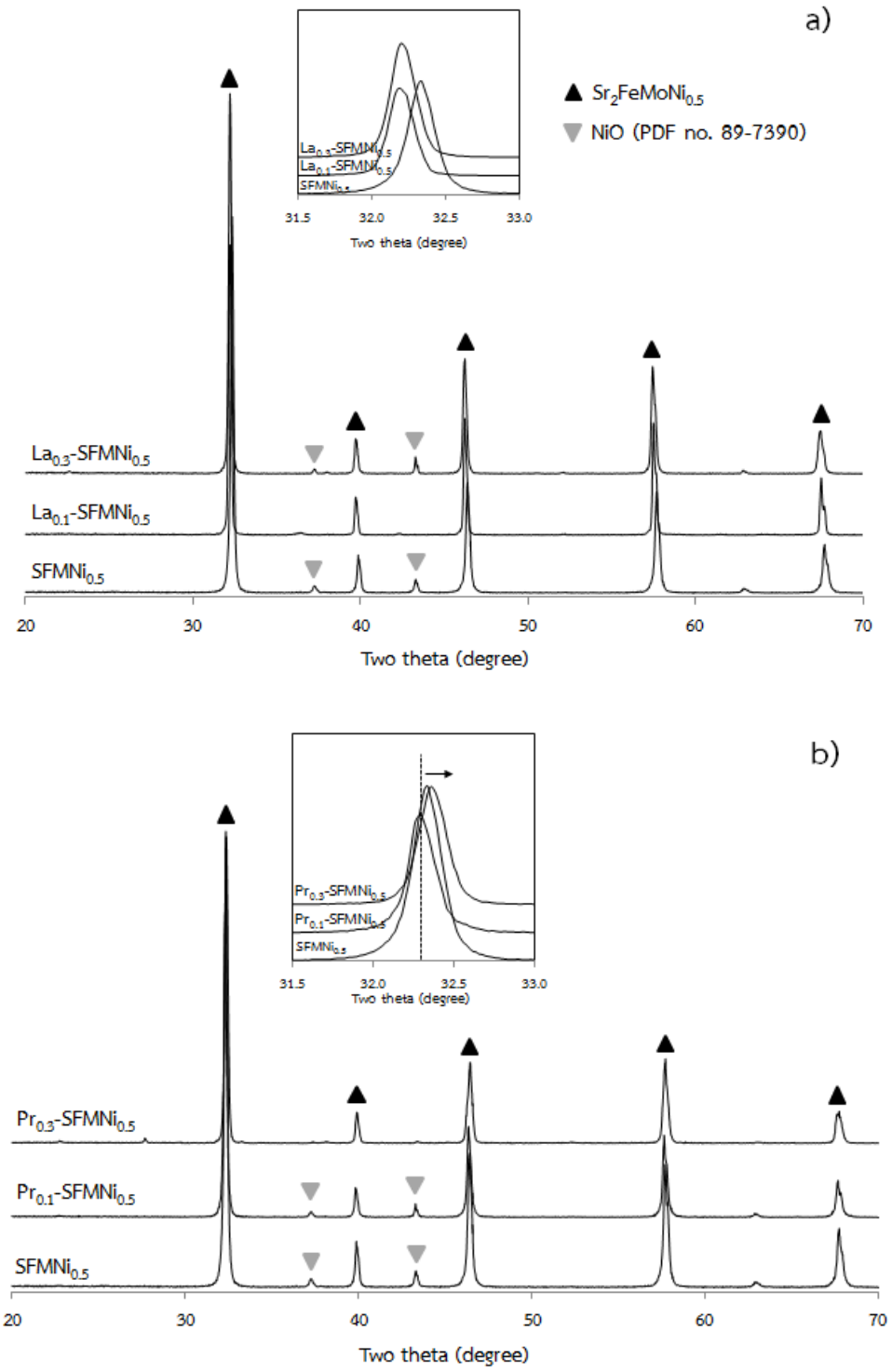

Figure 3.27 XRD patterns of a) La_x-$SFMNi_{0.5}$ and b) Pr_x-$SFMNi_{0.5}$ oxides sintered in air at 1300°C for 12 hours

The XRD patterns of La_x-$SFMNi_{0.5}$ and Pr_x-$SFMNi_{0.5}$ (x = 0-0.3), Figure 3.28, show that the structures of all compounds are double perovskite phase with a trace amount of NiO (JCPDS 89-7390) impurity phase. With increasing of x value, the main diffraction peaks of La_x-$SFMNi_{0.5}$ slightly shifted to the lower values, indicating the structural expansion caused by the loss of the excess Ni in the structure to form NiO as impurity phase. On the contrary, the main diffraction peaks of Pr_x-$SFMNi_{0.5}$ slightly shifted to the higher degree of two-theta, suggesting the decrease in lattice parameter caused by the doping of smaller size cation into the structure.

3.4.2 Electrical conductivity measurement

Figure 3.28 shows the temperature dependence on electrical conductivity as a function of La and Pr-doping concentrations in air from 300°C to 800°C and the data are summarized in Table 3.15.

Table 3.15 The specific conductivity of La_x-$SFMNi_{0.5}$ and Pr_x-$SFMNi_{0.5}$ (x = 0-0.3)

Oxide	Specific conductivity ($S \cdot cm^{-1}$)							E_a (eV)
	300°C	400°C	500°C	600°C	700°C	800°C	max	
$SFMNi_{0.5}$	22.06	34.90	45.77	50.11	46.27	43.02	50.11	0.136
$La_{0.1}$-$SFMNi_{0.5}$	8.68	13.59	18.19	21.00	24.22	27.67	27.67	0.186
$La_{0.3}$-$SFMNi_{0.5}$	10.27	14.97	18.64	20.65	16.74	16.26	20.65	0.111
$Pr_{0.1}$-$SFMNi_{0.5}$	9.51	13.89	18.10	16.66	14.82	12.99	18.10	0.098
$Pr_{0.3}$-$SFMNi_{0.5}$	4.28	6.43	8.55	9.73	10.01	9.39	10.01	0.154

The result showed that $SFMNi_{0.5}$ has semiconducting behavior at T < 600°C and shows a metallic-like behavior at T > 600°C. For La_x-$SFMNi_{0.5}$, with increasing of dopant, the conductivity decreased and the conduction behavior was changed. $La_{0.1}$-$SFMNi_{0.5}$ exhibited the semiconductor behavior whereas $La_{0.3}$-$SFMNi_{0.5}$ showed similar behavior as $SFMNi_{0.5}$. In case of Pr_x-$SFMNi_{0.5}$, the conductivity also decreased with increasing of x and the conducting behavior also varied as in La-substitution. The decrease of conductivity in La, Pr-doped perovskites may be a result of the BO_6-octahedral tilting caused by a decrease of the A site radius. This movement made a non-perfect overlapping of orbitals and reduced the moving of electrons.

The activation energy of La_x-$SFMNi_{0.5}$ and Pr_x-$SFMNi_{0.5}$ was calculated from the slope of Arrhenius plot (Figure 3.29) as summarized in Table 3.15. When La and Pr

were introduced into $SFMNi_{0.5}$, it was observed that the materials containing the NiO impurity phase have lower E_a values than that of the non-contaminated oxides, which may be due to the property of NiO phases as a semiconducting material. Therefore, the conduction property of $SFMNi_{0.5}$ is not improved by the insertion of La and Pr at Sr site.

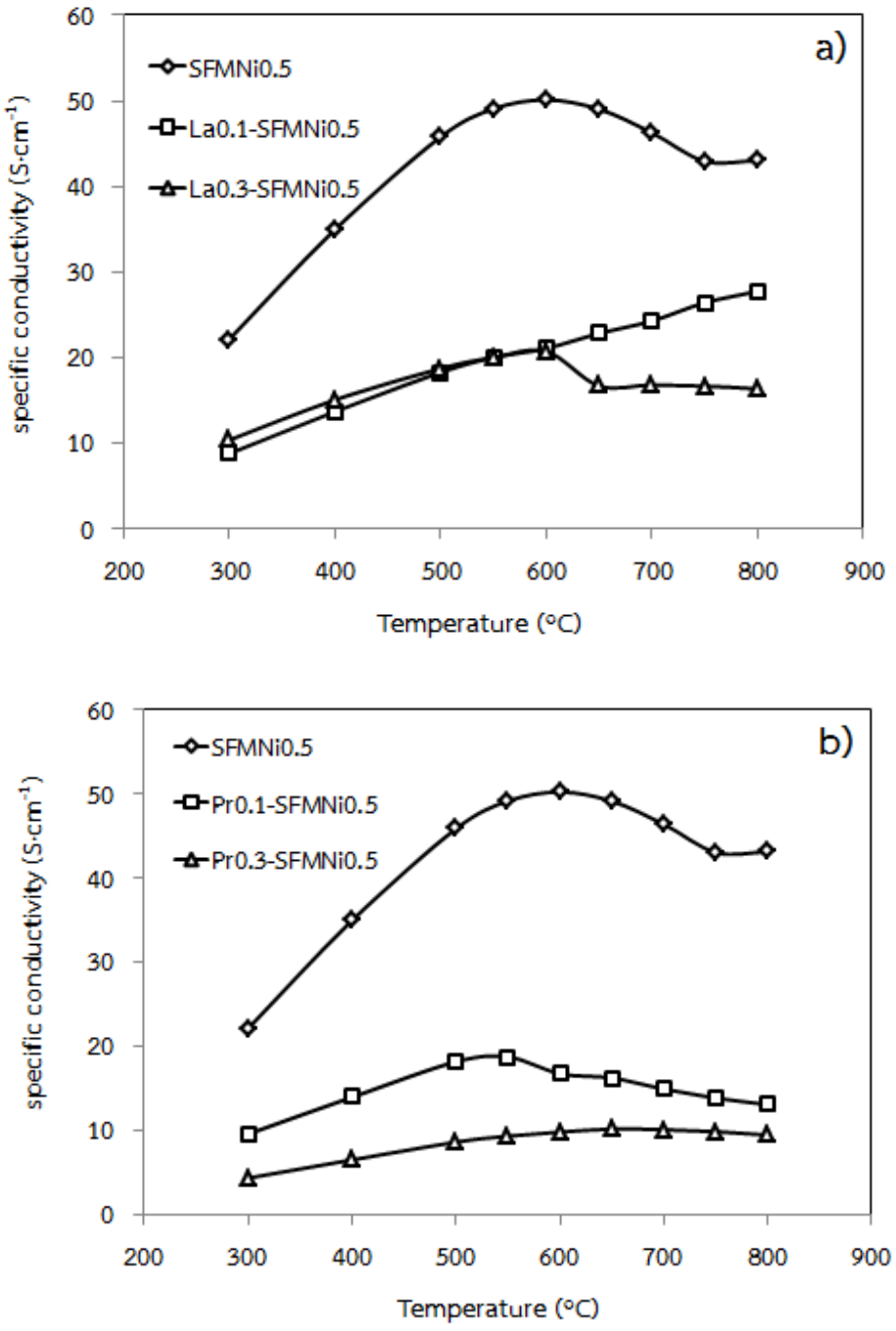

Figure 3.28 Temperature dependence on conductivity of (a) La_x-$SFMNi_{0.5}$ and (b) Pr_x-$SFMNi_{0.5}$ in air

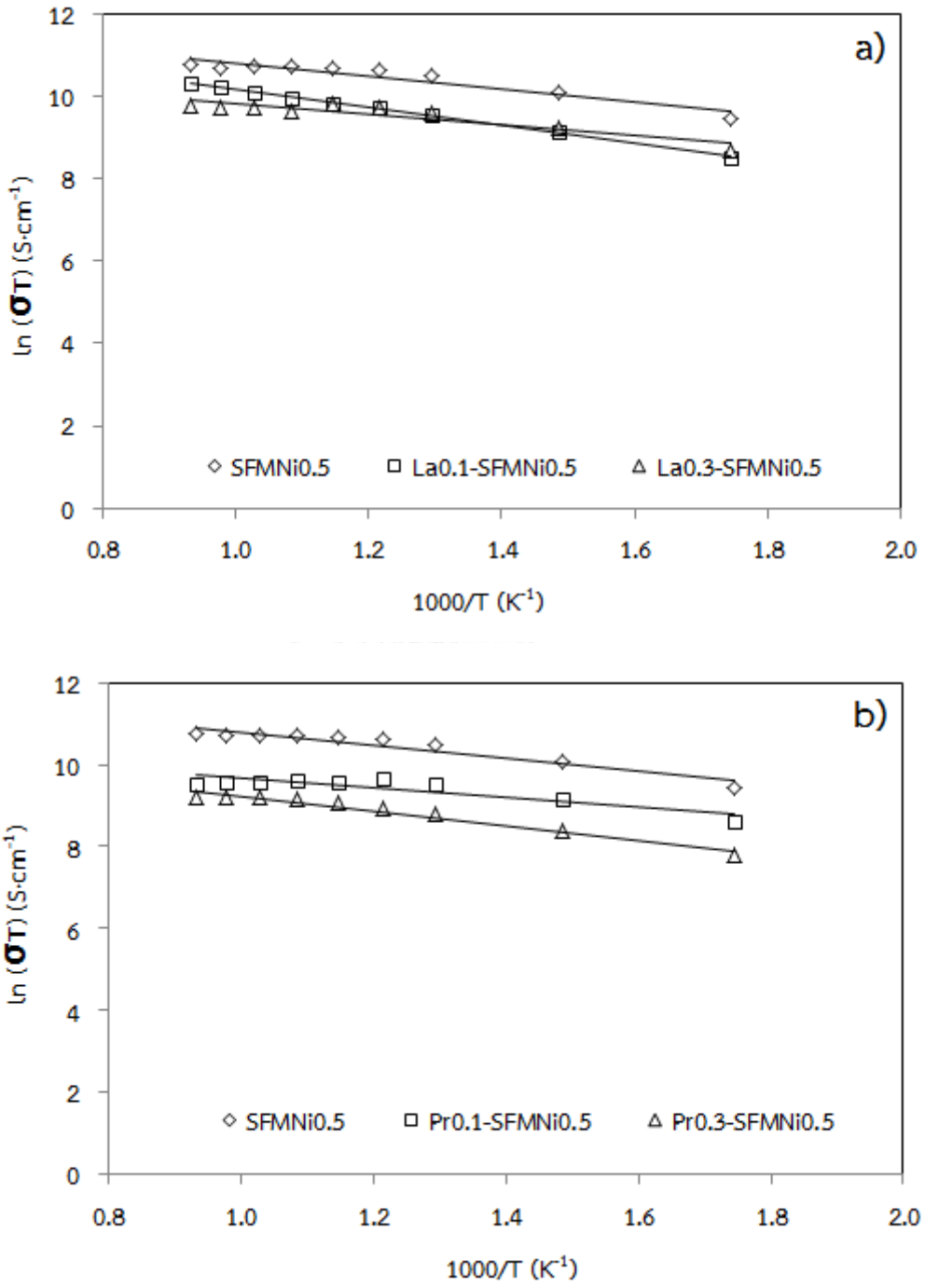

Figure 3.29 Arrhenius plots for the electrical conductivity of (a) La_x-$SFMNi_{0.5}$ and (b) Pr_x-$SFMNi_{0.5}$ at 300-800°C

CHAPTER IV
CONCLUSION

4.1 Conclusion

The following materials: (a) Sr_2FeMoO_6 (SFMO) (b) $Sr_2FeMo_{1-x}Co_xO_6$ ($SFMCo_x$, x = 0.0-0.5) and $Sr_2FeMo_{1-x}Ni_xO_6$ ($SFMNi_x$, x = 0.0-0.5) (c) $Sr_2Fe_{1-x}Co_xMoO_6$ ($SFCo_xM$, x = 0.0-0.2) and $Sr_2Fe_{1-x}Ni_xMoO_6$ ($SFNi_xM$, x = 0.0-0.2) (d) $Sr_{2-x}La_xFeMo_{0.5}Co_{0.5}O_6$ (La_x-$SFMCo_{0.5}$, x = 0.0-0.3) and $Sr_{2-x}Pr_xFeMo_{0.5}Co_{0.5}O_6$ (Pr_x-$SFMCo_{0.5}$, x = 0.0-0.3) (e) $Sr_{2-x}La_xFeMo_{0.5}Ni_{0.5}O_6$ (La_x-$SFMNi_{0.5}$, x = 0.0-0.3) and $Sr_{2-x}Pr_xFeMo_{0.5}Ni_{0.5}O_6$ (Pr_x-$SFMNi_{0.5}$, x = 0.0-0.3) were synthesized by a conventional solid state method under calcination temperature of 1000°C and sintering temperature of 1300°C for 12 hours. These oxides were characterized for phase structure, thermal expansion property, oxygen permeation, cross-section morphology and electrochemical property.

SFMO structure contains two phases: double perovskite and $SrMoO_4$ impurity (JCPDS 08-0482). The amount of $SrMoO_4$ impurity phase in $SFMCo_x$ and $SFMNi_x$ structures decreased with increasing of dopant and the pure double perovskite phase was obtained for x = 0.5 due to the solubility limit of Mo. All prepared materials exhibited semiconducting-like behavior and the electrical conductivity increased with Co-, Ni- addition due to a good overlapping of orbitals that can enhance the electron delocalization. The maximum conductivity values of 32.93 and 50.11 $S{\cdot}cm^{-1}$ were obtained from $SFMCo_{0.5}$ and $SFMNi_{0.5}$, respectively at 800°C. The highest power density of 802 $mW{\cdot}cm^{-2}$ and 723 $mW{\cdot}cm^{-2}$ at 800°C were observed from the cells using $SFMCo_{0.2}$ and $SFMNi_{0.1}$ anode, respectively, because of their high oxygen mobility and well-connected with LSGM electrolyte.

For the introduction of Co and Ni into the Fe-site, $SFCo_xM$ and $SFNi_xM$, these oxides consisted of the double perovskite structure and the $SrMoO_4$ impurity phase. Because of the solubility limit of Mo, the $SrMoO_4$ phase was still observed when increasing of Co and Ni content. Additionally, the electrical conductivity was improved by Co and Ni doping in the structure. This may be due to the increase in electronic charge carrier quantity and regarding to the band structure, the Fermi level and the valence band became closer. The highest electrical conductivity was achieved on $SFCo_{0.1}M$ and $SFNi_{0.1}M$ as 823 and 834 $mW{\cdot}cm^{-2}$, respectively, which can be supported by the minimal polarization resistance and the good connection to the LSGM electrolyte.

When substituted La and Pr at Sr-site in $SFMCo_{0.5}$ and $SFMNi_{0.5}$, La_x-$SFMCo_{0.5}$, Pr_x-$SFMCo_{0.5}$, La_x-$SFMNi_{0.5}$ and Pr_x-$SFMNi_{0.5}$ were obtained as a major product whereas

CoO and $SrMoO_4$ phase were noticed as impurity phase in doped-$SFMCo_{0.5}$ materials. This is because a large difference in size of the occupied ion at the A-site makes the oxygen strength weaker binding. The electrical conductivity of the doped oxides decreased when increased the concentration of dopant. These may be because the structural instability resulted from the weaker bond of oxygen in AO planes prohibit the hopping path of electrons or holes through the AO bonding. For doped-$SFMNi_{0.5}$ materials, most samples contained a trace amount of NiO impurity phase. The decreased in electrical conductivity with increasing of dopant content may be explained by the distortion of BO_6 octahedra in the structure. Based on these investigations, it can be concluded that insertion of Co and Ni at Mo-site and Fe-site can improve the electrochemical properties including the electrical conductivity, the oxygen permeation and the SOFC performance of SFMO materials. By a small addition of Co and Ni, $SFMCo_{0.2}$ and $SFMNi_{0.1}$ are potential anodes in SOFC. On the contrary, La and Pr substitution at A-site does not improve the property of materials.

4.2 Suggestions

1) $SFCo_xM$ and $SFNi_xM$ oxides should be characterized by XPS, dilatometer and oxygen permeation in order to obtain more details about oxidation state, compatibility with the adjacent components, and oxygen vacancy of the material.

2) The stability of single cell and the variation of fuel such as CH_4 should be performed for CH_4 reduction.

REFERENCES

[1] Boudghene Stambouli, A. and Traversa, E. Fuel cells, an alternative to standard sources of energy. Renewable and Sustainable Energy Reviews 6(3) (2002): 295-304.

[2] Acres, G.J.K. Recent advances in fuel cell technology and its applications. Journal of Power Sources 100(1–2) (2001): 60-66.

[3] Stambouli, A.B. and Traversa, E. Solid oxide fuel cells (SOFCs): a review of an environmentally clean and efficient source of energy. Renewable and Sustainable Energy Reviews 6(5) (2002): 433-455.

[4] Karakoussis, V., Brandon, N.P., Leach, M., and van der Vorst, R. The environmental impact of manufacturing planar and tubular solid oxide fuel cells. Journal of Power Sources 101(1) (2001): 10-26.

[5] Smith, W. The role of fuel cells in energy storage. Journal of Power Sources 86(1–2) (2000): 74-83.

[6] Huang, Q.-A., Hui, R., Wang, B., and Zhang, J. A review of AC impedance modeling and validation in SOFC diagnosis. Electrochimica Acta 52(28) (2007): 8144-8164.

[7] Mahato, N., Banerjee, A., Gupta, A., Omar, S., and Balani, K. Progress in material selection for solid oxide fuel cell technology: A review. Progress in Materials Science 72 (2015): 141-337.

[8] Sui, S. and Xiu, G.H. 14 - Fuels and fuel processing in SOFC applications A2 - Kendall, Kevin KendallMichaela. in High-Temperature Solid Oxide Fuel Cells for the 21st Century (Second Edition), pp. 461-495. Boston: Academic Press, 2016.

[9] Föger, K. 2 - Materials basics for fuel cells A2 - Gasik, Michael. in Materials for Fuel Cells, pp. 6-63: Woodhead Publishing, 2008.

[10] Kendall, K. 1 - Introduction to SOFCs. in High-Temperature Solid Oxide Fuel Cells for the 21st Century (Second Edition), pp. 1-24. Boston: Academic Press, 2016.

[11] Raghvendra, Singh, R.K., and Singh, P. Electrical conductivity of barium substituted LSGM electrolyte materials for IT-SOFC. Solid State Ionics 262 (2014): 428-432.

[12] Kilner, J.A., Druce, J., and Ishihara, T. 4 - Electrolytes A2 - Kendall, Kevin KendallMichaela. in High-Temperature Solid Oxide Fuel Cells for the 21st Century (Second Edition), pp. 85-132. Boston: Academic Press, 2016.

[13] Laukaitis, G., Dudonis, J., Orliukas, A.F., and Milcius, D. Properties of YSZ thin films deposited by e-beam technique. Solid State Ionics 179(1–6) (2008): 182-187.

[14] Wu, Y.-C., Lee, M.-J., and Li, X. Analysis of the microstructure and physical properties of $La_{0.85}Sr_{0.15}Ga_{0.8}Mg_{0.2}O_{2.825}$ and $Ce_{0.85}Sm_{0.15}O_{1.925}$ composite electrolytes used in solid oxide fuel cells. Journal of the European Ceramic Society 35(16) (2015): 4485-4495.

[15] Timurkutluk, B. The role of lamination conditions on electrochemical and mechanical performance of ceramic electrolytes for solid oxide fuel cells. Ceramics International 41(2, Part A) (2015): 2057-2068.

[16] Raghvendra, Kumar Singh, R., Sinha, A.S.K., and Singh, P. Investigations on structural and electrical properties of calcium substituted LSGM electrolyte materials for IT-SOFC. Ceramics International 40(7, Part B) (2014): 10711-10718.

[17] Sandoval, M.V., et al. Barium-modified NiO–YSZ/NiO–GDC cermet as new anode material for solid oxide fuel cells (SOFC). Solid State Ionics 261 (2014): 36-44.

[18] Wang, Z., Tian, Y., and Li, Y. Direct CH_4 fuel cell using Sr_2FeMoO_6 as an anode material. Journal of Power Sources 196(15) (2011): 6104-6109.

[19] Chiba, R., Yoshimura, F., Sakurai, Y., Tabata, Y., and Arakawa, M. A study of cathode materials for intermediate temperature SOFCs prepared by the sol-gel method. Solid State Ionics 175(1–4) (2004): 23-27.

[20] Haanappel, V.A.C., et al. Optimisation of processing and microstructural parameters of LSM cathodes to improve the electrochemical performance of anode-supported SOFCs. Journal of Power Sources 141(2) (2005): 216-226.

[21] Leone, P., Santarelli, M., Asinari, P., Calì, M., and Borchiellini, R. Experimental investigations of the microscopic features and polarization limiting factors of planar SOFCs with LSM and LSCF cathodes. Journal of Power Sources 177(1) (2008): 111-122.

[22] Liu, Y.L., Thydén, K., Chen, M., and Hagen, A. Microstructure degradation of LSM-YSZ cathode in SOFCs operated at various conditions. Solid State Ionics 206 (2012): 97-103.

[23] Morel, B., Roberge, R., Savoie, S., Napporn, T.W., and Meunier, M. Catalytic activity and performance of LSM cathode materials in single chamber SOFC. Applied Catalysis A: General 323 (2007): 181-187.

[24] Cassidy, M., Connor, P.A., Irvine, J.T.S., and Savaniu, C.D. 5 - Anodes A2 - Kendall, Kevin KendallMichaela. in High-Temperature Solid Oxide Fuel Cells for the 21st Century (Second Edition), pp. 133-160. Boston: Academic Press, 2016.

[25] Shaikh, S.P.S., Muchtar, A., and Somalu, M.R. A review on the selection of anode materials for solid-oxide fuel cells. Renewable and Sustainable Energy Reviews 51 (2015): 1-8.

[26] Molouk, A.F.S., Yang, J., Okanishi, T., Muroyama, H., Matsui, T., and Eguchi, K. Comparative study on ammonia oxidation over Ni-based cermet anodes for solid oxide fuel cells. Journal of Power Sources 305 (2016): 72-79.

[27] Niakolas, D.K. Sulfur poisoning of Ni-based anodes for Solid Oxide Fuel Cells in H/C-based fuels. Applied Catalysis A: General 486 (2014): 123-142.

[28] Rismanchian, A., Mirzababaei, J., and Chuang, S.S.C. Electroless plated Cu–Ni anode catalyst for natural gas solid oxide fuel cells. Catalysis Today 245 (2015): 79-85.

[29] Liu, M., et al. Performance of the nano-structured Cu–Ni (alloy) -CeO_2 anode for solid oxide fuel cells. Journal of Power Sources 274 (2015): 730-735.

[30] Hou, M., et al. Investigation into the effect of molybdenum-site substitution on the performance of $Sr_2Fe_{1.5}Mo_{0.5}O_{6-\delta}$ for intermediate temperature solid oxide fuel cells. Journal of Power Sources 272 (2014): 759-765.

[31] Johnsson, M. and Lemmens, P. Crystallography and chemistry of perovskites. Handbook of magnetism and advanced magnetic materials (2007).

[32] Erten, O. Electronic and Magnetic Properties of Double Perovskites and Oxide Interfaces. The Ohio State University, 2013.

[33] Richter, J., Holtappels, P., Graule, T., Nakamura, T., and Gauckler, L.J. Materials design for perovskite SOFC cathodes. Monatshefte für Chemie-Chemical Monthly 140(9) (2009): 985-999.

[34] Zhang, K., Ge, L., Ran, R., Shao, Z., and Liu, S. Synthesis, characterization and evaluation of cation-ordered $LnBaCo_2O_{5+\delta}$ as materials of oxygen permeation membranes and cathodes of SOFCs. Acta Materialia 56(17) (2008): 4876-4889.

[35] Sasaki, K., et al. Current-voltage characteristics and impedance analysis of solid oxide fuel cells for mixed H_2 and CO gases. Journal of The Electrochemical Society 149(3) (2002): A227-A233.

[36] Huang, Y.-H., Dass, R.I., Xing, Z.-L., and Goodenough, J.B. Double perovskites as anode materials for solid-oxide fuel cells. Science 312(5771) (2006): 254-257.

[37] Zhang, L., Zhou, Q., He, Q., and He, T. Double-perovskites $A_2FeMoO_{6-\delta}$ (A = Ca, Sr, Ba) as anodes for solid oxide fuel cells. Journal of Power Sources 195(19) (2010): 6356-6366.

[38] Suthirakun, S., et al. Theoretical investigation of H_2 oxidation on the $Sr_2Fe_{1.5}Mo_{0.5}O_6$ (001) perovskite surface under anodic solid oxide fuel cell conditions. Journal of the American Chemical Society 136(23) (2014): 8374-8386.

[39] Feng, J., et al. Investigation into the effect of Fe-site substitution on the performance of $Sr_2Fe_{1.5}Mo_{0.5}O_{6-\delta}$ anodes for SOFCs. Journal of Materials Chemistry A 2(41) (2014): 17628-17634.

[40] Pan, X., Wang, Z., He, B., Wang, S., Wu, X., and Xia, C. Effect of Co doping on the electrochemical properties of $Sr_2Fe_{1.5}Mo_{0.5}O_6$ electrode for solid oxide fuel cell. International Journal of Hydrogen Energy 38(10) (2013): 4108-4115.

[41] Kharton, V.V., Viskup, A.P., Bochkov, D.M., Naumovich, E.N., and Reut, O.P. Mixed electronic and ionic conductivity of $LaCo(M)O_3$ (M=Ga, Cr, Fe or Ni): III.

Diffusion of oxygen through $LaCo_{1-x-y}Fe_xNi_yO_{3\pm\delta}$ ceramics. Solid State Ionics 110(1–2) (1998): 61-68.

[42] Savaniu, C.-D. and Irvine, J.T. Reduction studies and evaluation of surface modified A-site deficient La-doped $SrTiO_3$ as anode material for IT-SOFCs. Journal of Materials Chemistry 19(43) (2009): 8119-8128.

[43] Wang, S.-F., Hsu, Y.-F., Lu, H.-C., Huang, C.-C., and Yeh, C.-T. $Sr_{1-x}Pr_xCo_{0.95}Sn_{0.05}O_{3-\delta}$ ceramic as a cathode material for intermediate-temperature solid oxide fuel cells. International Journal of Hydrogen Energy 37(17) (2012): 12548-12556.

[44] Jin, F., Xu, H., Long, W., Shen, Y., and He, T. Characterization and evaluation of double perovskites $LnBaCoFeO_{5+\delta}$ (Ln= Pr and Nd) as intermediate-temperature solid oxide fuel cell cathodes. Journal of Power Sources 243 (2013): 10-18.

[45] Ortiz-Vitoriano, N., Ruiz de Larramendi, I., Ruiz de Larramendi, J.I., Arriortua, M.I., and Rojo, T. Synthesis and electrochemical performance of $La_{0.6}Ca_{0.4}Fe_{1-x}Ni_xO_3$ (x = 0.1, 0.2, 0.3) material for solid oxide fuel cell cathode. Journal of Power Sources 192(1) (2009): 63-69.

[46] Muñoz-García, A.B., et al. Unveiling structure–property relationships in $Sr_2Fe_{1.5}Mo_{0.5}O_{6-\delta}$, an electrode material for symmetric solid oxide fuel cells. Journal of the American Chemical Society 134(15) (2012): 6826-6833.

[47] Xia, C., Rauch, W., Chen, F., and Liu, M. $Sm_{0.5}Sr_{0.5}CoO_3$ cathodes for low-temperature SOFCs. Solid State Ionics 149(1–2) (2002): 11-19.

[48] Enoki, M., Yan, J., Matsumoto, H., and Ishihara, T. High oxide ion conductivity in Fe and Mg doped $LaGaO_3$ as the electrolyte of solid oxide fuel cells. Solid State Ionics 177(19–25) (2006): 2053-2057.

[49] Smith, B.H. Development of Solid Oxide Fuel Cell Electrodes with High Conductivity and Enhanced Redox Stability. (2010).

[50] Vasala, S., Yamauchi, H., and Karppinen, M. Role of $SrMoO_4$ in Sr_2MgMoO_6 synthesis. Journal of Solid State Chemistry 184(5) (2011): 1312-1317.

[51] Rager, J., Zipperle, M., Sharma, A., and MacManus-Driscoll, J. Oxygen Stoichiometry in Sr_2FeMoO_6, the Determination of Fe and Mo Valence States, and the Chemical Phase Diagram of SrO-Fe_3O_4-MoO_3. Journal of the American Ceramic Society 87(7) (2004): 1330-1335.

[52] Xie, Z., et al. Effects of Co doping on the electrochemical performance of double perovskite oxide $Sr_2MgMoO_{6-\delta}$ as an anode material for solid oxide fuel cells. The Journal of Physical Chemistry C 116(17) (2012): 9734-9743.

[53] Moritomo, Y., et al. Electronic structure of double-perovskite transition-metal oxides. Physical Review B 61(12) (2000): R7827.

[54] Liu, Q., Dong, X., Xiao, G., Zhao, F., and Chen, F. A novel electrode material for symmetrical SOFCs. Advanced Materials 22(48) (2010): 5478-5482.

[55] Dai, N., et al. Synthesis and characterization of B-site Ni-doped perovskites $Sr_2Fe_{1.5-x}Ni_xMo_{0.5}O_{6-\delta}$ (x = 0, 0.05, 0.1, 0.2, 0.4) as cathodes for SOFCs. Journal of Materials Chemistry A 1(45) (2013): 14147-14153.

[56] Jiang, L., Liang, G., Han, J., and Huang, Y. Effects of Sr-site deficiency on structure and electrochemical performance in Sr_2MgMoO_6 for solid-oxide fuel cell. Journal of Power Sources 270 (2014): 441-448.

[57] Tai, L.-W., Nasrallah, M., Anderson, H., Sparlin, D., and Sehlin, S. Structure and electrical properties of $La_{1-x}Sr_xCo_{1-y}Fe_yO_3$. Part 2. The system $La_{1-x}Sr_xCo_{0.2}Fe_{0.8}O_3$. Solid State Ionics 76(3) (1995): 273-283.

[58] Sun, X.-F., Guo, R.-S., and Li, J. Preparation and properties of yttrium-doped $SrTiO_3$ anode materials. Ceramics International 34(1) (2008): 219-223.

[59] Mori, M. and Sammes, N.M. Sintering and thermal expansion characterization of Al-doped and Co-doped lanthanum strontium chromites synthesized by the Pechini method. Solid state ionics 146(3) (2002): 301-312.

[60] Kaus, I. and Anderson, H.U. Electrical and thermal properties of $La_{0.2}Sr_{0.8}Cu_{0.1}Fe_{0.9}O_{3-\delta}$ and $La_{0.2}Sr_{0.8}Cu_{0.2}Fe_{0.8}O_{3-\delta}$. Solid State Ionics 129(1) (2000): 189-200.

[61] Uhlenbruck, S. and Tietz, F. High-temperature thermal expansion and conductivity of cobaltites: potentials for adaptation of the thermal expansion

to the demands for solid oxide fuel cells. Materials Science and Engineering: B 107(3) (2004): 277-282.

[62] Li, Z., et al. Ba and Gd Doping Effect in $(Ba_xSr_{1-x})_{0.95}Gd_{0.05}Co_{0.8}Fe_{0.2}O_{3-\delta}$ (x = 0.1–0.9) Cathode on the Phase Structure and Electrochemical Performance. Fuel Cells 12(4) (2012): 633-641.

[63] Wei, T., Zhang, Q., Huang, Y.-H., and Goodenough, J.B. Cobalt-based double-perovskite symmetrical electrodes with low thermal expansion for solid oxide fuel cells. Journal of Materials Chemistry 22(1) (2012): 225-231.

[64] Shao, Z. and Haile, S.M. A high-performance cathode for the next generation of solid-oxide fuel cells. Nature 431(7005) (2004): 170-173.

[65] Tsipis, E., Naumovich, E., Shaula, A., Patrakeev, M., Waerenborgh, J., and Kharton, V. Oxygen nonstoichiometry and ionic transport in $La_2Ni(Fe)O_{4+\delta}$. Solid State Ionics 179(1) (2008): 57-60.

[66] Babakhani, E.G., Towfighi, J., Shirazi, L., Nakhaeipour, A., Zamaniyan, A., and Shafiei, Z. Structure Stability and Oxygen Permeability of Perovskite-type Oxides of $Ba_{0.5}Sr_{0.5}Co_{0.8}Fe_{0.1}R_{0.1}O_{3-\delta}$ (R= Al, Mn, Fe, Ce, Cr, Ni, Co). Journal of Materials Science & Technology 28(2) (2012): 177-183.

[67] Chen, C.-s., Zhang, Z.-p., Jiang, G.-s., Fan, C.-g., Liu, W., and Bouwmeester, H.J. Oxygen permeation through $La_{0.4}Sr_{0.6}Co_{0.2}Fe_{0.8}O_{3-\delta}$ membrane. Chemistry of materials 13(9) (2001): 2797-2800.

[68] Manthiram, A., Kim, J.-H., Kim, Y.N., and Lee, K.-T. Crystal chemistry and properties of mixed ionic-electronic conductors. Journal of electroceramics 27(2) (2011): 93-107.

[69] Taskin, A.A., Lavrov, A.N., and Ando, Y. Fast oxygen diffusion in A-site ordered perovskites. Progress in Solid State Chemistry 35(2–4) (2007): 481-490.

APPENDICIES

APPENDIX A

Ionic radii of some metal ions

Table A.1 Ionic crystal radii of concerned metal ions

Metal ion	Ionic charge	Coordination No.	Ionic radius (Å)
La	3+	12	1.36
Sr	2+	12	1.45
Pr	3+	12	1.13
Co	2+ (HS)	6	0.745
	2+ (LS)		0.65
	3+ (HS)		0.61
	3+ (LS)		0.545
	4+ (HS)		0.53
Fe	2+ (HS)	6	0.78
	2+ (LS)		0.61
	3+ (HS)		0.645
	3+ (LS)		0.55
	4+		0.585
Ni	2+	6	0.69
Mo	5+	6	0.61
	6+		0.59

HS = High spin configuration, LS = Low spin configuration

APPENDIX B

Activation energy (E_a)

Arrhenius equation (B.1) is shown below. The plot of ln (σT) versus 1000/T (K) gives a straight line, whose slope can be used to determine the E_a of small polaron conduction.

$$\sigma = (A/T)e^{(-Ea/RT)}$$

$$\ln (\sigma T) = \ln A\, e^{(-Ea/RT)}$$

$$\ln (\sigma T) = \ln e^{(-Ea/RT)} + \ln A \qquad \text{(B.1)}$$

$$\ln (\sigma T) = (-E_a/R)\,(1000/T) + \ln A$$

$$\downarrow \quad \downarrow \quad \downarrow \quad \downarrow$$

y slope x intercept y axis

$$-E_a/R = \text{Slope of the linear}$$

$$E_a = -\text{slope} \times R$$

Where A = material constant including the carrier concentration term

σ = specific conductivity ($S \cdot cm^{-1}$)

E_a = activation energy ($kJ \cdot mol^{-1}$)

T = temperature (K)

R = gas constant = 8.314472 $J \cdot K^{-1} \cdot mol^{-1}$

VITA

Miss Yupadee Ung-arphorn was born on February 14, 1990 in Pathumthani, Thailand. She graduated with Bachelor's Degree in Chemistry from Faculty of Science, Chulalongkorn University in 2011. She continued the Master's degree in program of Chemistry (Inorganic Chemistry), Faculty of Science, Chulalongkorn University in 2012 and completed in 2015.